Dynamic Response of Linear/Nonlinear Laminated Structures Containing Piezoelectric Laminas

by

Xiaoqing Liang

Dissertation submitted to the Faculty of the
Virginia Polytechnic Institute and State University
in partial fulfillment of the requirements for the degree of

Doctor of Philosophy

in

Engineering Mechanics

APPROVED:

Prof. Romesh C. Batra, Chairman

Prof. D.J. Inman

Prof. L. Librescu

Prof. L. Meirovitch

Prof. S.M. Sun

February, 1997
Blacksburg, Va

Keywords: finite element, laminated composite structures, linear elasticity, nonlinear piezoelectric materials.

Dynamic Response of Linear/Nonlinear Laminated Structures Containing Piezoelectric Laminas

Xiaoqing Liang
(ABSTRACT)

The three-dimensional linear theory of piezo-elasticity is used to analyse steady state vibrations of a simply supported rectangular laminated composite plate with piezoelectric (PZT) actuator and sensor patches either embedded in it or bonded to the its surfaces. It is assumed that different layers are perfectly bonded to each other. The method of Fourier series is used to find an analytical solution of the problem. The analytical solution is then applied to study the shape control of a steadily vibrating composite plate by exciting different regions of a PZT actuator. Numerical results for a thin and a thick plate containing one embedded actuator layer and one embedded sensor layer are presented. For the former case, the optimum location of the centroid of the excited rectangular region that will require minimum voltage to control the out-of-plane displacements is determined. Keeping the location of the centroid and the shape of the excited region fixed, we ascertain the voltage required as a function of the length of its diagonal to nullify the deflections of the plate. The maximum shear stress at the interface between the sensor and the lamina is found to be lower than that between the actuator and the lamina. The point of maximum output voltage from the sensor coincides with that of its peak out-of-plane displacement. The variations of displacement and stress components through the thickness for the thin and thick plates are similar.

The transient finite deformations of a neo-Hookean beam or plate with PZT patches bonded to its upper and lower surfaces are simulated by the finite element method. The constitutive relation for the piezoelectric material is taken to be linear in the Green-Lagrange strain tensor but quadratic in the driving voltage. A code using 8-noded brick elements has been developed and validated by comparing computed results with either analytical solutions or experimental observations. The code is then used to study flexural waves generated by PZT actuators and propagating through a cantilever beam both with and without a defect in it. The computed results are compared with test observations and with the published results for the linear elastic beam. The effects of both geometrical and material nonlinearities are discussed. A simple feedback control algorithm is shown to annul the motion of a neo-Hookean plate subjected to an impulsive load.

Acknowledgments:

I would like to express my sincere appreciation to my advisor Professor Romesh C. Batra for his long-term support and guidance during the course of this study. Special thanks are due to Professors D.J. Inman and L. Librescu for their helpful suggestions in this study. I would also like to extend my thanks to Professor L. Meirovitch and Professor S.M. Sun for taking the time to review my work and serve on my committee.

This work was supported by the U.S. Army Research Office grant DAAH04-93-G-0214 to the University of Missouri-Rolla, and a matching grant from the Missouri Research and Training Center. The Virginia Polytechnic Institute and State University acted as a subcontractor to the University of Missouri-Rolla.

Finally, I would like to dedicate this dissertation to my wife, Jing, and my parents, Yun-Ying Liao and Yan-Wen Liang. Without their love and support I would never have come this far.

Contents

List of Figures

Chapter 1

The Vibration of a Rectangular Laminated Elastic Plate with Embedded Piezoelectric Sensors and Actuators

Abstract

We use the three-dimensional linear theory of elasticity to analyse the steady state vibrations of a simply supported rectangular linear elastic laminated plate with embedded PZT layers. Some of these PZT layers act as actuators while the remaining act as sensors. It is assumed that there is perfect bonding between different layers. Numerical results for a thin and a thick plate containing one embedded actuator layer and one embedded sensor layer are presented. For the former case, the optimum location of the centroid of the excited rectangular region that will result in the maximum out-of-plane displacement for a given distribution of the applied voltage is also determined. Equivalently, an equal and opposite voltage applied to this region of a vibrating plate will be most effective in diminishing these vibrations. The maximum shear stress at the interface between the sensor and the lamina is lower than that between the actuator and the lamina. The point of maximum output voltage from the sensor coincides with that of peak out-of-plane displacement. The variations of displacement and stress components through the thickness for the thin and thick plates are similar.

[0]A slightly different version of this chapter has appeared in *Computers and Structures*, Vol.63, pp.203-216, 1997

1.1 Introduction

An interesting problem in smart structures is to control the shape of a plate subjected to a static or time harmonic external disturbance with the least expenditure of energy. It requires estimating dynamic response of the plate, finding the optimum shapes, number and placement of distributed actuators and sensors on the given plate, and designing a robust control algorithm [1,2]. The general problem of a plate with distributed PZT actuators and sensors partially covering the plate surfaces is hard to analyse. Here we analyse time harmonic vibrations of a simply supported rectangular laminated plate with thin piezoelectric layers embedded in it. An actuator patch is modelled by applying voltage only on a portion of the actuator layer. This is justified because the mass and rigidity of thin PZT layers do not affect significantly the dynamic response of a plate; this will be demonstrated below. We use the three-dimensional linear theory of elasticity to analyse this problem for the first few modes of vibration of the plate. We also compare the distributions of deformation fields and stresses in a thin and a thick plate. We note that a similar problem when PZT layers are fixed to the top and bottom surfaces of the plate has recently been analysed by Batra et al. [3]. However, the problem with embedded PZT layers is more practical since insulation from environmental effects, aesthetics and other design considerations may necessitate that PZT layers be embedded in the structure. Mathematically, the problem is more challenging because of (i) the additional effects involved in the equations of motion for the PZT layers, and (ii) the need to solve for the voltage output from PZTs used as sensors. Also more than one layer of PZT sensors and actuators can be embedded in the plate. As before [3], the PZT layers are modeled as thin films. Here, we also compare results for a thin and a thick plate.

Piezoelectric elements have been extensively used to control the vibrations of a beam, e.g., see Baz and Poh [4], Tzou and Tseng [5], and Crawley and de Luis [6]. Elastic plates with PZT films attached to their surfaces have been analyzed by using approximate two-dimensional plate theories [7-11], and also by using the three-dimensional equations of elasticity and the method of Fourier series [12-19]. Here we use the three-dimensional equations of linear elasticity to study the vibrations and structural response of a steadily vibrating simply supported rectangular laminated plate.

1.2 Formulation of the Problem

1.2.1 Governing Equations

We consider a simply supported rectangular laminated elastic plate of dimensions a and b in x_1 and x_2 directions respectively. The total thickness of the plate made up of N layers,

not necessarily of the same thickness and including N_s layers of sensors and N_a layers of actuators equals $2h$ (cf. Fig. 1.1); the ith layer is determined by $h^{(i-1)} \le x_3 \le h^{(i)}$. We note that some of these layers are made of a linear piezoelectric material while others are made of a linear elastic material. Both sensors and actuators are modeled as thin films (Tiersten [20], Mindlin [21]) poled in the x_3-direction, and are assumed to be transversely isotropic with x_3-axis as the preferred direction. Each of the elastic laminate is assumed to be made of an orthotropic material with constitutive equations given by

$$\begin{aligned} \tau_{\alpha\beta}^{(i)} &= c_{\alpha\beta\gamma\delta}^{(i)} e_{\gamma\delta}^{(i)}, \ \alpha,\beta,\gamma,\delta = 1,2,3, \\ e_{\alpha\beta}^{(i)} &= (u_{\alpha,\beta}^{(i)} + u_{\beta,\alpha}^{(i)})/2 \ . \end{aligned} \tag{1.1}$$

Here $\tau_{\alpha\beta}$ is the Cauchy stress tensor, $c_{\alpha\beta\gamma\delta}$ the material elasticity tensor, $e_{\alpha\beta}$ the infinitesimal strain tensor, u_α the displacement of a point, $u_{\alpha,\beta} = \partial u_\alpha/\partial x_\beta$, a repeated index implies summation over the range of the index, and a superscript i in parentheses indicates quantities for the i-th layer. Henceforth we drop the superscript i unless it is needed for clarity.

For an elastic laminate, governing equations in terms of displacements $\mathbf{u}$ are

$$\begin{aligned} &c_{11}^{(i)} u_{1,11}^{(i)} + c_{66}^{(i)} u_{1,22}^{(i)} + c_{55}^{(i)} u_{1,33}^{(i)} + (c_{12}^{(i)} + c_{66}^{(i)}) u_{2,12}^{(i)} + (c_{13}^{(i)} + c_{55}^{(i)}) u_{3,13}^{(i)} = \rho^{(i)} \ddot{u}_1^{(i)} \\ &(c_{12}^{(i)} + c_{66}^{(i)}) u_{1,12}^{(i)} + c_{66}^{(i)} u_{2,11}^{(i)} + c_{22}^{(i)} u_{2,22}^{(i)} + c_{44}^{(i)} u_{2,33}^{(i)} + (c_{23}^{(i)} + c_{44}^{(i)}) u_{3,23}^{(i)} = \rho^{(i)} \ddot{u}_2^{(i)} \\ &(c_{13}^{(i)} + c_{55}^{(i)}) u_{1,13}^{(i)} + (c_{23}^{(i)} + c_{44}^{(i)}) u_{2,23}^{(i)} + c_{55}^{(i)} u_{3,11}^{(i)} + c_{44}^{(i)} u_{3,22}^{(i)} + c_{33}^{(i)} u_{3,33}^{(i)} = \rho^{(i)} \ddot{u}_3^{(i)} \end{aligned} \tag{1.2}$$

where a superimposed dot indicates material time derivative which for infinitesimal deformations reduces to partial time derivative, and $c_{\alpha\beta}$ are the material elasticities when $\tau_{\alpha\beta}$ and $e_{\alpha\beta}$ are written as six-dimensional vectors. The boundary conditions at the simply supported edges, when the plate is viewed as a 3-dimensional body, are

$$\begin{aligned} &\tau_{11}^{(i)} = c_{11}^{(i)} u_{1,1}^{(i)} + c_{12}^{(i)} u_{2,2}^{(i)} + c_{13}^{(i)} u_{3,3}^{(i)} = 0, \ u_3^{(i)} = 0, \ u_2^{(i)} = 0 \text{ at } x_1 = 0, \ a \\ &\tau_{22}^{(i)} = c_{12}^{(i)} u_{1,1}^{(i)} + c_{22}^{(i)} u_{2,2}^{(i)} + c_{23}^{(i)} u_{3,3}^{(i)} = 0, \ u_3^{(i)} = 0, \ u_1^{(i)} = 0 \text{ at } x_2 = 0, \ b. \end{aligned} \tag{1.3}$$

These simulate a simply supported edge characterized by the vanishing of the deflection and the bending moment there, and have been used by Srinivas et al. [15], Wattrick [16], and Yang et al. [18].

At the interface $x_3 = h^{(i)}$ between the i-th and the $(i+1)$th layers, coherency conditions, i.e., the continuity of surface tractions and displacements, imply the following.

$$\begin{aligned} c_{55}^{(i)}(u_{3,1}^{(i)} + u_{1,3}^{(i)}) &= c_{55}^{(i+1)}(u_{3,1}^{(i+1)} + u_{1,3}^{(i+1)}) \text{ at } x_3 = h^{(i)} \\ c_{44}^{(i)}(u_{2,3}^{(i)} + u_{3,2}^{(i)}) &= c_{44}^{(i+1)}(u_{2,3}^{(i+1)} + u_{3,2}^{(i+1)}) \text{ at } x_3 = h^{(i)} \\ c_{13}^{(i)} u_{1,1}^{(i)} + c_{23}^{(i)} u_{2,2}^{(i)} + c_{33}^{(i)} u_{3,3}^{(i)} &= c_{13}^{(i+1)} u_{1,1}^{(i+1)} + c_{23}^{(i+1)} u_{2,2}^{(i+1)} + c_{33}^{(i+1)} u_{3,3}^{(i+1)} \text{ at } x_3 = h^{(i)} \\ u_1^{(i)} = u_1^{(i+1)}, \ u_2^{(i)} &= u_2^{(i+1)}, \ u_3^{(i)} = u_3^{(i+1)} \text{ at } x_3 = h^{(i)}. \end{aligned} \tag{1.4}$$

Since the bottom and top surfaces of the plate are traction free, boundary conditions on them correspond to the vanishing of expressions on the left-hand sides of equations $(1.4)_{1\text{-}3}$ with $i = 1$, $x_3 = -h$ and $i = N$, $x_3 = h$ respectively.

Recalling that sensors and actuators are modeled as thin films, the balance of linear momentum and the Maxwell equation for any one of them can be written as (Mindlin [21])

$$\begin{aligned} \tau^{(i)}_{11,1} + \tau^{(i)}_{12,2} + [\![\tau^{(i)}_{31}]\!] &= \rho^{(i)}\ddot{u}^{(i)}_1, \\ \tau^{(i)}_{21,1} + \tau^{(i)}_{22,2} + [\![\tau^{(i)}_{32}]\!] &= \rho^{(i)}\ddot{u}^{(i)}_2, \\ [\![\tau^{(i)}_{33}]\!] &= \rho^{(i)}\ddot{u}^{(i)}_3, \\ D^{(i)}_{\alpha,\alpha} &= 0. \end{aligned} \tag{1.5}$$

where

$$[\![\tau^{(i)}_{31}]\!] = \left(\tau^{(i+1)}_{31}\big|_{x_3=h^{(i)}} - \tau^{(i-1)}_{31}\big|_{x_3=h^{(i-1)}}\right)/h^{(i)} \ , \tag{1.6}$$

and D_α is the electric displacement. The constitutive equations for a linear piezoelectric medium are

$$\begin{aligned} \mathbf{D} &= \mathbf{e}^T\mathbf{s} + \boldsymbol{\epsilon}\mathbf{E}, \\ \boldsymbol{\tau} &= \mathbf{c}\mathbf{s} - \mathbf{e}\mathbf{E} \end{aligned} \tag{1.7}$$

where $\mathbf{E}$ is the electric field vector given by $\mathbf{E} = -\text{grad}\phi$, ϕ is the voltage field, $\mathbf{e}$ the piezoelectric constants and $\boldsymbol{\epsilon}$ the dielectric permittivity. We note that the material response of PZT and PVDF can be represented by constitutive equations (1.7).

Since the thickness of a sensor or an actuator is very small as compared to that of a lamina, it is reasonable to assume that $|D_{1,1}| << |D_{3,3}|$ and $|D_{2,2}| << |D_{3,3}|$; (cf. Tiersten [20]). Thus equation $(1.5)_4$ reduces to

$$D^{(i)}_{3,3} = 0, \text{ or } \phi^{(i)}_{,33} = 0 \ . \tag{1.8}$$

Following Brooks and Heyliger [14], we assume the electric potential ϕ to be a linear function of x_3. That is,

$$\phi^{(i)}(x_1, x_2, x_3, t) = \Phi^{(i)}(x_1, x_2, t)\frac{x_3 - h^{(i-1)}}{h^{(i)} - h^{(i-1)}}. \tag{1.9}$$

Hence equation (1.8) or equivalently $(1.5)_4$ is identically satisfied.

Boundary conditions at the edges of a PZT sensor/actuator and at the interfacial surfaces are

$$\begin{aligned} \tau^{(i)}_{11} = u^{(i)}_2 = u^{(i)}_3 &= 0, \text{ at } x_1 = 0, a, \\ \tau^{(i)}_{22} = u^{(i)}_1 = u^{(i)}_3 &= 0, \text{ at } x_2 = 0, b, \\ u^{(i)}_\alpha &= u^{(i+1)}_\alpha, \text{ at } x_3 = h^{(i)}, \\ u^{(i)}_\alpha &= u^{(i-1)}_\alpha, \text{ at } x_3 = h^{(i-1)} \ . \end{aligned} \tag{1.10}$$

Note that the continuity of tractions at the interface between the PZT/PVDF layer and the lamina has been considered in writing the equations of motion for a PZT/PVDF material point. For an actuator, we also have

$$\begin{aligned} \Phi^{(i)}(x_1, x_2, t) &= V^a(x_1, x_2, t) \quad \text{at} \quad x_3 = h^{(i)}, \\ \Phi^{(i)}(x_1, x_2, t) &= 0 \qquad\qquad \text{at} \quad x_3 = h^{(i-1)} \ , \end{aligned} \tag{1.11}$$

and for a sensor,

$$\begin{aligned} \Phi^{(i)}(x_1, x_2, t) &= 0 \quad \text{at} \quad x_3 = h^{(i-1)}, \\ D_3 \qquad\qquad &= 0 \quad \text{at} \quad x_3 = h^{(i)} \ . \end{aligned} \tag{1.12}$$

This completes the formulation of the problem.

1.2.2 Time Harmonic Vibrations

We assume that the actuators are excited by a time harmonic voltage

$$V^{(i)}(x_1, x_2, t) = \tilde{V}^{(i)}(x_1, x_2) e^{i\omega t}, \tag{1.13}$$

and seek solutions of the governing equations which are also time harmonic with the same frequency. That is

$$\begin{aligned} u_\alpha^{(i)}(x_1, x_2, x_3, t) &= \tilde{u}_\alpha^{(i)}(x_1, x_2, x_3) e^{i\omega t}, \\ \Phi^{(i)}(x_1, x_2, t) &= \tilde{\Phi}^{(i)}(x_1, x_2) e^{i\omega t}. \end{aligned} \tag{1.14}$$

Henceforth we drop the superimposed tilde. The form of equations given in the preceding section is unchanged except that $\ddot{\mathbf{u}}$ is replaced by $-\omega^2 \mathbf{u}$.

1.3 Solutions

The solution procedure is similar to that described by Batra et al. [19] and is therefore briefly sketched below.

1.3.1 Solutions for the Substrate Laminates

We assume that the displacements of the i-th layer can be represented by the following Fourier series.

$$u_1^{(i)} = \sum_{m,n=1}^{\infty} a_{1mn}^{(i)}(x_3)\cos\alpha_m x_1 \sin\beta_n x_2$$
$$u_2^{(i)} = \sum_{m,n=1}^{\infty} a_{2mn}^{(i)}(x_3)\sin\alpha_m x_1 \cos\beta_n x_2$$
$$u_3^{(i)} = \sum_{m,n=1}^{\infty} a_{3mn}^{(i)}(x_3)\sin\alpha_m x_1 \sin\beta_n x_2$$
$$\alpha_m = m\pi/a,\ \beta_n = n\pi/b. \tag{1.15}$$

These satisfy boundary conditions at the edges $x_1 = 0, a$ and $x_2 = 0, b$. Substitution of (1.15) into equation (1.14) and then into the governing equations (1.2) yields ordinary differential equations for $a_{\alpha mn}(x_3)$ which are solved by assuming that

$$a_{\alpha mn}(x_3) = A_{\alpha mn} e^{\eta_{mn} x_3},\ \text{no sum on } m, n, \tag{1.16}$$

where $A_{\alpha mn}$ are undetermined constants. Equation (1.16) when substituted into the ordinary differential equations will yield a set of linear homogeneous equations for the determination of $A_{\alpha mn}$; the coefficients of these equations involve the elastic constants for the material of the laminate and the frequency ω. In order for these equations to have a nontrivial solution, the determinant of the coefficients of $A_{\alpha mn}$ must vanish. This gives the following cubic equation for $(\eta_{mn})^2$.

$$(\eta_{mn})^6 + a(\eta_{mn})^4 + b(\eta_{mn})^2 + c = 0 \tag{1.17}$$

Explicit expressions for a, b and c in terms of the elasticities of the laminate and the frequency ω are given in Batra et al. [19]. For distinct real or complex conjugate roots $\eta_{mnp},\ p = 1, 2, \ldots, 6$, we have

$$a_{\alpha mn}(x_3) = D_{mnp} F_{\alpha mnp} e^{\eta_{mnp} x_3} \text{ no sum on } m, n,\ \text{but summed on } p \tag{1.18}$$

where D_{mnp} is an arbitrary constant and $F_{\alpha mnp}$ is a function of η_{mnp} and the material parameters. We note that for a few values of ω, equation (1.17) may have repeated real roots; it is more likely to occur for an isotropic material. We exclude those special values of ω.

Equation (1.18) when substituted into (1.15) gives the displacement field in the i-th laminate.

$$u_1^{(i)} = \sum_{m,n=1}^{\infty} \left[\sum_{p=1}^{6} D_{mnp}^{(i)} F_{1mnp}^{(i)}(x_3) \right] \cos \alpha_m x_1 \sin \beta_n x_2,$$
$$u_2^{(i)} = \sum_{m,n=1}^{\infty} \left[\sum_{p=1}^{6} D_{mnp}^{(i)} F_{2mnp}^{(i)}(x_3) \right] \sin \alpha_m x_1 \cos \beta_n x_2,$$
$$u_3^{(i)} = \sum_{m,n=1}^{\infty} \left[\sum_{p=1}^{6} D_{mnp}^{(i)} F_{3mnp}^{(i)}(x_3) \right] \sin \alpha_m x_1 \sin \beta_n x_2. \tag{1.19}$$

Thus strains and stresses in the i-th laminate can be computed. The continuity conditions at the interface $x_3 = h^{(i)}$ between the two laminates yield

$$[D_{mnp}^{(i)}] = [T^{(i)}][D_{mnp}^{(i+1)}] \tag{1.20}$$

where $[D_{mnp}^{(i)}]$ is a 6×1 matrix (for $p = 1, 2, \ldots, 6$) and $[T^{(i)}]$ is a 6×6 matrix whose elements are functions of $F_{\alpha mnp}^{(i)}$ and $F_{\alpha mnp}^{(i+1)}$ evaluated at $x_3 = h^{(i)}$. Equation (1.20) is a recursive relation between constants for the ith and $(i+1)$th laminate and can be used repeatedly to express constants for the k-th laminate in terms of those for the ℓ-th laminate provided that no sensor or actuator layer is between them.

The traction-free conditions at the top and bottom surfaces yield

$$\sum_{p=1}^{6} R_{\alpha mnp}^{(1)} D_{mnp}^{(1)} = 0, \ \sum_{p=1}^{6} R_{\alpha mnp}^{(N)} D_{mnp}^{(N)} = 0, \tag{1.21}$$

where $R_{\alpha mnp}^{(1)}$ and $R_{\alpha mnp}^{(N)}$ are functions of $F_{\alpha mnp}$ evaluated at $x_3 = -h$ and $x_3 = h$ respectively.

1.3.2 Solutions for Actuator Layers

For the ith-layer made of a PZT material and assumed to act as an actuator, we presume that

$$u_1^{(i)}(x_1, x_2) = \sum_{m,n=1}^{\infty} \bar{D}_{1mn}^{(i)} \cos \alpha_m x_1 \sin \beta_n x_2,$$
$$u_2^{(i)}(x_1, x_2) = \sum_{m,n=1}^{\infty} \bar{D}_{2mn}^{(i)} \sin \alpha_m x_1 \cos \beta_n x_2,$$
$$u_3^{(i)}(x_1, x_2) = \sum_{m,n=1}^{\infty} \bar{D}_{3mn}^{(i)} \sin \alpha_m x_1 \sin \beta_n x_2 \tag{1.22}$$

where

$$\bar{D}^{(i)}_{1mn} = \frac{4}{ab}\int_0^a\int_0^b u_1^{(i)} \cos\alpha_m x_1 \sin\beta_n x_2 dx_1 dx_2$$
$$\bar{D}^{(i)}_{2mn} = \frac{4}{ab}\int_0^a\int_0^b u_2^{(i)} \sin\alpha_m x_1 \cos\beta_n x_2 dx_1 dx_2$$
$$\bar{D}^{(i)}_{3mn} = \frac{4}{ab}\int_0^a\int_0^b u_3^{(i)} \sin\alpha_m x_1 \sin\beta_n x_2 dx_1 dx_2 \tag{1.23}$$

These satisfy the homogeneous edge conditions for mechanical displacements in equations $(1.10)_{1\text{-}2}$. When the applied electric voltages are not zero at the edges of actuators, the stress conditions in equations $(1.10)_{1\text{-}2}$ will become nonhomogeneous and the displacements (1.22), after term by term differentiation, cannot accomodate the nonhomogeneous conditions. This is so because the Fourier series (1.22) for the nonhomogeneous boundary conditions case do not have the uniform convergence needed for term by term differentiation. In order to avoid term by term differentiation and to take care of the nonhomogeneous boundary conditions at the same time, we multiply equations obtained from $(1.5)_{1\text{-}3}$ by $\cos\alpha_m\ x_1 \sin\beta_n x_2$, $\sin\alpha_m x_1 \cos\beta_n x_2$ and $\sin\alpha_m x_1 \sin\beta_n x_2$ respectively, and integrate the resulting equations over $0 < x_1 < a$ and $0 < x_2 < b$. With integration by parts and the use of boundary conditions we arrive at the following.

$$\sum_{p=1}^{6} R^{(i+1)}_{mnp}(h^{(i)}) D^{(i+1)}_{mnp} - \sum_{p=1}^{6} R^{(i-1)}_{mnp}(h^{(i-1)}) D^{(i-1)}_{mnp}$$
$$+h^{(i)}(\rho^{(i)}\omega^2 - c^{(i)}_{11}\alpha_m^2 - c^{(i)}_{66}\beta_n^2)\bar{D}^{(i)}_{1mn} - h^{(i)}(c^{(i)}_{12} + c^{(i)}_{66})\alpha_m\beta_n\bar{D}^{(i)}_{2mn}$$
$$= -\frac{4e^{(i)}_{31}}{ab}\alpha_m \int_0^a\int_0^b \tilde{V}^{(i)} \sin\alpha_m x_1 \sin\beta_n x_2 dx_1 dx_2, \tag{1.24}$$

$$\sum_{p=1}^{6} Q^{(i+1)}_{mnp}(h^{(i)}) D^{(i+1)}_{mnp} - \sum_{p=1}^{6} Q^{(i-1)}_{mnp}(h^{(i-1)}) D^{(i-1)}_{mnp}$$
$$-h^{(i)}(c^{(i)}_{12} + c^{(i)}_{66})\alpha_m\beta_n\bar{D}^{(i)}_{1mn} + h^{(i)}(\rho^{(i)}\omega^2 - c^{(i)}_{66}\alpha_m^2 - c^{(i)}_{11}\beta_n^2)\bar{D}^{(i)}_{2mn}$$
$$= -\frac{4e^{(i)}_{31}}{ab}\beta_n \int_0^a\int_0^b \tilde{V}^{(i)} \sin\alpha_m x_1 \sin\beta_n x_2 dx_1 dx_2, \tag{1.25}$$

$$\sum_{p=1}^{6} P^{(i+1)}_{mnp}(h^{(i)}) D^{(i+1)}_{mnp} - \sum_{p=1}^{6} P^{(i-1)}_{mnp}(h^{(i-1)}) D^{(i-1)}_{mnp} + h^{(i)}\rho^{(i)}\omega^2\bar{D}^{(i)}_{3mn} = 0, \tag{1.26}$$

where R_{mnp}, Q_{mnp} and P_{mnp} are linear functions of $F_{\alpha mnp}$ and $F_{\alpha mnp,3}$, and $\tilde{V}^{(i)}$ is a known function of x_1 and x_2. The continuity conditions $(1.10)_{3,4}$ at the interface between the plate

and the actuator give the following.

$$\begin{aligned}
&\sum_{p=1}^{6} F_{1mnp}^{(i-1)}(h^{(i-1)})D_{mnp}^{(i-1)} - \bar{D}_{1mn}^{(i)} = 0,\\
&\sum_{p=1}^{6} F_{2mnp}^{(i-1)}(h^{(i-1)})D_{mnp}^{(i-1)} - \bar{D}_{2mn}^{(i)} = 0,\\
&\sum_{p=1}^{6} F_{3mnp}^{(i-1)}(h^{(i-1)})D_{mnp}^{(i-1)} - \bar{D}_{3mn}^{(i)} = 0,\\
&\sum_{p=1}^{6} F_{1mnp}^{(i+1)}(h^{(i)})D_{mnp}^{(i+1)} - \bar{D}_{1mn}^{(i)} = 0,\\
&\sum_{p=1}^{6} F_{2mnp}^{(i+1)}(h^{(i)})D_{mnp}^{(i+1)} - \bar{D}_{2mn}^{(i)} = 0,\\
&\sum_{p=1}^{6} F_{3mnp}^{(i+1)}(h^{(i)})D_{mnp}^{(i+1)} - \bar{D}_{3mn}^{(i)} = 0,
\end{aligned} \tag{1.27}$$

where coefficients $\bar{D}_{\alpha mn}^{(i)},\ \alpha = 1, 2, 3$ are to be determined.

1.3.3 Solutions for Sensor Layers

Let the ith layer made of a PZT material act as a sensor. For it, we assume that the displacement field is given by (1.22), and

$$\Phi^{(i)} = \sum_{m,n=1}^{\infty} \phi_{mn}^{(i)} \sin\alpha_m x_1 \sin\beta_n x_2. \tag{1.28}$$

A procedure similar to that used for an actuator layer yields the following set of equations.

$$\begin{aligned}
&\sum_{p=1}^{6} R_{mnp}^{(i+1)}(h^{(i)})D_{mnp}^{(i+1)} - \sum_{p=1}^{6} R_{mnp}^{(i-1)}(h^{(i-1)})D_{mnp}^{(i-1)}\\
&+h^{(i)}\left[\rho^{(i)}\omega^2 - c_{11}^{(i)}\alpha_m^2 - c_{66}^{(i)}\beta_n^2\right] D_{1mn}^{(i)} - h^{(i)}(c_{12}^{(i)} + c_{66}^{(i)})\alpha_m\beta_n D_{2mn}^{(i)} + e_{31}^{(i)}\alpha_m\phi_{mn}^{(i)} = 0,
\end{aligned} \tag{1.29}$$

$$\begin{aligned}
&\sum_{p=1}^{6} Q_{mnp}^{(i+1)}(h^{(i)})D_{mnp}^{(i+1)} - \sum_{p=1}^{6} Q_{mnp}^{(i-1)}(h^{(i-1)})D_{mnp}^{(i-1)}\\
&-h^{(i)}(c_{12}^{(i)} + c_{66}^{(i)})\alpha_m\beta_n D_{1mn}^{(i)} + h^{(i)}\left[\rho^{(i)}\omega^2 - c_{66}^{(i)}\alpha_m^2 - c_{11}^{(i)}\beta_n^2\right] D_{2mn}^{(i)} + e_{31}^{(i)}\beta_n\phi_{mn}^{(i)} = 0,
\end{aligned} \tag{1.30}$$

$$\sum_{p=1}^{6} P_{mnp}^{(i+1)}(h^{(i)})D_{mnp}^{(i+1)} - \sum_{p=1}^{6} P_{mnp}^{(i-1)}(h^{(i-1)})D_{mnp}^{(i-1)} + h^{(i)}\rho^{(i)}\omega^2 D_{3mn}^{(i)} = 0. \tag{1.31}$$

The continuity conditions at the interface between a sensor and a laminate are analogous to equations (1.27) with the addition of the following equation.

$$h^{(i)}e_{31}^{(i)}\alpha_m D_{1mn}^{(i)} + h^{(i)}e_{31}^{(i)}\beta_n D_{2mn}^{(i)} + \epsilon_{33}^{(i)}\phi_{mn}^{(i)} = 0. \tag{1.32}$$

Knowing ω and the voltage field applied to the actuators, we solve the aforestated equations for various Fourier coefficients and hence can find the displacements, strains, stresses and sensor electric voltages at any point in the structure.

1.4 Numerical Results

As an example, we consider a $30\sqrt{2}$ cm $\times$ 30 cm $\times$ 0.404 cm plate made of 10 layers of T300/976 graphite-epoxy laminates each 0.04 cm thick, a layer of PZT - G1195 actuator 0.002 cm thick, and a layer of PZT-G1195 sensor also 0.002 cm thick; the substrates are arranged symmetrically as 0/90/0/90.... The actuator layer is located between the second and the third substrate layers from the bottom of the structure, and the sensor layer is located between the second and the third layers from the top of the structure. The material properties of the graphite/epoxy layer with respect to the local principal axes are taken to be

$$\begin{gathered} E_{11} = 150 \text{ GPa},\ E_{22} = E_{33} = 9 \text{ GPa},\ \nu_{12} = \nu_{23} = \nu_{13} = 0.3, \\ G_{12} = G_{31} = 7.1 \text{ GPa},\ G_{23} = 2.5 \text{ GPa},\ \rho = 1600 \text{ kg/m}^3, \end{gathered} \tag{1.33}$$

and those for the PZT-G1195 are

$$\rho = 7500 \text{ kg/m}^3,\ [e] = \begin{bmatrix} 0 & 0 & -2.1 \\ 0 & 0 & -2.1 \\ 0 & 0 & 9.5 \\ 0 & 9.2 & 0 \\ 9.2 & 0 & 0 \\ 0 & 0 & 0 \end{bmatrix}^T C/m^2;$$

$$[c] = \begin{bmatrix} 148 & 76.2 & 74.2 & 0 & 0 & 0 \\ & 148 & 74.2 & 0 & 0 & 0 \\ & & 131 & 0 & 0 & 0 \\ & & & 25.4 & 0 & 0 \\ & & & & 25.4 & 0 \\ & & & & & 25.4 \end{bmatrix} GPa \tag{1.34}$$

The applied voltage is a half sine function over a rectangular region of $a/10.5 \times b/10.5$ with a peak value of 200 volts and equals zero outside this region. This simulates finite size PZT patches used in practice.

The Fourier series converges very fast; it takes the first 30 terms of the Fourier series in equations (1.22) to compute displacements accurate to first 5 significant digits. However, computation of stresses involves the spatial gradients of the displacements and more terms are needed. Here we take 400 terms to evaluate strains and stresses.

1.4.1 Natural Frequencies of the Plate

The structure has a series of natural frequencies which can be ordered as $\omega_{mn},\ m,n = 1,2,\ldots$. These are determined by plotting the vertical component of the deflection at the point $\left(\frac{a}{4},\ \frac{b}{4},\ 0\right)$ as a function of the forcing frequency. The deflection becomes large at certain discrete values of the forcing frequency which signifies the resonance phenomenon; the natural frequencies so computed are listed in Table 1.1. The normalized natural frequencies Ω_{mn} of the structure, estimated from the thin plate theory, and with the inertia and rigidity of the piezoelectric layers neglected, are given by (Jones [22])

$$\Omega_{mn} \equiv \frac{\omega_{mn}}{\left(\frac{\pi^2}{a^2}\left(\frac{D_{11}}{2\rho h}\right)^{1/2}\right)} = \left[m^4 + 2\frac{D_{12}+2D_{66}}{D_{11}}m^2\left(\frac{a}{b}n\right)^2 + \frac{D_{22}}{D_{11}}\left(\frac{a}{b}n\right)^4\right]^{1/2} \tag{1.35}$$

where $D_{\alpha\beta}$ $(\alpha,\beta = 1,2,6)$ is the flexural rigidity. As is clear from the values listed in Table 1, the maximum difference between the first six natural frequencies computed from the thin plate theory with no PZT layers and the present analysis employing the three dimensional elasticity theory and considering the inertia and rigidity of the PZT layers is 4%. Thus for a thin plate with very thin piezoelectric films embedded in it, both theories give nearly identical values of the natural frequencies, and thin PZT films do not affect noticeably the dynamic response of the structure. Our approach will yield good results for higher modes too and is valid for thick plates for which the thin plate theory may not yield satisfactory results. To demonstrate this, we have listed in Table 1.2 the first six natural frequencies for a $30\sqrt{2}$ cm $\times$ 30 cm $\times$ 4.04 cm plate similar to the one considered above except that each lamina is 0.4 cm thick as computed by the present method and also by the thin plate theory; the maximum difference between the two sets of results is 44%.

1.4.2 The Optimal Placement of an Actuator

An interesting exercise is to ascertain the optimal locations and sizes of actuators so that the energy is efficiently transferred to the structure (Bhargava et al. [1]). Such a problem is difficult to solve analytically. For the problem of the thin plate being studied herein, and as shown in the preceding section, the mass and rigidity of the thin piezoelectric films have a negligible effect on the dynamic response of the structure. We find the optimal location of the actuator as follows. Let the thin PZT films cover the entire surface of the plate, and the voltage be applied only on a rectangular region of the surface. By fixing the magnitude of the applied voltage and the size of the excited region, we move the rectangular region around and find the maximum out-of-plane displacement of a point on the midsurface of the plate. The optimal location(s) of the excited region will be that which results in the maximum value of the peak out-of-plane displacement since if the plate were initially vibrating at the frequency of the applied voltage, such a location will be most effective in suppressing these vibrations with the least amplitude of the applied voltage. Here we delineate the optimal location for modes 11, 21 and 22.

Figures 1.2 through 1.4 depict the peak value of the nondimensional displacement $U_3 = u_3/a$ versus the location of the centroid of the $a/10.5 \times b/10.5$ excited region. It is evident that for the three modes studied the optimal location of the centroid of the excited region (and hence of an actuator patch of size equal to that of the excited rectangular region) coincides with the point(s) where the amplitude of vibration is maximum. Thus for modes 11, 21 and 22, the optimal locations of the centroid of the excited region in the planes of the actuators are $(a/2,\ b/2)$; $(a/4,\ b/2)$ and $(3a/4,\ b/2)$; and $(a/4,\ b/4)$, $(a/4,\ 3b/4)$, $(3a/4,\ b/4)$ and $(3a/4,\ 3b/4)$ respectively. When the centroid of the excited region is located at a point on the nodal line consisting of points whose deflection for free vibrations of the plate is zero, the efficiency of actuation will be very poor.

Another part of the optimal placement of an actuator is to ascertain the optimal distance of the actuator layer from the neutral surface. Here we determine this for mode 11 and conjecture that the result will apply to higher modes too. We consider a laminated plate made of 20 substrate lamina arranged symmetrically as 0/90; the thickness of each substrate equals 0.2 mm and that of the PZT layer 0.01 mm. Keeping the centroid of the excited region at the centroid of the plate, the size of the excited region as $a/10.5 \times b/10.5$ and the voltage applied to it fixed, we move the actuator layer in the x_3-direction. Recall that we also have a PZT layer used as a sensor that is located symmetrically with respect to the neutral surface. We note that displacements are very sensitive to the frequency of the applied voltage when it is close to a natural frequency of the system, and Ω_{11} will vary slightly with the location of the actuator layer. In each case we take the non-dimensional frequency of the applied voltage to be 0.03 less than the corresponding Ω_{11}. As depicted in Fig. 1.5, the relation between the maximum out-of-plane displacement and the distance of the actuator layer from the neutral surface is essentially linear. Thus an optimum location

for the actuator is at a bounding surface of the plate. However, because of the assumption of embedded PZT layers, our analysis is not valid when the PZT layers are affixed to the top and bottom surfaces; those cases have been analyzed by Batra et al. [3]. Factors such as severe environment may suggest that it is better to have embedded PZTs.

For the $30\sqrt{2}$ cm $\times$ 30 cm $\times$ 0.404 cm plate, Fig. 1.6 shows that the maximum out-of-plane displacement depends nonlinearly upon the size of the excited region for mode 11. In each case the shape of the excited region, its centroid and the peak voltage applied with a frequency close to Ω_{11} are kept fixed. Since the applied voltage is a half sinusoidal wave, the resultant force and moment exerted by the forces between the actuator and the substrate layer depend nonlinearly upon the diagonal of the excited region.

Here we have kept the shape of the excited region as rectangular. Another possibility is to examine other shapes such as circular, elliptic etc. and also consider variations in the distribution of the voltage applied to this region. However, these numerous investigations have not been carried out here. One difficulty with shapes of the excited region other than a rectangular one is the evaluation of the integrals in equations (1.24) and (1.25). These can be evaluated analytically for a rectangular region. The evaluation of these integrals by a quadrature rule results in very high values of the shear stress at the quadrature points.

1.4.3 Structural Response

In the laminated rectangular plate made up of 10 graphite-epoxy lamina and 2 PZT layers, we assume that 3rd and 10th layers from the bottom are made of a PZT and the former acts as an actuator and the latter as a sensor. In the actuator's plane, the centroid of the excited region ($a/10.5 \times b/10.5$) is located at ($a/2,\ b/2$) for mode 11, ($a/4,\ b/2$) for mode 21 and ($a/4,\ b/4$) for mode 22 which were found to be optimal locations in the previous section. Figures 1.7 through 1.15 depict the distribution of the nondimensional displacement $U_\alpha = u_\alpha/a$ for modes 11, 21 and 22 respectively. It is clear that the magnitude of U_3 is about 100 times that of U_1 and U_2.

In order to check the integrity of the smart structure, we have plotted in Figures 1.16 through 1.21 the nondimensional shear stress $T_{31} = \tau_{31}/E_{11}$ at the lower interface between the actuator and the substrate, and at the lower interface between the sensor and the substrate. In the former case, the maximum shear stress occurs at a point in the excited rectangular region indicating the possibility of delamination there between the PZT layer and the substrate. Similar results were obtained by Hanagud and Kulkarni [23] for beams by the finite element method, for quasistatic deformations of plates by Zhou and Tiersten [17], and for steadily vibrating plates with no PZTs by Batra et al. [19]; References 17 and 19 used the elasticity theory. The magnitude of the maximum shear stress between the sensor and the substrate is about one-tenth that between the actuator and the substrate, and the jump in the shear

stress at any point is also considerably smaller than that in the excited region of the actuator. For the sensor/substrate interface, the shear stress in the region that is below the excited region is high indicating the possibility of delamination there. However, the risk of this happening is lower than that in excited actuator region because of an order-of-magnitude difference in the magnitude of the maximum shear stress in the two cases.

For the plate vibrating in mode 11, 21 or 22, Figures 1.22 through 1.24 depict the out-put electric voltage at the upper surface of the sensor layer; in each case the point where the magnitude of the out-put voltage is maximum coincides with the point of peak out-of-plane displacement.

The variation with respect to x_3, on a vertical line in the horizontal configuration of the plate through the point $(a/4, b/4, 0)$, of nondimensional displacement components and stress components for the thin and thick plates studied herein and vibrating at a frequency close to Ω_{11} are shown in Figures 1.25 through 1.27. Both for the thin and the thick plates, U_1 and U_2 vary linearly through the thickness; however they are an order of magnitude higher for the thin plate as compared to that for the thick plate. The variation of U_3 through the thickness is parabolic for the thin and thick plates but that for the thin plate is about 100 times that for the thick plate. The variation of different stress components in the thickness direction for the two plates is similar; as expected T_{11} and T_{22} exhibit discontinuities at the interfaces but other stress components are continuous as required by the coherency condition. Maximum values of T_{11}, T_{22} and T_{33} for the thin plate are nearly one-tenth of those for the thick plate; the peak values of other components of the stress tensor are essentially the same for the two plates.

1.5 Conclusions

We have studied steady state vibrations of a simply supported rectangular laminated elastic plate with embedded piezoelectric actuators and sensors by using the three-dimensional elasticity theory. The piezoelectric sensor and actuator layers are modeled as thin films and are assumed to be perfectly bonded to the adjoining lamina. Numerical results for a thin and a thick plate are presented. For very thin sensor and actuator layers, the mass and rigidity of the PZT material have negligible effects on the natural frequencies of a laminated thin plate. For a thin plate vibrating at a frequency close to Ω_{11}, Ω_{21} and Ω_{22}, the optimal locations of the centroid of the excited rectangular region coincide with the points where the displacement for the corresponding mode attains maximum values. The shear stress in the excited region is high indicating the possibility of delamination there; however, the delamination will first occur at an interface between the actuator and the lamina rather than that between the sensor and the lamina. The points of maximum sensor output coincide with those of peak out-of-plane displacement. For the thin and thick plates, U_1 and U_2 vary

nearly linearly with the distance from the midsurface but U_3 varies parabolically.

1.6 References

1. Bhargava, A., Chaudhry, Z., Liang, C. and Rogers, A.C., "Experimental Verification of Optimum Actuator Location and Configuration Based on Actuator Power Factor", *J. Intelligent Materials & Structures*, Vol. 6, 1995, pp. 411-418.

2. D'Cruz, J., "Global Multivariable Vibration Control with Distributed Piezoceramic Actuators," *J. Intelligent Materials & Structures*, Vol. 6, 1995, pp. 419-429.

3. Batra, R. C., Liang, X.Q., and Yang, J.S., "Shape Control of Vibrating Simply Supported Rectangular Plates", *AIAA J.*, Vol.34, No.1, 1996, pp.116-122.

4. Baz, A., and Poh, S., "Performance of an Active Control System with Piezoelectric Actuators", *Journal of Sound and Vibration*, Vol. 126, 1988, pp. 327-343.

5. Tzou, H.S., and Tseng, C.I., "Distributed Modal Identification and Vibration Control of Continua: Piezoelectric Finite Element Formulation and Analysis", *Journal of Dynamic Systems, Measurement and Control*, Vol. 113, 1991, pp. 501-505.

6. Crawley, E.F. and de Luis, J., "Use of Piezoelectric Actuators as Elements of Intelligent Structures", *AIAA J.*, Vol. 25, 1987, pp. 1373-1385.

7. Tauchert, T.R., "Piezothermoelastic Behavior of a Laminated Plate", *J. Thermal Stresses*, Vol. 15, 1992, pp. 25-37.

8. Tang, Y.Y., and Xu, K., "Dynamic Analysis of Piezothermoelastic Laminate Plate", *J. Thermal Stresses*, Vol. 17, 1994, pp. 87-104.

9. Mitchell, J.A. and Reddy, J.N., "A Refined Hybrid Plate Theory for Composite Laminates with Piezoelectric Laminae", *Int. J. Solids & Structures*, Vol. 32, 1995, pp. 2345-2368.

10. Ghosh, K., and Batra, R.C., "Shape Control of Plates Using Piezoceramic Elements", *AIAA J.*, Vol. 33, 1995, pp. 1354-1357.

11. Batra, R.C., and Ghosh, K., "Deflection Control During Dynamic Deformations of a Rectangular Plate Using Piezoceramic Elements", *AIAA J.*, Vol. 33, 1995, pp. 1547-1548.

12. Ray, M.C.H., Rao, K.M., and Samanta, B., "Exact Solution for Static Analysis of an Intelligent Structure Under Cylindrical Bending", *Computers & Structures*, Vol. 47, 1993, pp. 1031-1042.

13. Lagoudas, D.C., and Bo, Z., "The Cylindrical Bending of Composite Plates with Piezoelectric and SMA Layers", *Smart Materials & Structures*, Vol. 3, 1994, pp. 309-317.

14. Brooks, S. and Heyliger, P., "Static Behavior of Piezoelectric Laminates with Distributed and Patched Actuators", *J. Intelligent Materials & Structures*, Vol. 5, 1994, pp. 635-646.

15. Srinivas S., Rao, C.V.J. and Rao, A.K., "An Exact Analysis of Vibration of Simply-Supported Homogeneous and Laminated Thick Rectangular Plates", *J. Sound Vib.*, Vol. 12, 1970, pp. 257-269.

16. Wittrick, W.H., "Analytical, Three-dimensional Elasticity Solutions to Some Plate Problems, and Some Observations on Mindlin's Plate Theory", *Int. J. Solids Structures*, Vol. 23, 1987, pp. 441-464.

17. Zhou, Y.S., and Tiersten, H.F., "Elastic Analysis of Laminated Composite Plates in Cylindrical Bending due to Piezoelectric Actuators", *Smart Materials & Structures*, Vol. 3, 1994, pp. 225-265.

18. Yang, J.S., Batra, R.C. and Liang, X.Q., "The Cylindrical Bending Vibration of a Laminated Elastic Plate due to Piezoelectric Actuators", *Smart Materials & Structures*, Vol. 3, 1994, pp. 485-493.

19. Batra, R.C., Liang, X.Q., and Yang, J.S., "The Vibration of a Simply Supported Rectangular Elastic Plate due to Piezoelectric Actuators", *International J. Solids & Structures*, Vol.33, No.11, 1996, pp.1597-1618.

20. Tiersten, H.F., "Electroelastic Equations for Electroded Thin Plates Subject to Large Driving Voltages", *Journal Applied Physics*, Vol. 74, 1993, pp. 3389-3393.

21. Mindlin, R.D., "High Frequency Vibrations of Plated Crystal Plates", *Progress in Applied Mechanics*, The Prager Anniversary Volume, MacMillan, New York, 1963, pp. 73-84.

22. Jones, R.M., *Mechanics of Composite Materials*, Scripta Book Co., Washington, D.C., 1975.

23. Hanagud S. and Kulkarni G., "Coupled Piezoceramic-elastic Structures with Finite Deformations", Developments in Theoretical and Applied Mechanics (*Proc. 16th Southeastern Conference on Theoretical and Applied Mechanics*) eds. B. Antar, R. Engels, A.A. Prinaris and T.H. Moulden, University of Tennessee Space Institute, Vol. XVI, pp. 22-30.

Table 1.1 A comparison of the first six natural frequencies for a $30\sqrt{2}$ cm $\times 30$ cm $\times 0.404$ cm simply supported laminated plate as computed by the thin plate theory and the present analysis employing the 3-dimensional linear elasticity theory.

	Ω_{11}	Ω_{21}	Ω_{12}	Ω_{22}	Ω_{31}	Ω_{32}
Thin-plate Theory	2.002	4.585	6.408	8.007	9.454	11.938
present analysis (3-D Theory)	1.944	4.456	6.152	7.736	9.128	11.528
% difference	3.0	2.6	4.0	3.3	3.5	3.0

Table 1.2 A comparison of the first six natural frequencies for a $30\sqrt{2}$ cm $\times 30$ cm $\times 4.04$ cm simply supported laminated plate as computed by the thin plate theory and the present analysis employing the 3-dimensional linear elasticity theory.

	Ω_{11}	Ω_{21}	Ω_{12}	Ω_{22}	Ω_{31}	Ω_{32}
Thin-plate Theory	1.975	4.570	6.284	7.900	9.444	11.858
present analysis (3-D Theory)	1.664	3.276	4.021	4.992	5.443	6.657
% difference	15.75	28.32	36.01	36.81	42.37	43.86

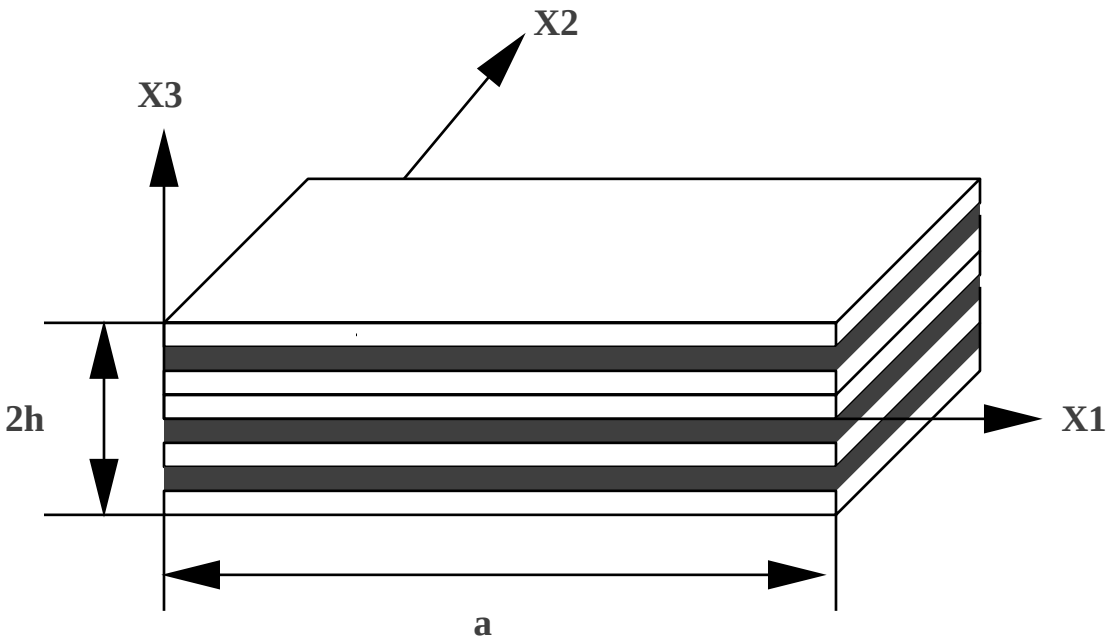

Figure 1.1: A schematic sketch of the problem studied

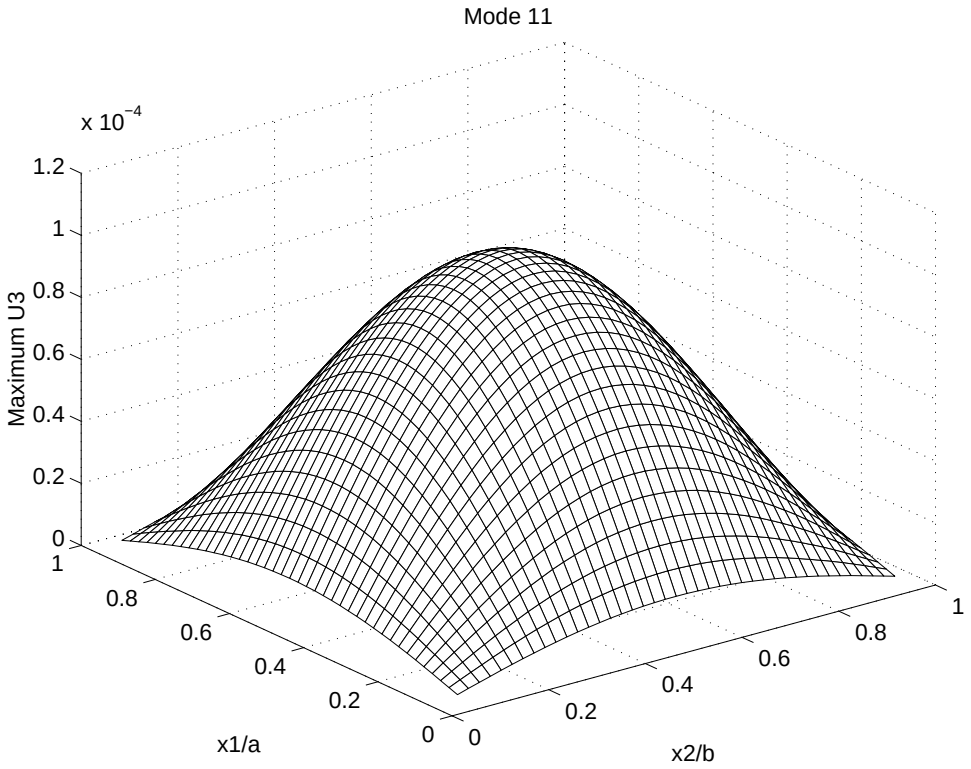

Figure 1.2: Peak value of the nondimensional out-of-plane displacement versus the location of the centroid of the excited rectangular region for the thin plate vibrating at a frequency close to Ω_{11}.

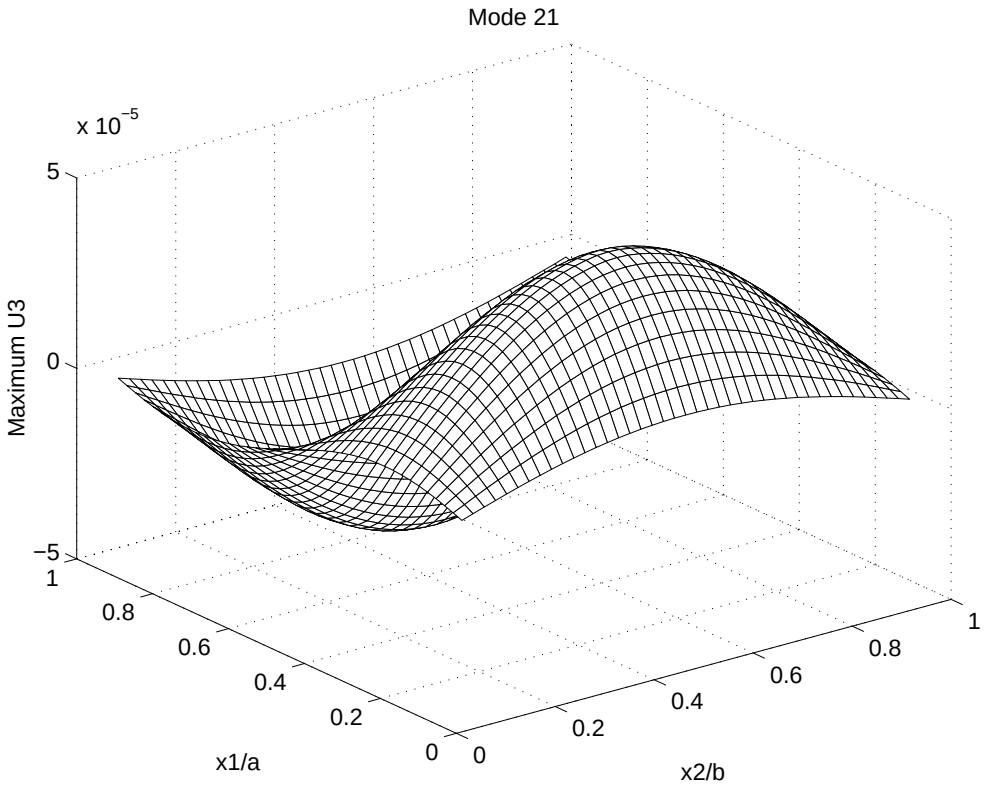

Figure 1.3: Peak value of the nondimensional out-of-plane displacement versus the location of the centroid of the excited rectangular region for the thin plate vibrating at a frequency close to Ω_{21}.

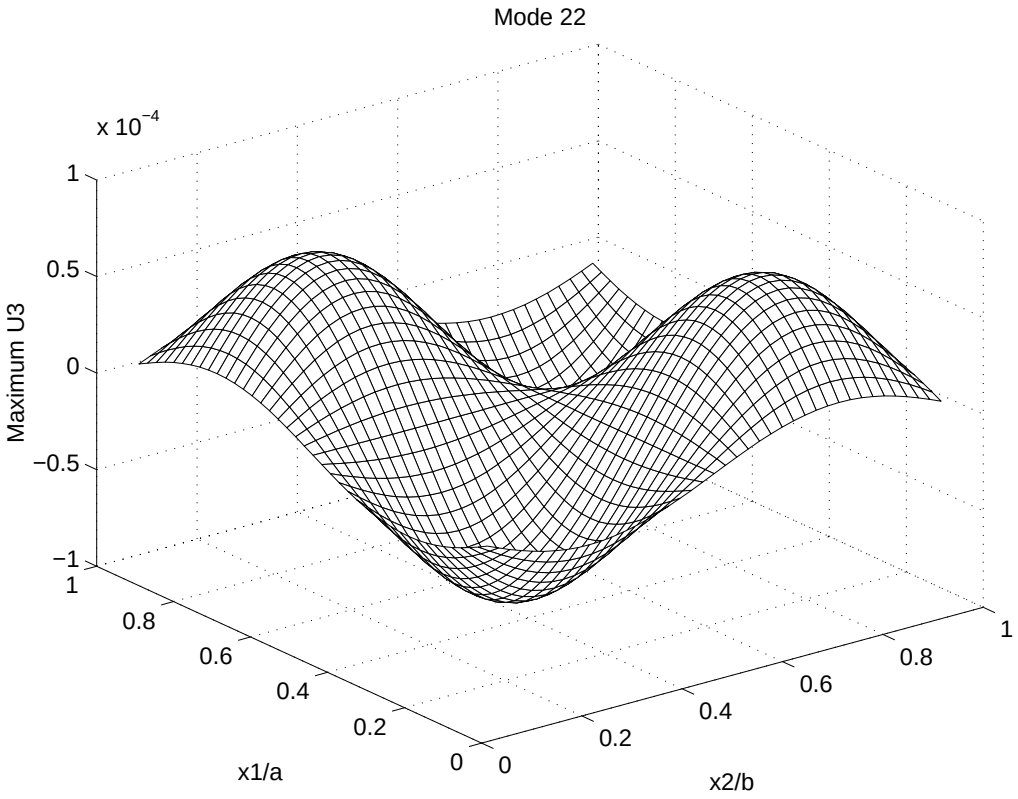

Figure 1.4: Peak value of the nondimensional out-of-plane displacement versus the location of the centroid of the excited rectangular region for the thin plate vibrating at a frequency close to Ω_{22}.

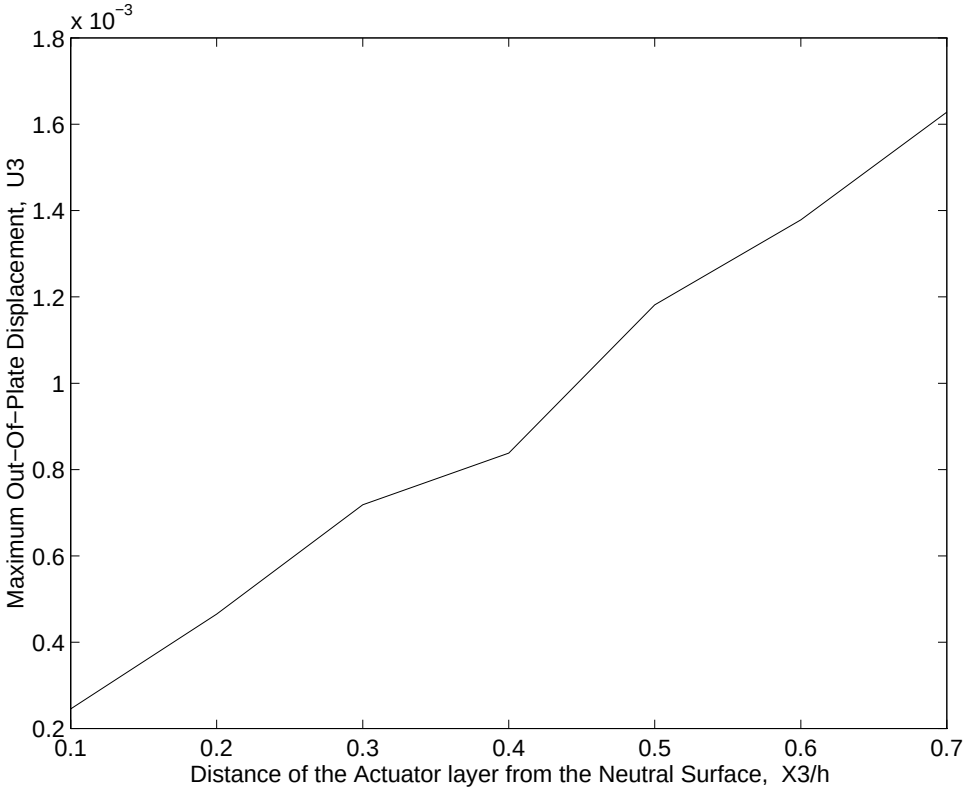

Figure 1.5: Peak out-of-plane displacement versus the distance of the actuator layer from the neutral surface for the $30\sqrt{2}$ cm $\times$ 30 cm $\times$ 0.404 cm plate.

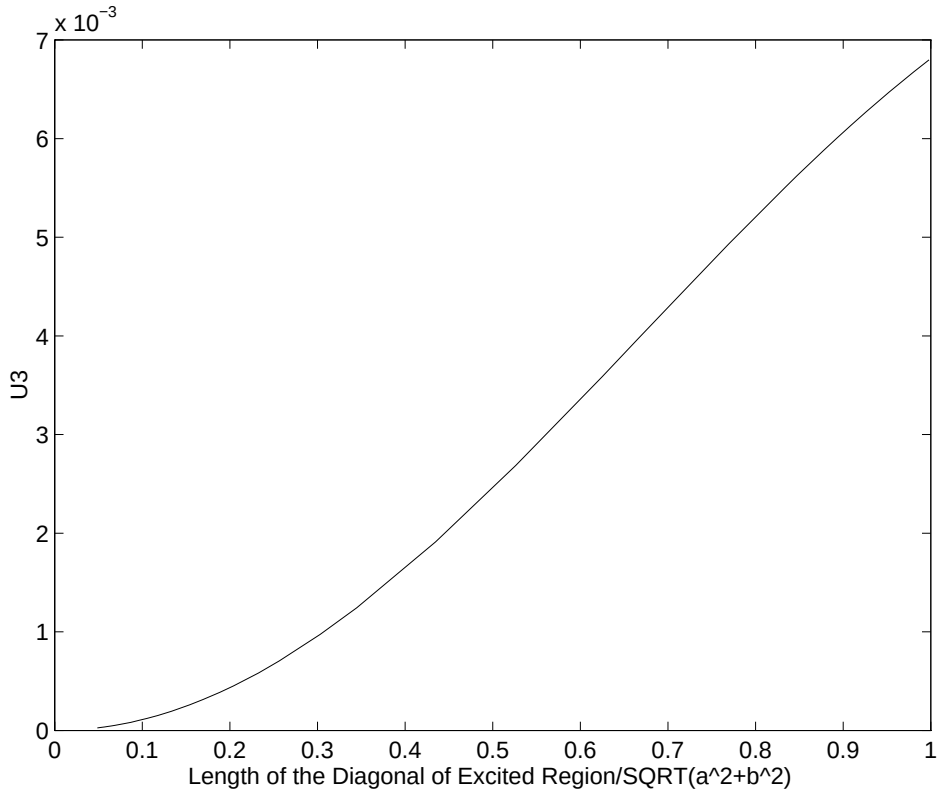

Figure 1.6: Maximum out-of-plane displacement versus the length of the diagonal of the rectangular excited region for the $30\sqrt{2}$ cm $\times$ 30 cm $\times$ 0.404 cm plate.

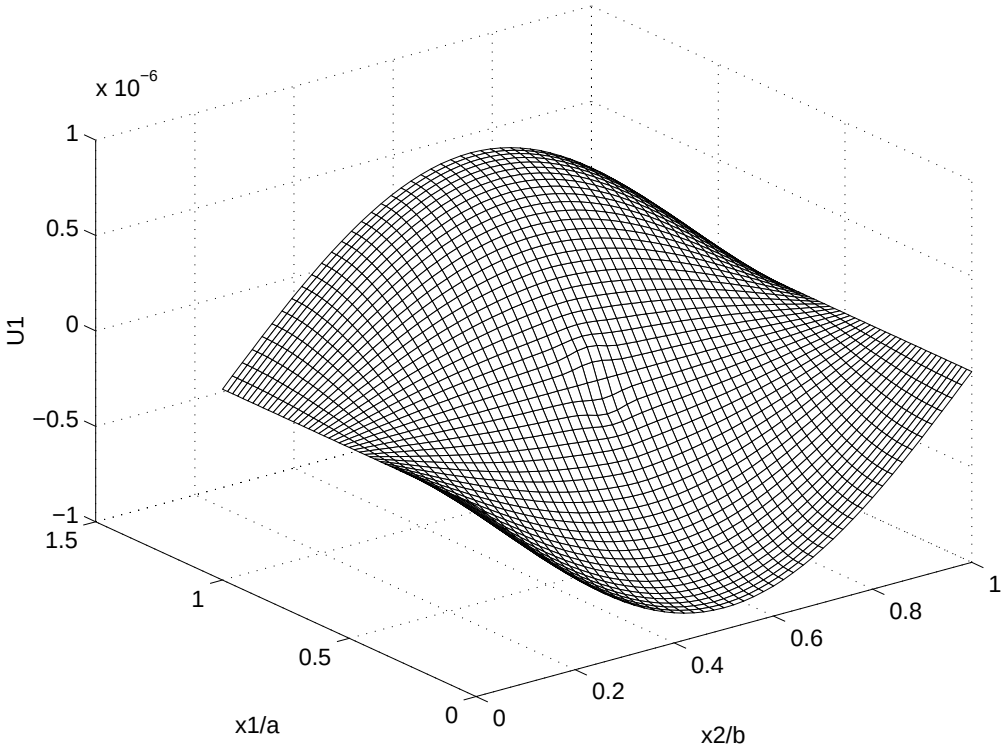

Figure 1.7: Distribution of the non-dimensional displacement U_1 for a thin plate vibrating at a frequency close to Ω_{11}.

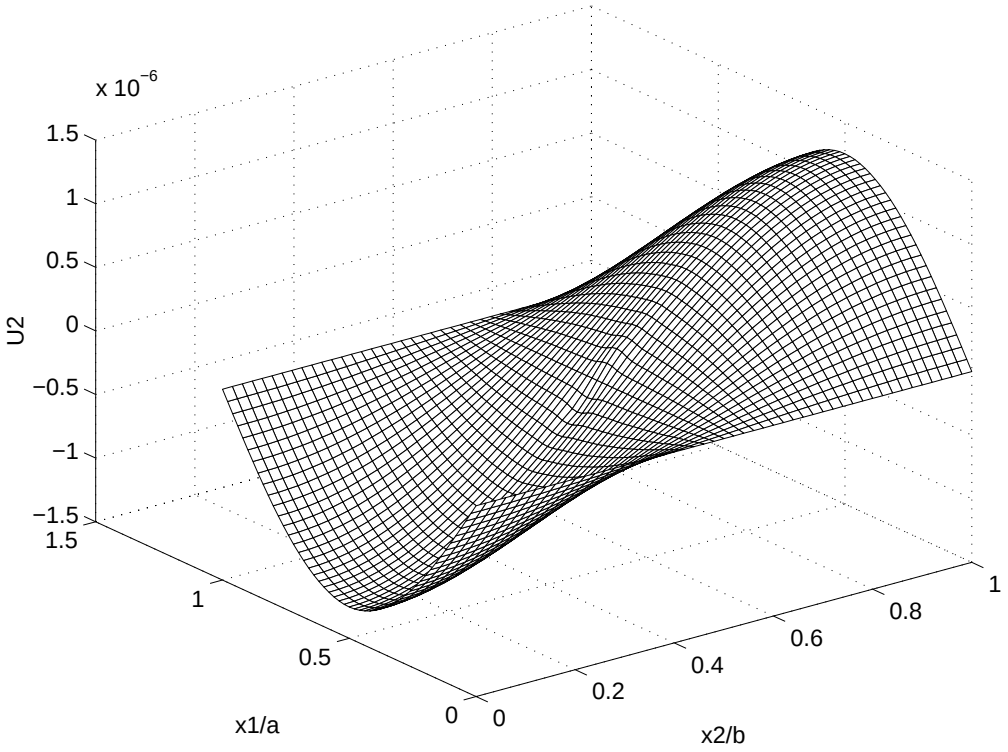

Figure 1.8: Distribution of the non-dimensional displacement U_2 for a thin plate vibrating at a frequency close to Ω_{11}.

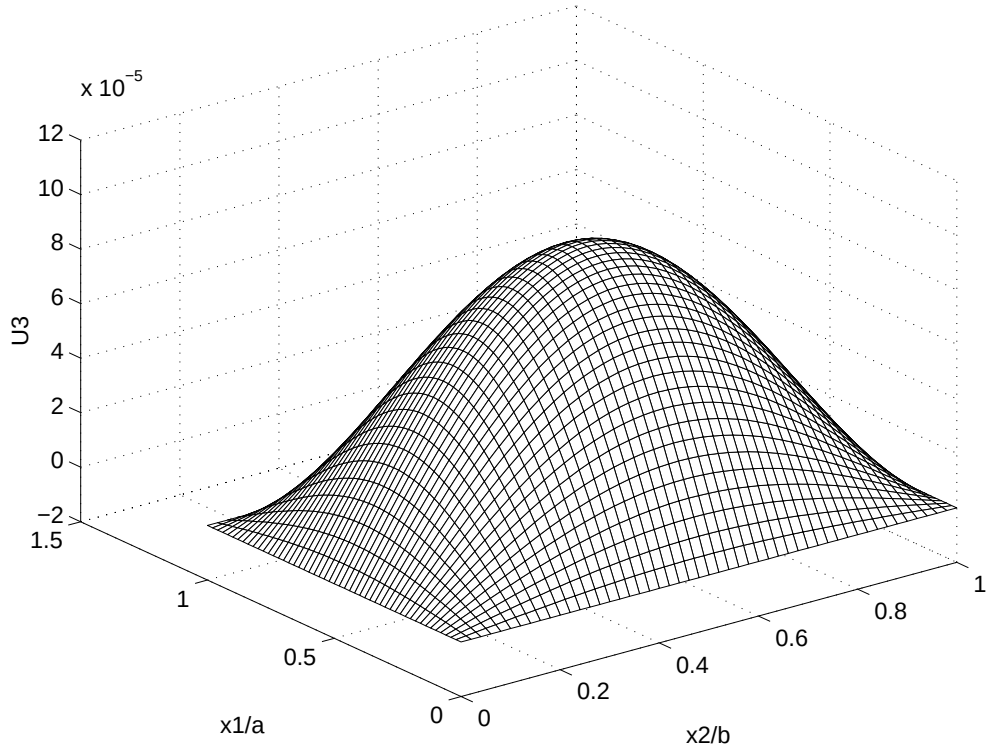

Figure 1.9: Distribution of the non-dimensional displacement U_3 for a thin plate vibrating at a frequency close to Ω_{11}.

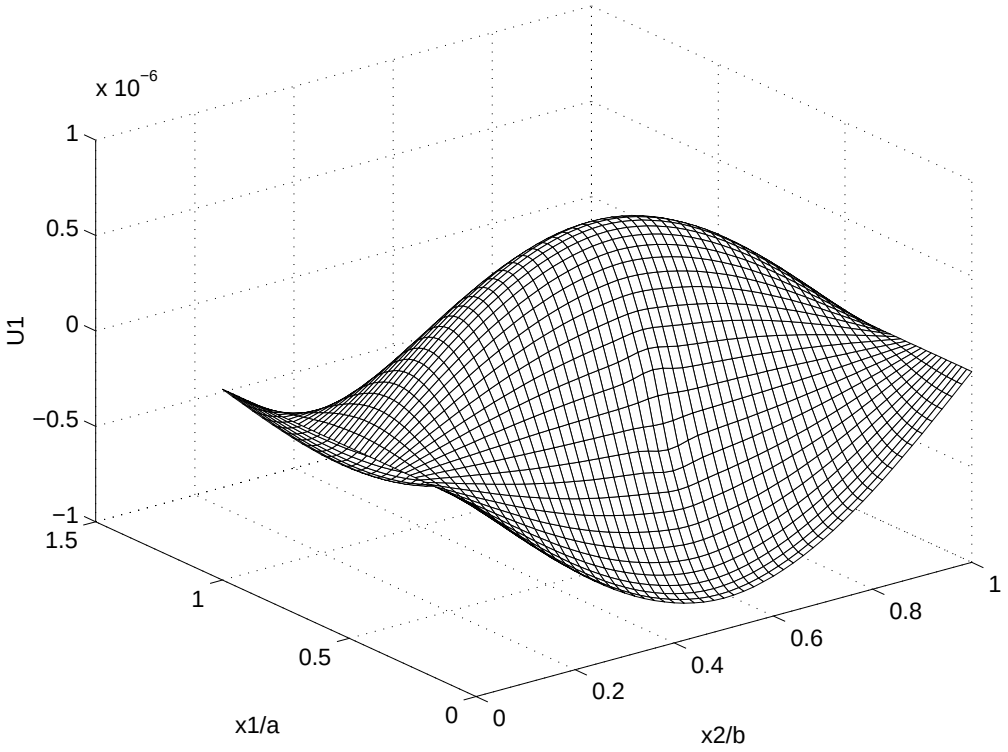

Figure 1.10: Distribution of the non-dimensional displacement U_1 for a thin plate vibrating at a frequency close to Ω_{21}.

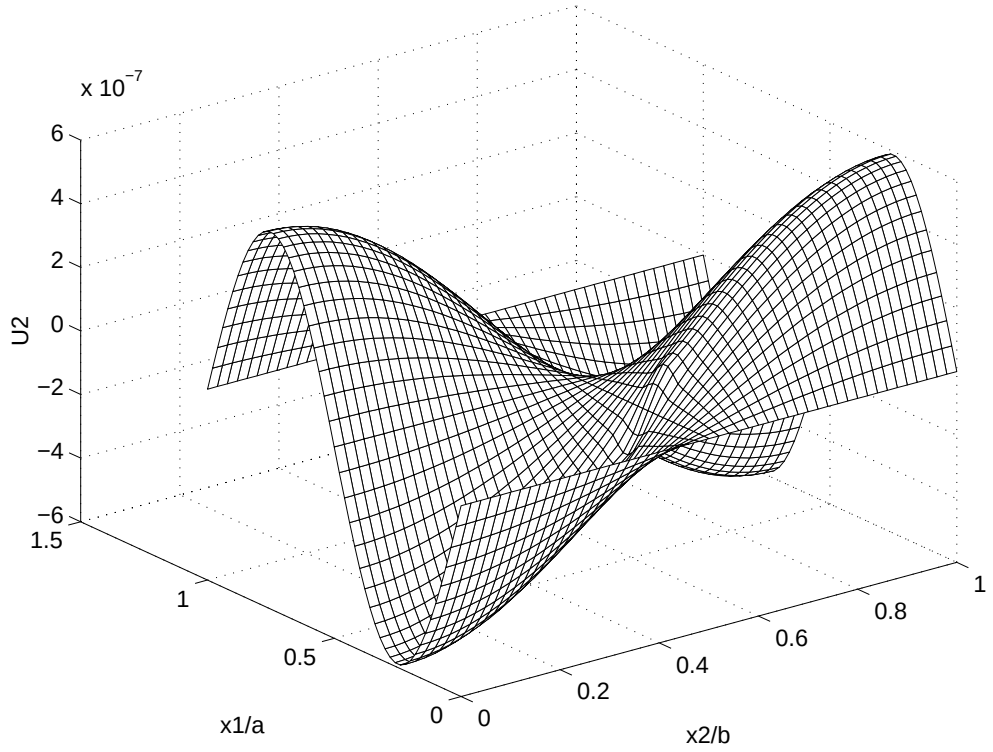

Figure 1.11: Distribution of the non-dimensional displacement U_2 for a thin plate vibrating at a frequency close to Ω_{21}.

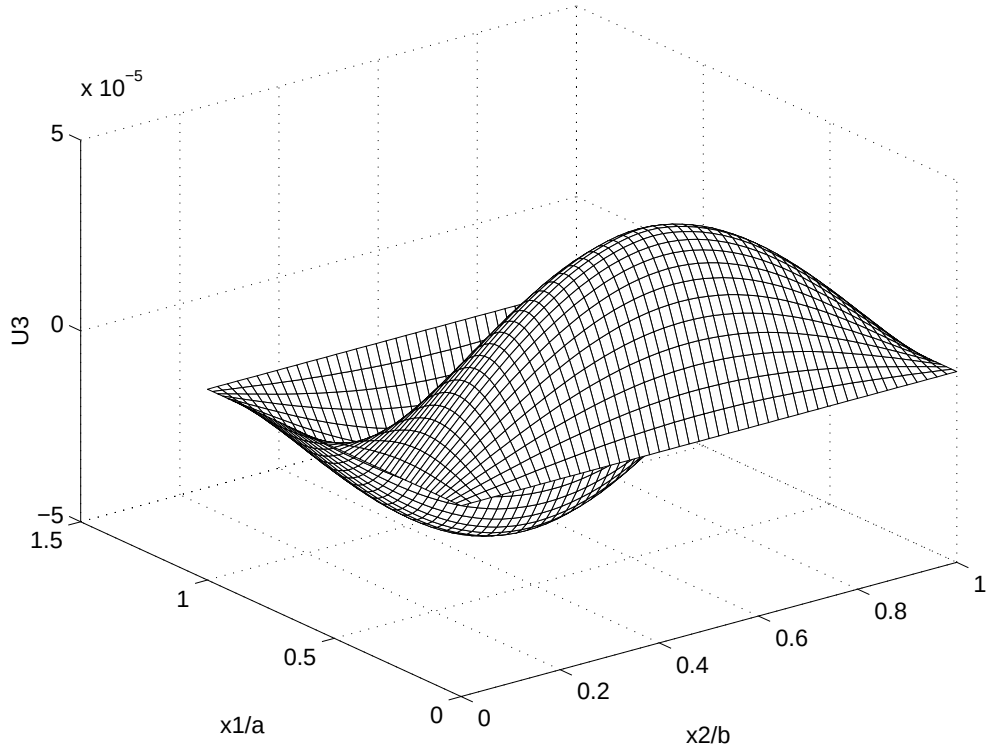

Figure 1.12: Distribution of the non-dimensional displacement U_3 for a thin plate vibrating at a frequency close to Ω_{21}.

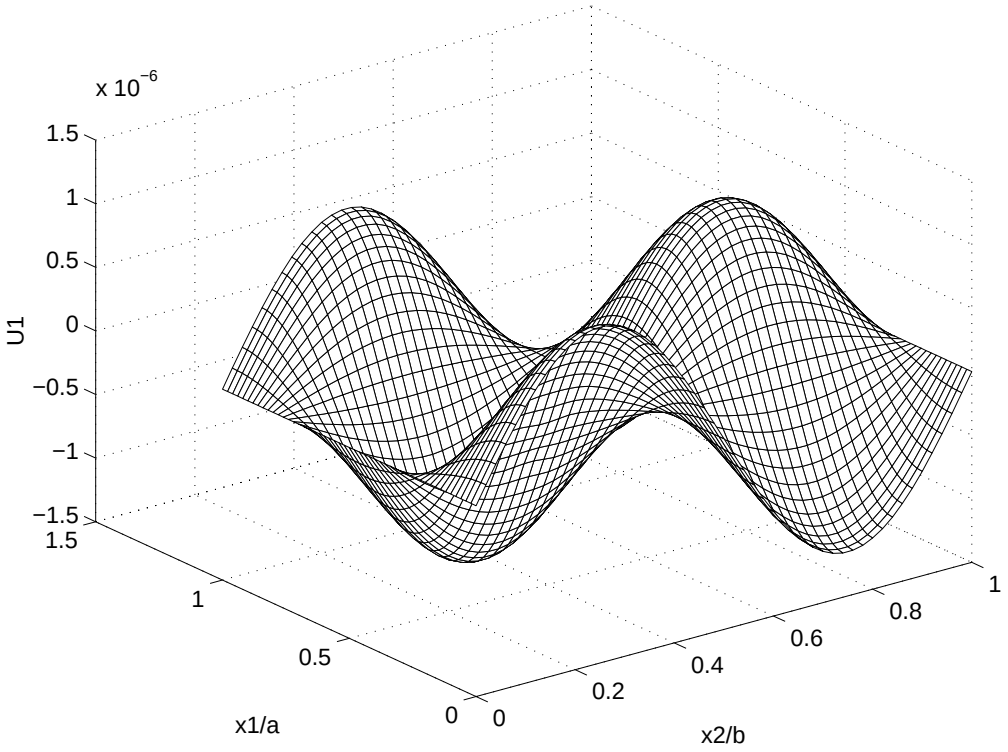

Figure 1.13: Distribution of the non-dimensional displacement U_1 for a thin plate vibrating at a frequency close to Ω_{22}.

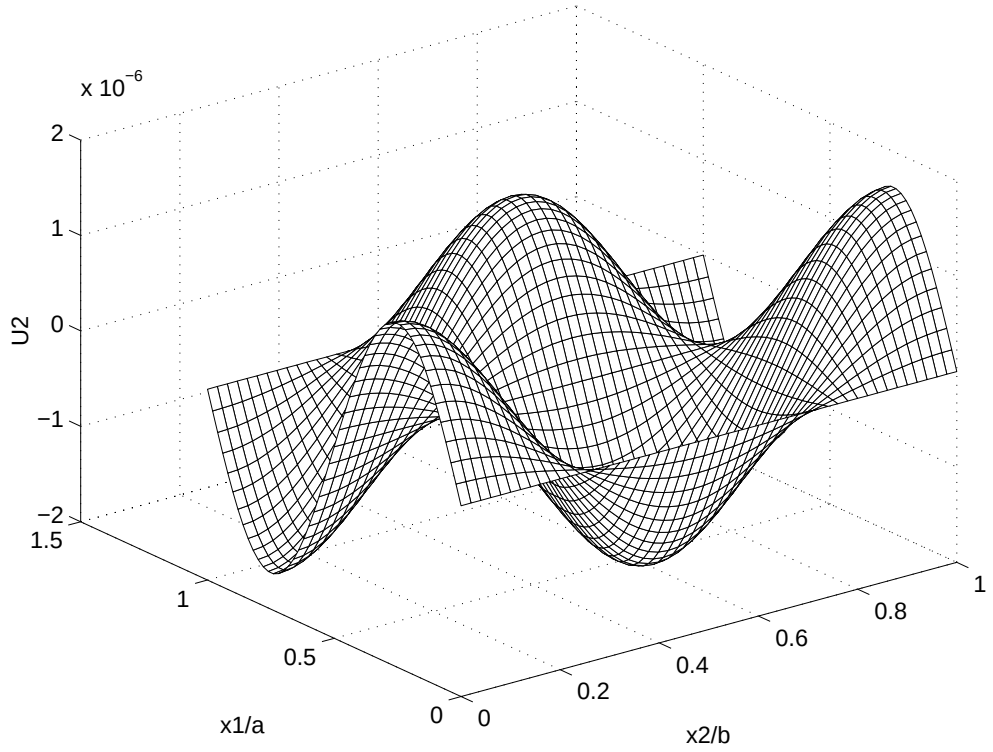

Figure 1.14: Distribution of the non-dimensional displacement U_2 for a thin plate vibrating at a frequency close to Ω_{22}.

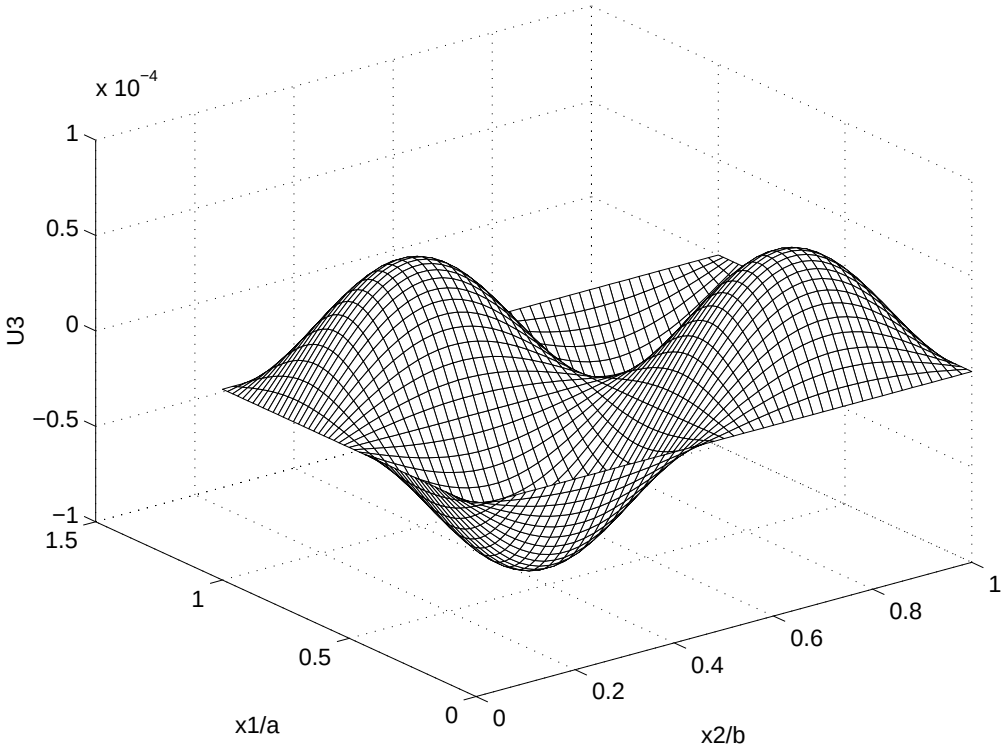

Figure 1.15: Distribution of the non-dimensional displacement U_3 for a thin plate vibrating at a frequency close to Ω_{22}.

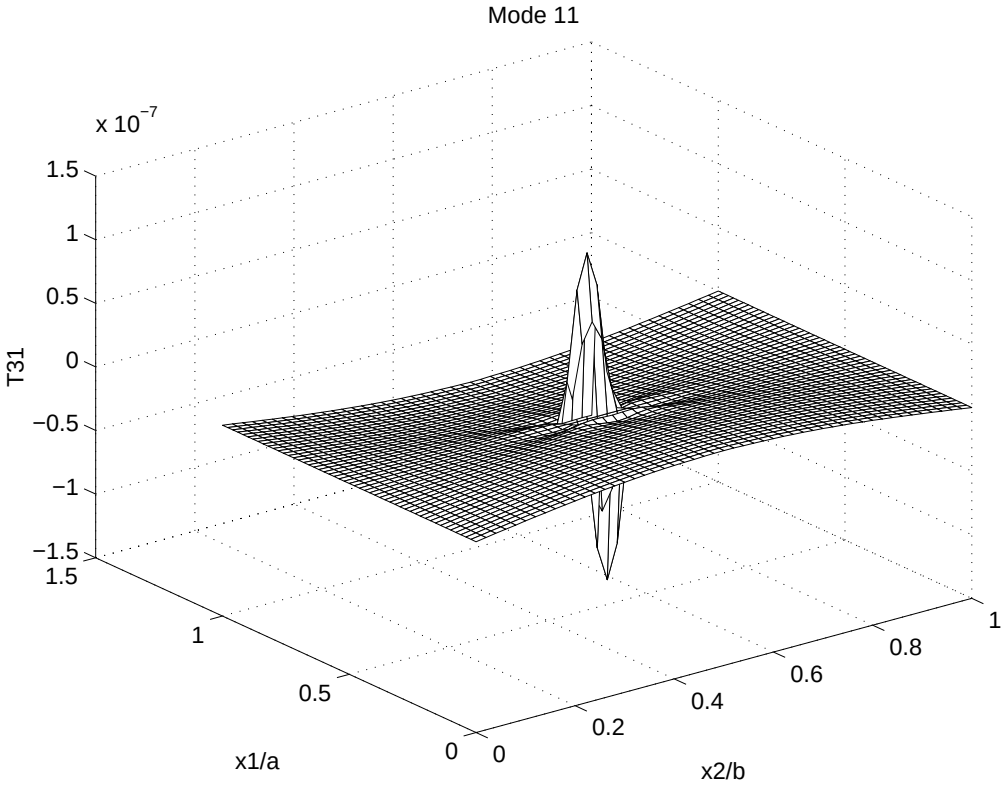

Figure 1.16: Distribution of the nondimensional shear stress T_{31} at the lower interface between the actuator and the substrate for a thin plate vibrating at a frequency close to Ω_{11}.

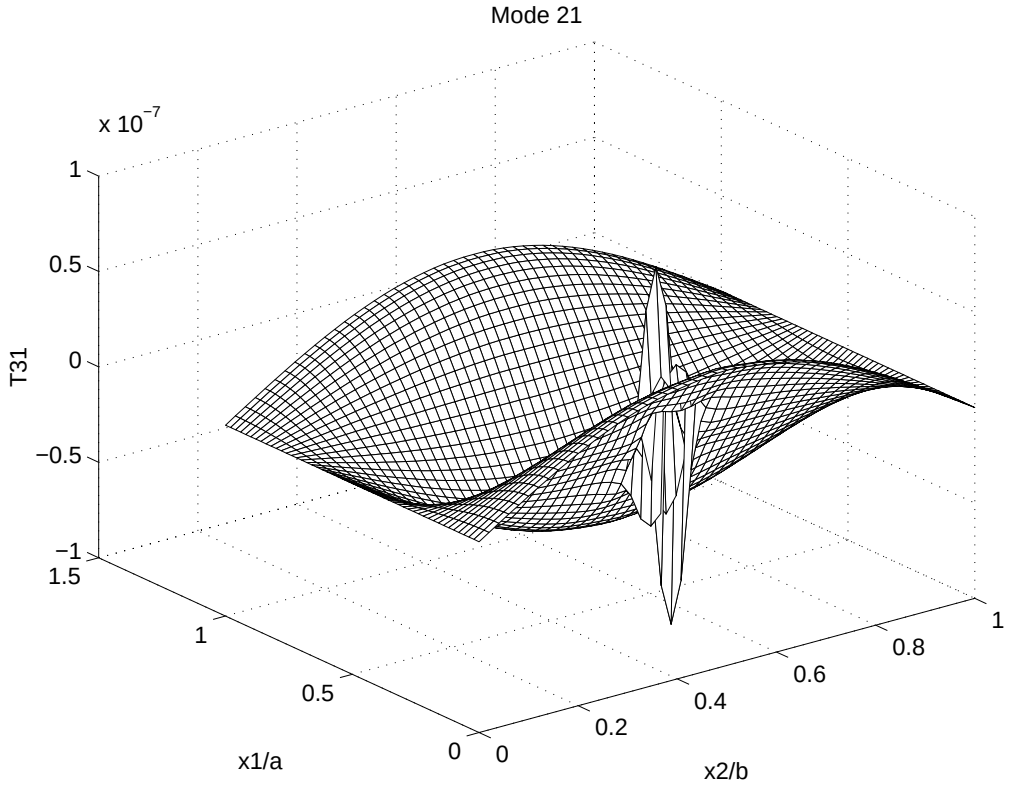

Figure 1.17: Distribution of the nondimensional shear stress T_{31} at the lower interface between the actuator and the substrate for a thin plate vibrating at a frequency close to Ω_{21}.

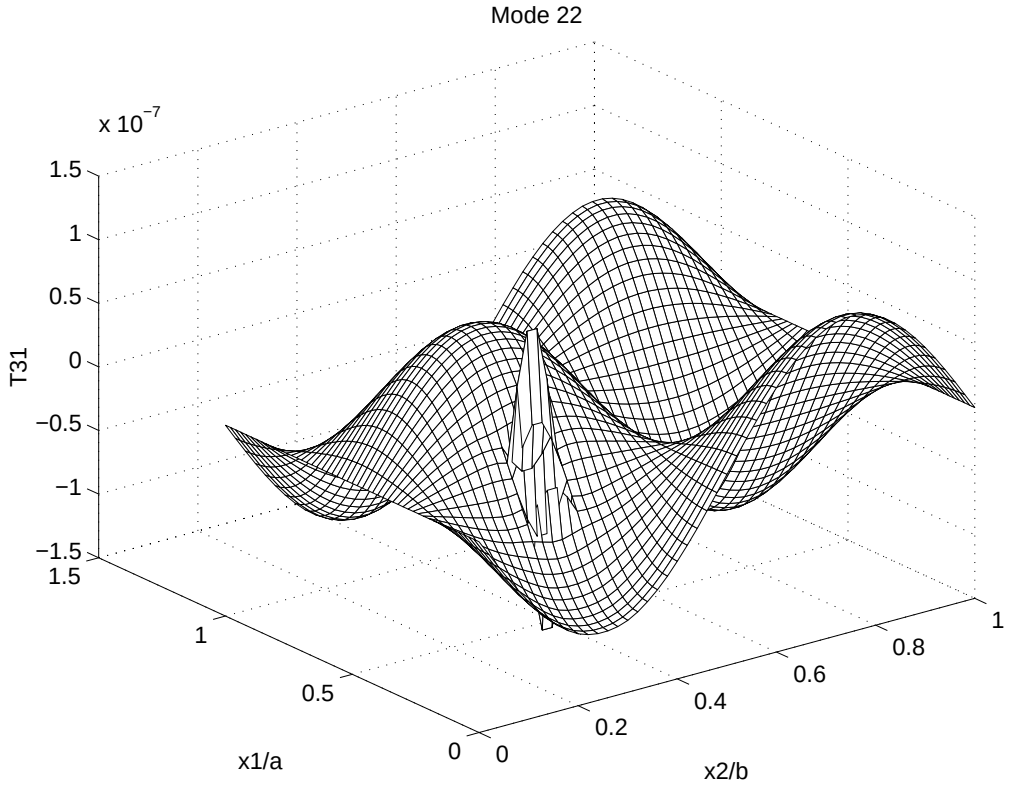

Figure 1.18: Distribution of the nondimensional shear stress T_{31} at the lower interface between the actuator and the substrate for a thin plate vibrating at a frequency close to Ω_{22}.

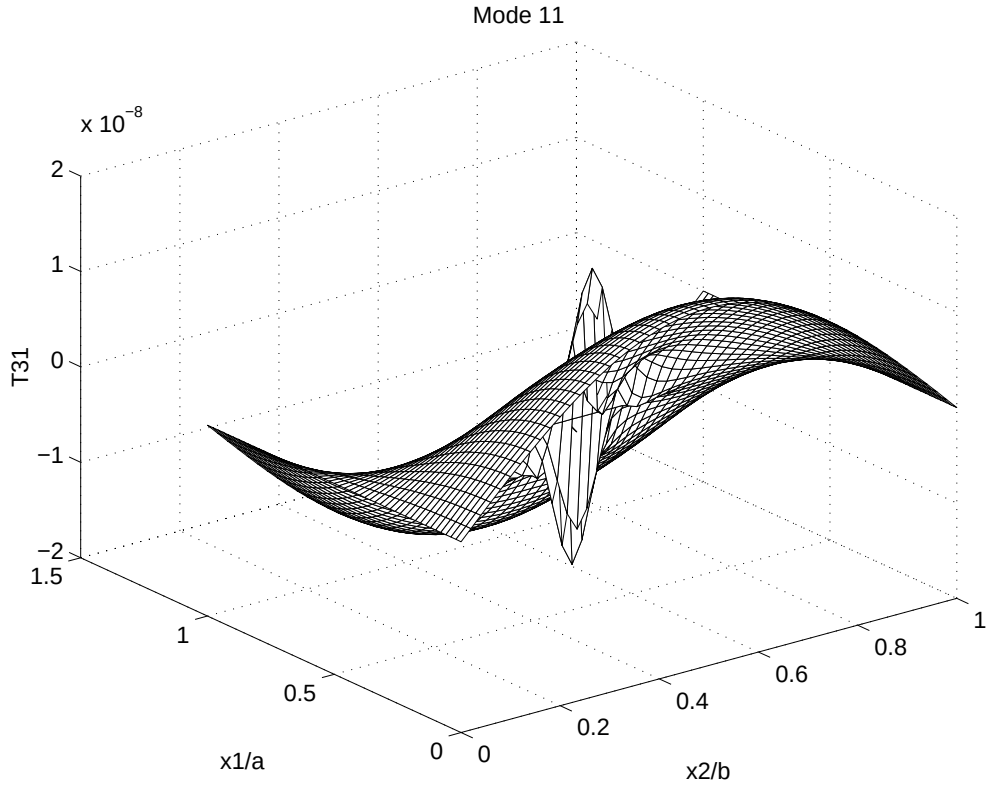

Figure 1.19: Distribution of the nondimensional shear stress T_{31} at the lower interface between the sensor and the substrate for a thin plate vibrating at a frequency close to Ω_{11}.

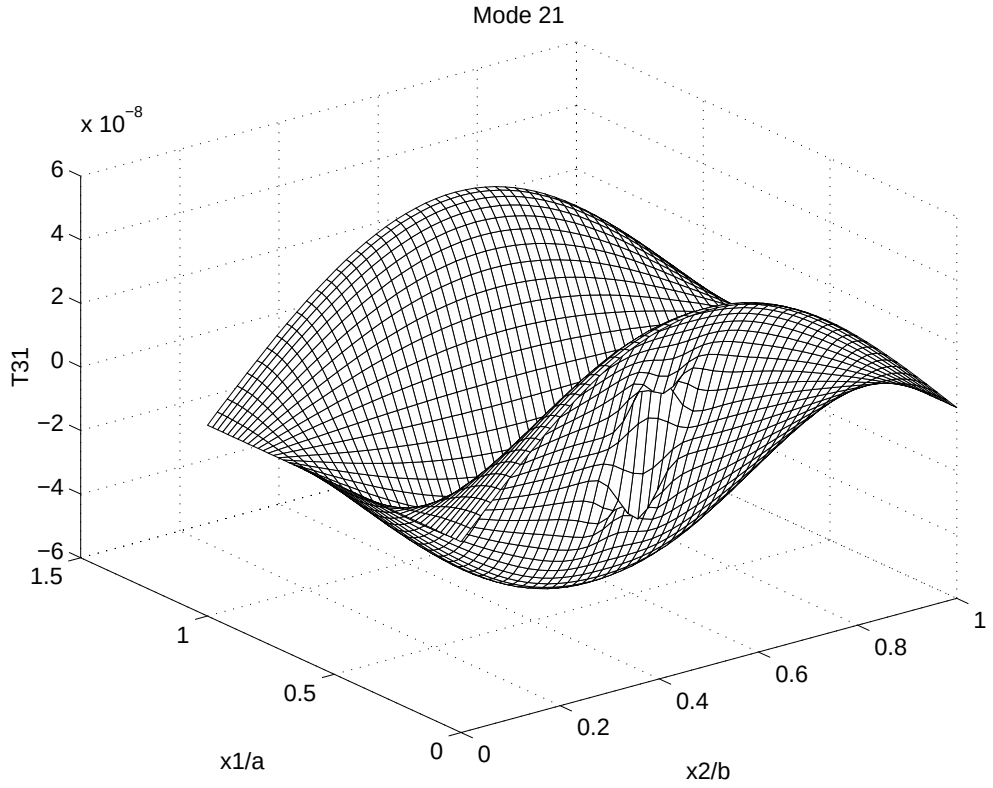

Figure 1.20: Distribution of the nondimensional shear stress T_{31} at the lower interface between the sensor and the substrate for a thin plate vibrating at a frequency close to Ω_{21}.

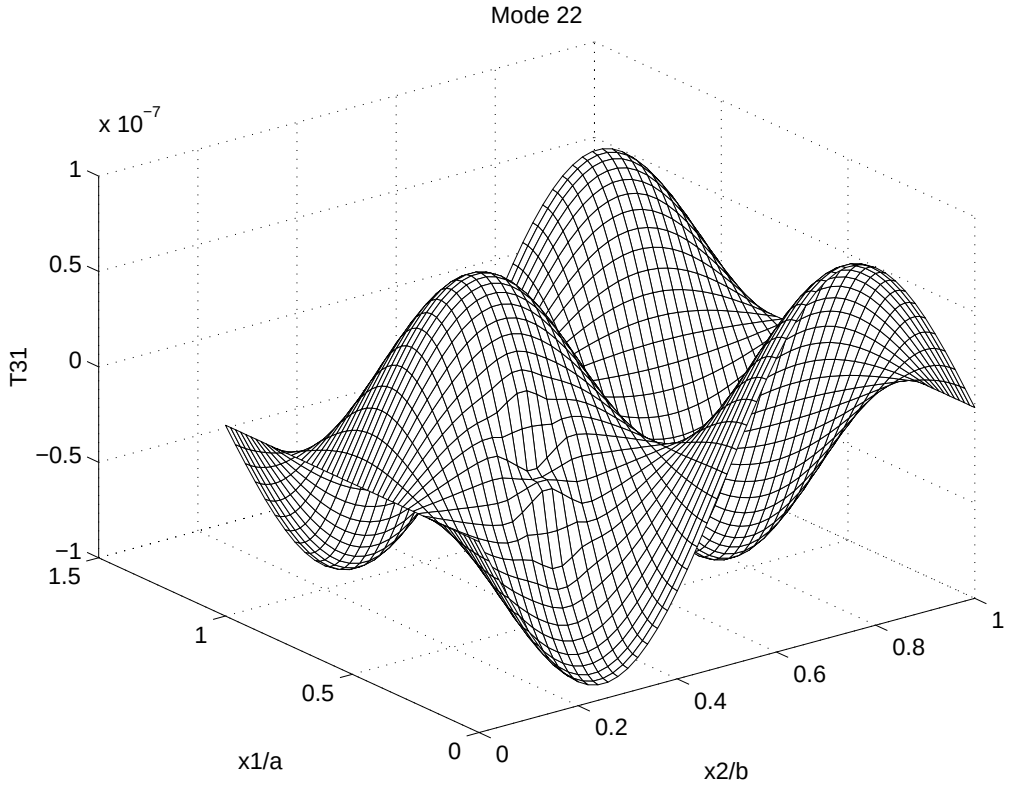

Figure 1.21: Distribution of the nondimensional shear stress T_{31} at the lower interface between the sensor and the substrate for a thin plate vibrating at a frequency close to Ω_{22}.

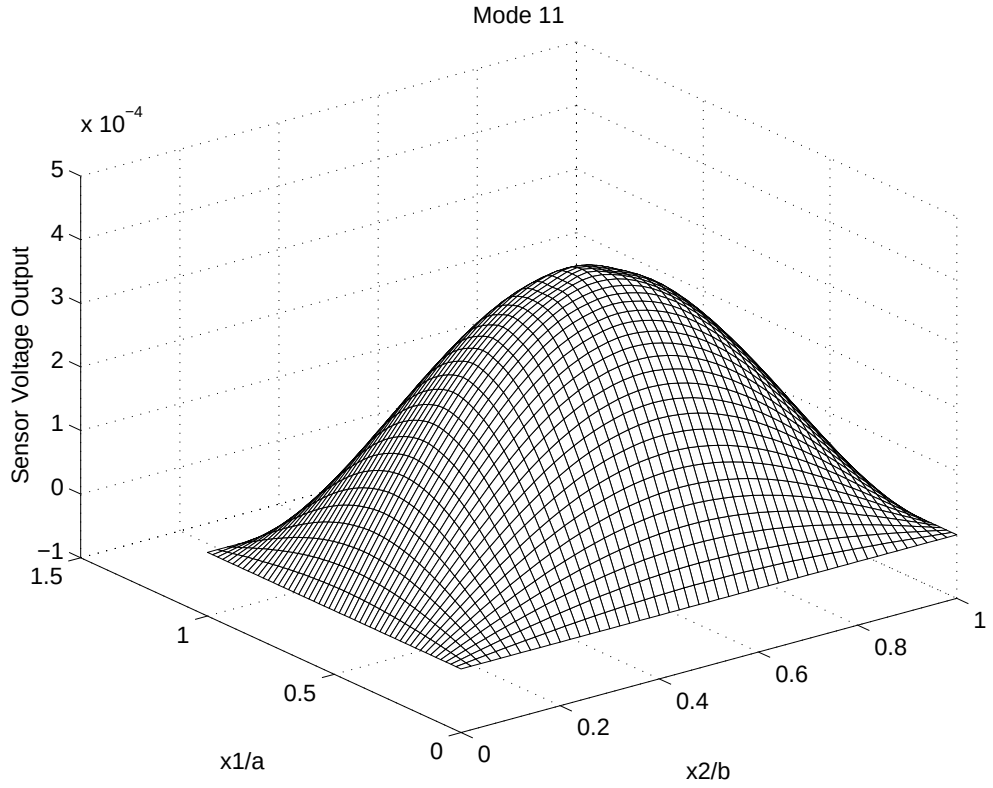

Figure 1.22: Distribution of the normalized electric voltage V/(200 volts) at the upper surface of the PZT sensor for a thin plate vibrating at a frequency close to Ω_{11}.

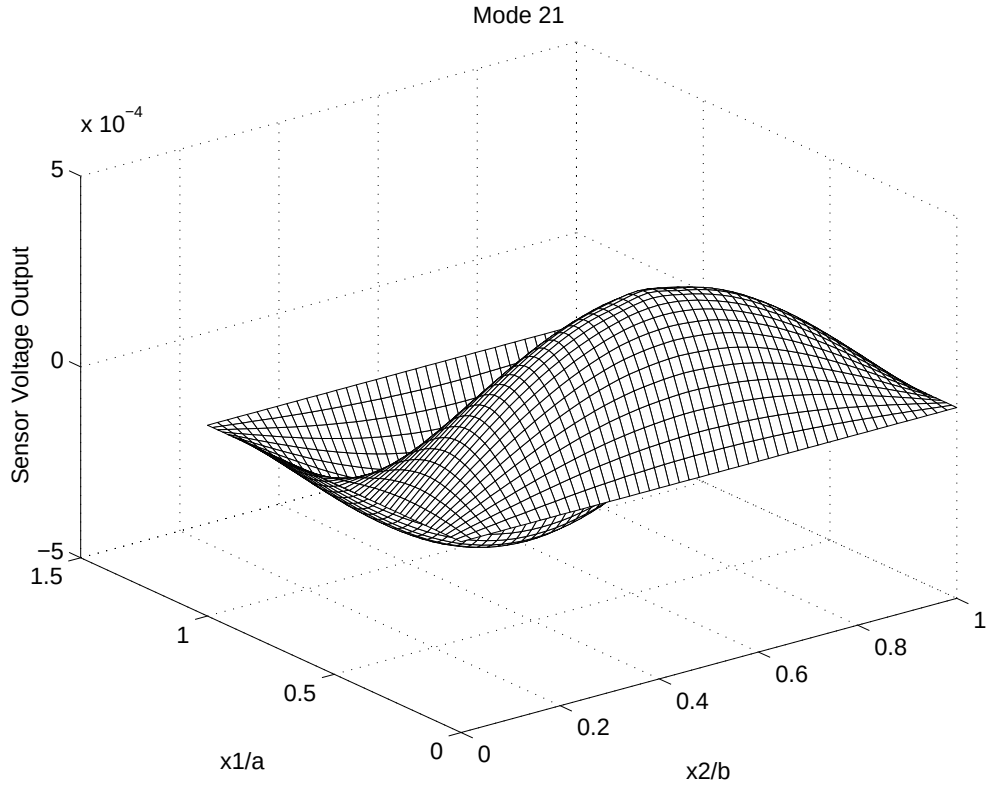

Figure 1.23: Distribution of the normalized electric voltage V/(200 volts) at the upper surface of the PZT sensor for a thin plate vibrating at a frequency close to Ω_{21}.

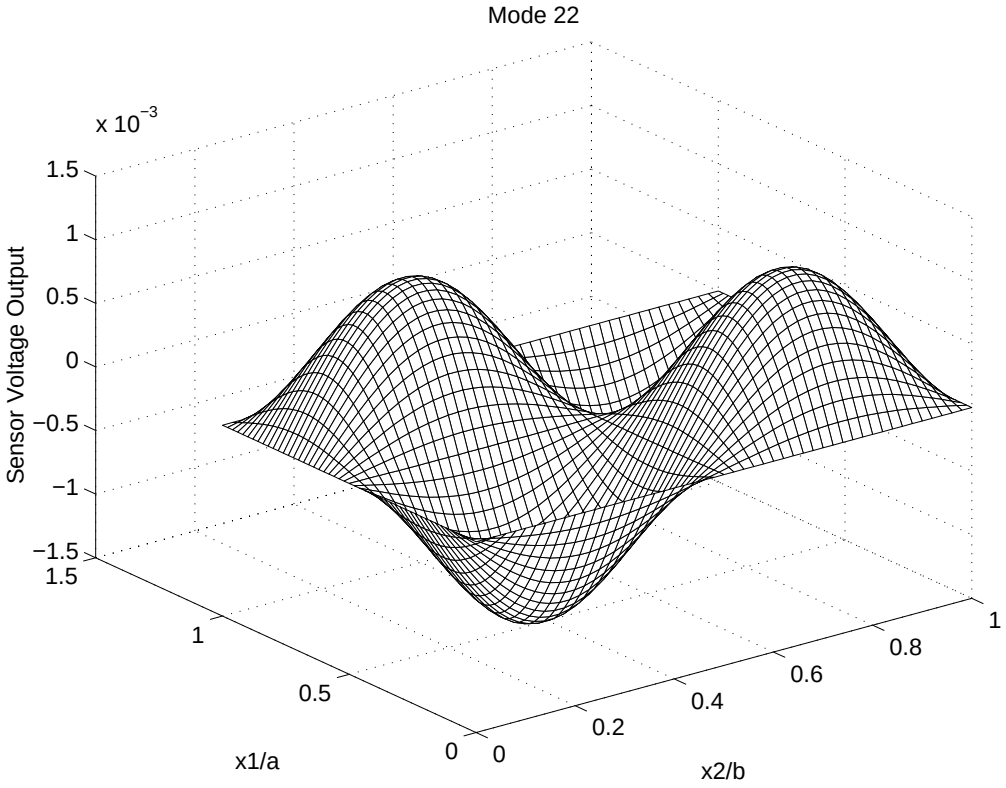

Figure 1.24: Distribution of the normalized electric voltage V/(200 volts) at the upper surface of the PZT sensor for a thin plate vibrating at a frequency close to Ω_{22}.

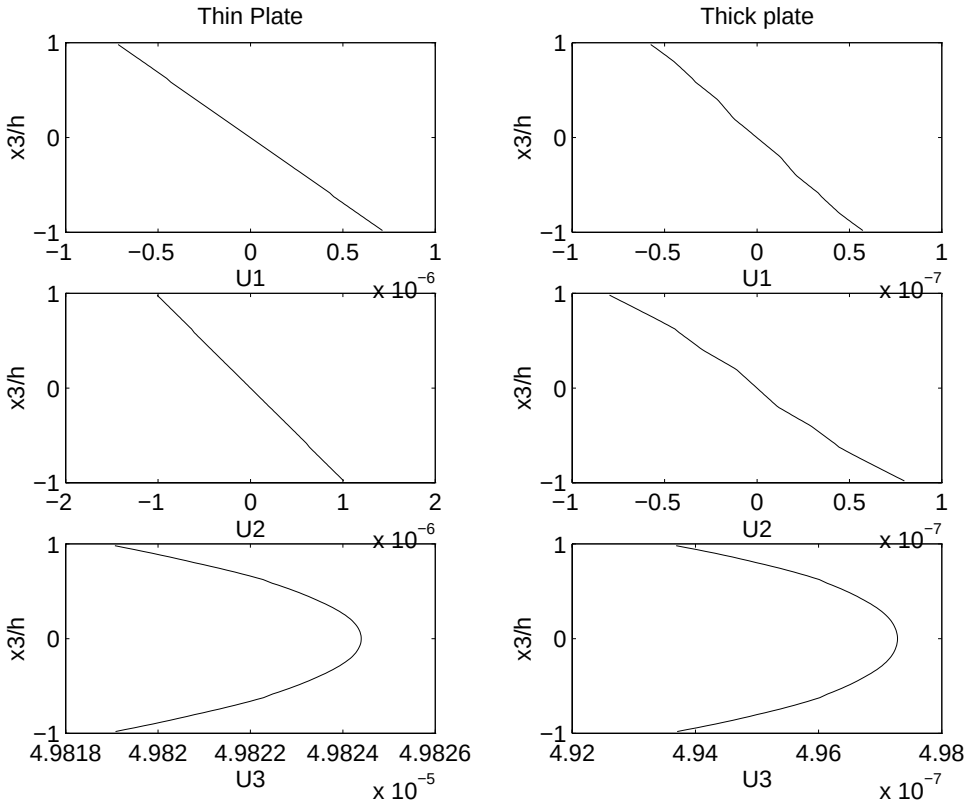

Figure 1.25: Variations of the non-dimensional displacement components on a vertical line through the point $\left(\frac{a}{4}, \frac{b}{4}, 0\right)$ for a thin and a thick plate vibrating at a frequency close to Ω_{11}.

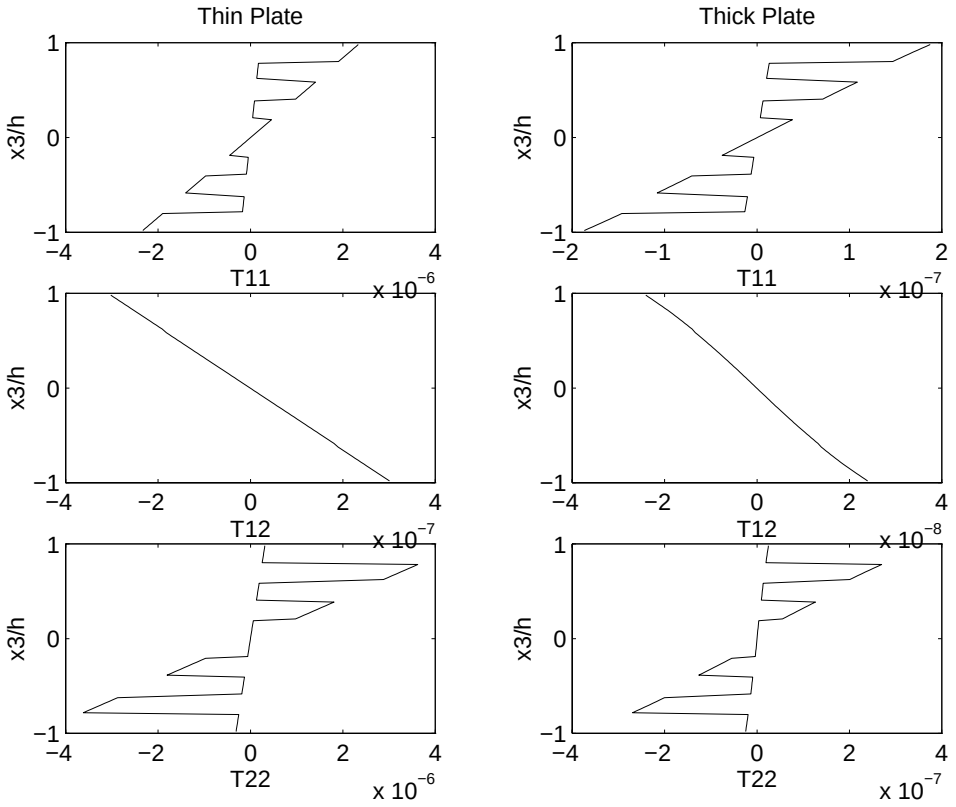

Figure 1.26: Variations through the thickness of the nondimensional in-plane stress components at the point $\left(\frac{a}{4}, \frac{b}{4}, .\right)$ for a thin and a thick plate vibrating at a frequency close to Ω_{11}.

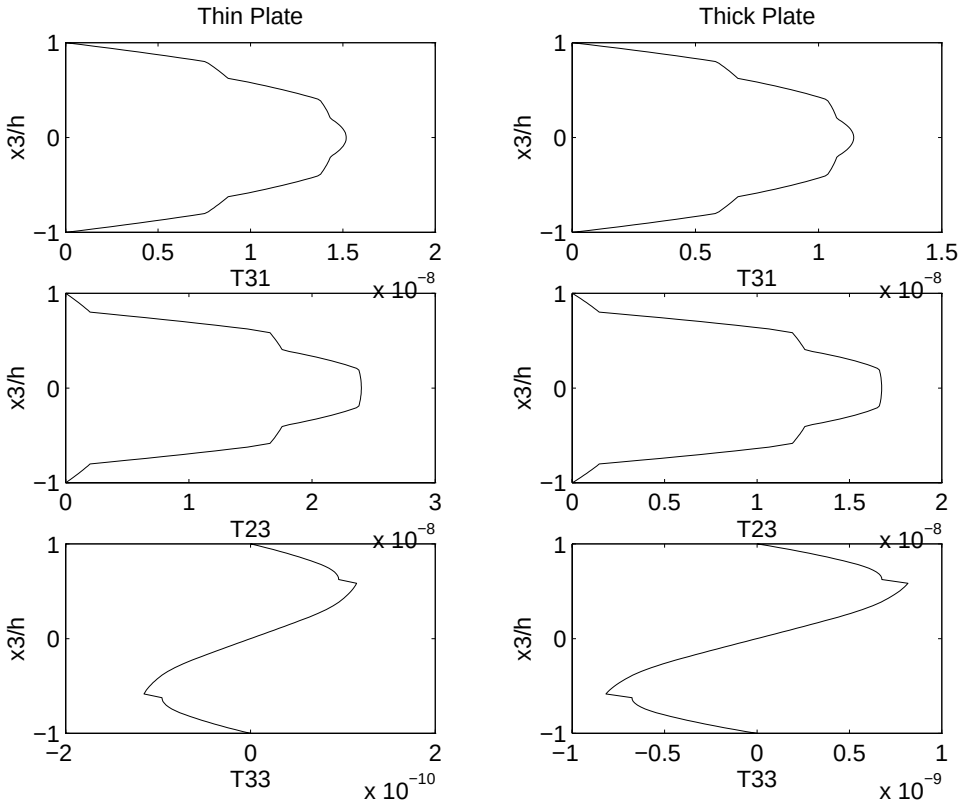

Figure 1.27: Variations through the thickness of the nondimensional out-of-plane stress components at the point $\left(\frac{a}{4}, \frac{b}{4}, .\right)$ for a thin and a thick plate vibrating at a frequency close to Ω_{11}.

Chapter 2

Shape Control of Vibrating Simply Supported Rectangular Plates

Abstract

We determine the optimum location of a given rectangular piezoceramic (PZT) actuator that will require the minimum voltage to annul the deflections of a simply supported rectangular linear elastic plate vibrating near one of its fundamental frequencies. Keeping the location of the centroid and the shape of the PZT fixed, we ascertain the voltage required as a function of the length of its diagonal to nullify the deflections of the plate.

2.1 Introduction

An interesting problem in smart structures is to control the shape of a plate subjected to external disturbances with distributed PZT patches. Here we consider the following problem. Assume that a simply supported rectangular plate with thin piezoelectric layers affixed to its bottom and top surfaces is vibrating freely at a frequency close to one of its natural frequencies. Find the optimum location and size of the PZT region on which a minimum voltage is applied to suppress the motion of the plate. We use the linear theory of elasticity to analyze the vibrations of the simply supported rectangular laminated plate due to the time harmonic driving voltages applied on the surfaces of actuator layers affixed to the bottom and the top of the plate. The solution is then applied to suppress an existing free vibration in the plate. We first envisage that the voltage is to be applied to a square area of fixed sides and investigate the location of its centroid that will require the minimum voltage to diminish the deflection of all points of the plate to essentially zero. Subsequently we locate the centroid

[0]A slightly different version of this chapter has appeared in *AIAA J.*, Vol.34, 1996, pp. 116-122.

of the excited rectangular PZT region at the optimum locations found above, and determine the length of its diagonal with the ratio of its sides always equal to that of the plate that will minimize the voltage. Even though we have not verified it, the conjecture is that if proper voltage at the appropriate frequencies is applied to several areas simultaneously then the deflections of points of the plate can be reduced to essentially zero under a more general loading. For a plate vibrating in first two modes and the PZT excited with the frequency of the first mode, we found that only the first mode was canceled and there was no spill over to the second mode in the sense that its amplitude of vibration remained unchanged. Also, the results presented herein should help others formulate the problem more rigorously by using an optimization theory.

We note that piezoelectric elements have been extensively used to control the vibrations of a beam, e.g., see Baz and Poh[1], Tzou and Tseng[2], and Crawley and de Luis[3]. However, their use to control the shape and vibration of a thin plate has received less attention. Elastic plates with PZT films attached to their surfaces have been analyzed by using approximate two-dimensional plate theories. Three-dimensional equations of elasticity and the method of Fourier series have also been used to study deformations of elastic plates.[4-8] Here we use it to analyze dynamic deformations of a steadily vibrating orthotropic laminated plate with PZT layers bonded to its top and bottom surfaces. The goal is to determine the size of the PZT surface and the voltage to be applied to it so as to annul the deflections of all points of the plate.

2.2 Formulation of the Problem

We use a fixed set of rectangular Cartesian coordinates to describe infinitesimal deformations of a laminated rectangular elastic plate with thin PZT layers affixed to its top and bottom surfaces. Each laminate may be made of an orthotropic material and occupies the domain $0 \le x_1 \le a,\ 0 \le x_2 \le b$ in the $x_1 - x_2$ plane; however in the x_3-direction points in the ith laminate satisfy $h^{(i-1)} \le x_3 \le h^{(i)}$. Thus the positions of the bottom and top surfaces as well as of the $(N-1)$ interfaces are given by $x_3 = 0,\ h^{(1)},\ h^{(2)}, \ldots, h^{(N-1)}, h^{(N)} = h$. We use a superscript i in parentheses to indicate quantities for the ith layer. Equations governing the deformations of a material point of the ith layer are

$$\tau^{(i)}_{\alpha\beta,\beta} = \rho^{(i)} \ddot{u}^{(i)}_{\alpha},\ \alpha, \beta = 1, 2, 3 \tag{2.1}$$

where $\tau_{\alpha\beta}$ is the Cauchy stress tensor, a comma followed by an index β implies partial differentiation with respect to x_β, a repeated index implies summation over the range of the index, ρ is the mass density, $\mathbf{u}$ the displacement and a superimposed dot implies the material time derivative which for infinitesimal deformations reduces to the partial time derivative. The constitutive relation for a linear elastic orthotropic material may be written as

$$\tau_{\alpha\beta} = C_{\alpha\beta\gamma\delta} e_{\gamma\delta}, \tag{2.2}$$

$$2e_{\alpha\beta} = u_{\alpha,\beta} + u_{\beta,\alpha}, \tag{2.3}$$

where $e_{\alpha\beta}$ is infinitesimal strain tensor, $C_{\alpha\beta\gamma\delta}$ is the elasticity tensor and we have dropped the superscript i in parentheses. For an isotropic material

$$C_{\alpha\beta\gamma\nu} = \lambda\delta_{\alpha\beta}\delta_{\gamma\nu} + \mu\left(\delta_{\alpha\gamma}\delta_{\beta\nu} + \delta_{\alpha\nu}\delta_{\beta\gamma}\right) \tag{2.4}$$

where λ and μ are Lamé constants, and $\delta_{\alpha\beta}$ is the Kronecker delta. The boundary conditions at the edges are

$$\begin{aligned} \tau_{11} = 0,\ u_3 = 0,\ u_2 = 0 \text{ at } x_1 = 0, a \\ \tau_{22} = 0,\ u_3 = 0,\ u_1 = 0 \text{ at } x_2 = 0, b. \end{aligned} \tag{2.5}$$

These boundary conditions simulate a simply supported plate characterized by the vanishing of the deflection and bending moment at the edges, and have been previously employed for simply supported plates.[6-8] At the interface $x_3 = h^{(i)}$ between the ith and the $(i+1)$th layers, we have for $i = 1, 2, \ldots, N-1$,

$$\tau_{3\alpha}^{(i)} = \tau_{3\alpha}^{(i+1)},\ u_\alpha^{(i)} = u_\alpha^{(i+1)} \text{ at } x_3 = h^{(i)}\ . \tag{2.6}$$

These imply the continuity of surface tractions and surface displacements at the interface, sometimes also referred to as the coherence conditions. Substitution from (2.2) and (2.3) into (2.1), (2.5) and (2.6) yields the governing equations, boundary conditions and the coherence conditions in terms of displacements.

We model the piezoelectric actuators as thin piezoelectric films, and use superscripts b and t to denote quantities for the bottom and top actuators respectively. For the bottom actuator of thickness h^b poled in the x_3-direction, the pertinent equations are

$$\begin{aligned} h^b(\tau_{11,1}^b + \tau_{21,2}^b) + \tau_{31}^{(1)}\Big|_{x_3=-h} &= \rho^b h^b \ddot{u}_1^b, \\ h^b(\tau_{12,1}^b + \tau_{22,2}^b) + \tau_{32}^{(1)}\Big|_{x_3=-h} &= \rho^b h^b \ddot{u}_2^b, \\ \tau_{11}^b = c_{11}^b u_{1,1}^b + c_{12}^b u_{2,2}^b - e_{31}^b V^b(x_1, x_2, t)/h^b, \\ \tau_{22}^b = c_{12}^b u_{1,1}^b + c_{11}^b u_{2,2}^b - e_{31}^b V^b(x_1, x_2, t)/h^b, \\ \tau_{12}^b = c_{66}^b\left(u_{1,2}^b + u_{2,1}^b\right), \\ \tau_{11}^b = 0,\ u_2^b = 0 \text{ at } x_1 = 0, a, \\ \tau_{22}^b = 0,\ u_1^b = 0 \text{ at } x_2 = 0, b, \\ \tau_{33}^{(1)} = \rho^b h^b \ddot{u}_3^{(1)},\ u_1^{(1)} = u_1^b,\ u_2^{(1)} = u_2^b \text{ at } x_3 = -h. \end{aligned} \tag{2.7}$$

Equations $(2.7)_{1\text{-}2}$ express the balance of linear momentum obtained after integrating through the thickness and assuming that displacements of the PZT layer are independent of x_3. The

constitutive relations of the PZT are given by equations $(2.7)_{3\text{-}5}$ with V^b being the voltage difference across its surfaces, and boundary conditions $(2.7)_{6\text{-}7}$ are equivalent to the vanishing of moments and displacements at the edges. The coherency or continuity conditions at the interface $x_3 = -h$ are given by equation $(2.7)_8$.

We note that equations analogous to (2.7) give deformations of the top PZT layer and are omitted.

2.3 Time Harmonic Vibration

2.3.1 Reduction of Governing Equations

We assume that the plate is vibrating harmonically at a frequency close to one of its natural frequencies with no voltage applied to the PZTs. Let the corresponding displacement field be given by $\tilde{u}^0_\alpha(x_1, x_2, x_3)$. The objective is to find the optimum size and location of the rectangular area on the top and bottom PZT layers where a harmonically varying voltage with frequency equal to that of the plate and the least amplitude should be applied so as to annul the deflections of all points of the plate. Since we are analyzing a linear problem, the resulting displacement of a point equals the sum of the initial displacement and that induced by the applied voltage. Below we attempt to find the latter.

Let the time harmonic driving voltage be given by

$$\begin{aligned} V^b(x_1, x_2, t) &= \tilde{V}^b(x_1, x_2)e^{i\omega t} \\ V^t(x_1, x_2, t) &= \tilde{V}^t(x_1, x_2)e^{i\omega t} \end{aligned} \tag{2.8}$$

For steady state vibrations all field quantities have the same time dependence

$$\begin{aligned} u^{(i)}_\alpha(x_1, x_2, x_3, t) &= \tilde{u}^{(i)}_\alpha(x_1, x_2, x_3)e^{i\omega t},\ \alpha = 1, 2, 3, \\ u^t_\alpha(x_1, x_2, t) &= \tilde{u}^t_\alpha(x_1, x_2)e^{i\omega t},\ \alpha = 1, 2, \\ u^b_\alpha(x_1, x_2, t) &= \tilde{u}^b_\alpha(x_1, x_2)e^{i\omega t},\ \alpha = 1, 2. \end{aligned} \tag{2.9}$$

Substitution of equations (2.9) and constitutive relations (2.2) and $(2.7)_{3\text{-}5}$ into equations (2.1), $(2.7)_{1\text{-}2}$, (2,6) and $(2.7)_{6\text{-}8}$ yields following equations for the determination of $\tilde{u}^{(i)}_\alpha$, $\tilde{u}^t_\alpha$

and $\tilde{u}^b_\alpha$, where we have dropped the superimposed tildes on $\mathbf{u}$.

$$
\begin{aligned}
&c^{(i)}_{11}u^{(i)}_{1,11} + c^{(i)}_{66}u^{(i)}_{1,22} + c^{(i)}_{55}u^{(i)}_{1,33} + (c^{(i)}_{12} + c^{(i)}_{66})u^{(i)}_{2,12} + (c^{(i)}_{13} + c^{(i)}_{55})u^{(i)}_{3,13} = -\rho^{(i)}\omega^2 u^{(i)}_1 \\
&(c^{(i)}_{12} + c^{(i)}_{66})u^{(i)}_{1,12} + c^{(i)}_{66}u^{(i)}_{2,11} + c^{(i)}_{22}u^{(i)}_{2,22} + c^{(i)}_{44}u^{(i)}_{2,33} + (c^{(i)}_{23} + c^{(i)}_{44})u^{(i)}_{3,23} = -\rho^{(i)}\omega^2 u^{(i)}_2 \\
&(c^{(i)}_{13} + c^{(i)}_{55})u^{(i)}_{1,13} + (c^{(i)}_{23} + c^{(i)}_{44})u^{(i)}_{2,23} + c^{(i)}_{55}u^{(i)}_{3,11} + c^{(i)}_{44}u^{(i)}_{3,22} + c^{(i)}_{33}u^{(i)}_{3,33} = -\rho^{(i)}\omega^2 u^{(i)}_3 \\
&c^{(i)}_{11}u^{(i)}_{1,1} + c^{(i)}_{12}u^{(i)}_{2,2} + c^{(i)}_{13}u^{(i)}_{3,3} = 0\ , \quad u^{(i)}_3 = 0\ , \quad u^{(i)}_2 = 0 \quad \text{at} \quad x_1 = 0,\ a \\
&c^{(i)}_{12}u^{(i)}_{1,1} + c^{(i)}_{22}u^{(i)}_{2,2} + c^{(i)}_{23}u^{(i)}_{3,3} = 0\ , \quad u^{(i)}_3 = 0\ , \quad u^{(i)}_1 = 0 \quad \text{at} \quad x_2 = 0,\ b
\end{aligned}
\tag{2.10}
$$

$$
\begin{aligned}
&c^{(i)}_{55}(u^{(i)}_{3,1} + u^{(i)}_{1,3}) = c^{(i+1)}_{55}(u^{(i+1)}_{3,1} + u^{(i+1)}_{1,3}) \quad \text{at} \quad x_3 = h^{(i)} \\
&c^{(i)}_{44}(u^{(i)}_{2,3} + u^{(i)}_{3,2}) = c^{(i+1)}_{44}(u^{(i+1)}_{2,3} + u^{(i+1)}_{3,2}) \quad \text{at} \quad x_3 = h^{(i)} \\
&c^{(i)}_{13}u^{(i)}_{1,1} + c^{(i)}_{23}u^{(i)}_{2,2} + c^{(i)}_{33}u^{(i)}_{3,3} = c^{(i+1)}_{13}u^{(i+1)}_{1,1} + c^{(i+1)}_{23}u^{(i+1)}_{2,2} + c^{(i+1)}_{33}u^{(i+1)}_{3,3} \quad \text{at} \quad x_3 = h^{(i)} \\
&u^{(i)}_1 = u^{(i+1)}_1\ , \quad u^{(i)}_2 = u^{(i+1)}_2\ , \quad u^{(i)}_3 = u^{(i+1)}_3 \quad \text{at} \quad x_3 = h^{(i)}
\end{aligned}
\tag{2.11}
$$

$$
\begin{aligned}
&h^b\bar{c}^b_{11}u^b_{1,11} + h^b c^b_{66}u^b_{1,22} + h^b(\bar{c}^b_{12} + c^b_{66})u^b_{2,12} + c^{(1)}_{55}(u^{(1)}_{3,1} + u^{(1)}_{1,3})\Big|_{x_3=-h} = -\rho^b h^b\omega^2 u^b_1 \\
&h^b(\bar{c}^b_{12} + c^b_{66})u^b_{1,12} + h^b c^b_{66}u^b_{2,11} + h^b\bar{c}^b_{11}u^b_{2,22} + c^{(1)}_{44}(u^{(1)}_{3,2} + u^{(1)}_{2,3})\Big|_{x_3=-h} = -\rho^b h^b\omega^2 u^b_2 \\
&h^b\bar{c}^b_{11}u^b_{1,1} = \bar{e}^b_{31}\bar{V}^b\ , \quad u^b_2 = 0 \quad \text{at} \quad x_1 = 0,\ a \\
&h^b\bar{c}^b_{11}u^b_{2,2} = \bar{e}^b_{31}\bar{V}^b\ , \quad u^b_1 = 0 \quad \text{at} \quad x_2 = 0,\ b
\end{aligned}
\tag{2.12}
$$

$$
\begin{aligned}
&h^t\bar{c}^t_{11}u^t_{1,11} + h^t c^t_{66}u^t_{1,22} + h^t(\bar{c}^t_{12} + c^t_{66})u^t_{2,12} - c^{(N)}_{55}(u^{(N)}_{3,1} + u^{(N)}_{1,3})\Big|_{x_3=h} = -\rho^t h^t\omega^2 u^t_1 \\
&h^t(\bar{c}^t_{12} + c^t_{66})u^t_{1,12} + h^t c^t_{66}u^t_{2,11} + h^t\bar{c}^t_{11}u^t_{2,22} - c^{(N)}_{44}(u^{(N)}_{3,2} + u^{(N)}_{2,3})\Big|_{x_3=h} = -\rho^t h^t\omega^2 u^t_2 \\
&h^t\bar{c}^t_{11}u^t_{1,1} = \bar{e}^t_{31}\bar{V}^t\ , \quad u^t_2 = 0 \quad \text{at} \quad x_1 = 0,\ a \\
&h^t\bar{c}^t_{11}u^t_{2,2} = \bar{e}^t_{31}\bar{V}^t\ , \quad u^t_1 = 0 \quad \text{at} \quad x_2 = 0,\ b
\end{aligned}
\tag{2.13}
$$

$$
\begin{aligned}
&c^{(1)}_{13}u^{(1)}_{1,1} + c^{(1)}_{23}u^{(1)}_{2,2} + c^{(1)}_{33}u^{(1)}_{3,3} = -\rho^b h^b\omega^2 u^{(1)}_3, \quad u^{(1)}_1 = u^b_1, \quad u^{(1)}_2 = u^b_2 \text{ at } x_3 = -h \\
&-(c^{(N)}_{13}u^{(N)}_{1,1} + c^{(N)}_{23}u^{(N)}_{2,2} + c^{(N)}_{33}u^{(N)}_{3,3}) = -\rho^t h^t\omega^2 u^{(N)}_3, \quad u^{(N)}_1 = u^t_1, \quad u^{(N)}_2 = u^t_2 \text{ at } x_3 = h
\end{aligned}
\tag{2.14}
$$

2.3.2 Solutions for the Laminates

The solution procedure is similar to that detailed in Ref. 8 and is therefore briefly described herein. In order to solve equations (2.10) we assume that

$$u_1(x_1,x_2,x_3,t) = \sum_{m,n=1}^{\infty} a_{1mn}(x_3)\cos\alpha_m x_1 \sin\beta_n x_2,$$
$$u_2(x_1,x_2,x_3,t) = \sum_{m,n=1}^{\infty} a_{2mn}(x_3)\sin\alpha_m x_1 \cos\beta_n x_2,$$
$$u_3(x_1,x_2,x_3,t) = \sum_{m,n=1}^{\infty} a_{3mn}(x_3)\sin\alpha_m x_1 \sin\beta_n x_2,$$
$$\alpha_m = m\pi/a,\ \beta_n = n\pi/b, \tag{2.15}$$

which satisfy all boundary conditions at the edges $x_1 = 0, a$ and $x_2 = 0, b$. Substitution of equations (2.15) into the governing equations (2.10) yields following ordinary differential equations for $a_{\alpha mn}(x_3)$

$$\begin{gathered}
-c_{11}^{(i)}\alpha_m^2 a_{mn}^{(i)} - c_{66}^{(i)}\beta_n^2 a_{mn}^{(i)} + c_{55}^{(i)} a_{mn,33}^{(i)} - (c_{12}^{(i)} + c_{66}^{(i)})\alpha_m\beta_n b_{mn}^{(i)} \\
+(c_{13}^{(i)} + c_{55}^{(i)})\alpha_m c_{mn,3}^{(i)} = -\rho^{(i)}\omega^2 a_{mn}^{(i)} \\
-(c_{12}^{(i)} + c_{66}^{(i)})\alpha_m\beta_n a_{mn}^{(i)} - c_{66}^{(i)}\alpha_m^2 b_{mn}^{(i)} - c_{22}^{(i)}\beta_n^2 b_{mn}^{(i)} + c_{44}^{(i)} b_{mn,33}^{(i)} \\
+(c_{23}^{(i)} + c_{44}^{(i)})\beta_n c_{mn,3}^{(i)} = -\rho^{(i)}\omega^2 b_{mn}^{(i)} \\
-(c_{13}^{(i)} + c_{55}^{(i)})\alpha_m a_{mn,3}^{(i)} - (c_{23}^{(i)} + c_{44}^{(i)})\beta_n b_{mn,3}^{(i)} - c_{55}^{(i)}\alpha_m^2 c_{mn}^{(i)} \\
-c_{44}^{(i)}\beta_n^2 c_{mn}^{(i)} + c_{33}^{(i)} c_{mn,33}^{(i)} = -\rho^{(i)}\omega^2 c_{mn}^{(i)}
\end{gathered} \tag{2.16}$$

We now assume that

$$a_{\alpha mn}(x_3) = A_{\alpha mn} e^{\eta_{mn} x_3},\ \text{no sum on repeated indices}, \tag{2.17}$$

where $A_{\alpha mn}$ are undetermined constants. Relation (2.17) when substituted into equation (2.16) yields a set of linear homogeneous equations for the determination of $A_{\alpha mn}$; the coefficients of these equations involve the elastic constants for the material of the laminate. The necessary and sufficient condition for these equations to have a nontrivial solution is the following cubic equation for η_{mn}.

$$(\eta_{mn})^6 + a(\eta_{mn})^4 + b(\eta_{mn})^2 + c = 0 \tag{2.18}$$

Explicit expressions for a, b and c in terms of the elasticities of the laminate are given in Ref. 8. For a real root η_{mnp} with $p = 1, 2, \ldots, 6$, of equation (2.18), we have

$$a_{\alpha mn}(x_3) = D_{mnp} F_{\alpha mnp} e^{\eta_{mnp} x_3},\ \text{no sum on } m,\ n,\ \text{but summed on } p \tag{2.19}$$

where D_{mnp} is an arbitrary constant and $F_{\alpha mnp}$ is a function of η_{mnp} and the material parameters. For a complex root $\eta_{mnp} = \xi_{mnp} + i\zeta_{mnp}$ of equation (2.18), one can show that equation (2.19) still holds with $F_{\alpha mnp}$ involving $\cos(\xi_{mnp}x_3)$ and $\sin(\zeta_{mnp}x_3)$ in addition to the material elasticities. We note that for a few values of ω, equation (2.18) may have repeated roots; it is more likely to occur for an isotropic material. We exclude those special values of ω.

The continuity conditions at the interface $x_3 = h^{(i)}$ require that

$$\left[D^{(i)}_{mnp}\right] = \left[T^{(i)}\right]\left[D^{(i+1)}_{mnp}\right] \tag{2.20}$$

where $\left[D^{(i)}_{mnp}\right]$ is a 6×1 matrix (for $p = 1, 2, \ldots, 6$) and $[T^{(i)}]$ is a 6×6 matrix whose elements are functions of $F^{(i)}_{\alpha mnp}$ and $F^{(i+1)}_{\alpha mnp}$ evaluated at $x_3 = h^{(i)}$. Equation (2.20) is a recursive relation between constants for the ith and $(i+1)$th laminate.

2.3.3 Solutions for the Actuators

We assume that

$$\begin{aligned} u^b_1(x_1, x_2) &= \sum_{m,n=1}^{\infty} D^b_{1mn} \cos\alpha_m x_1 \sin\beta_n x_2, \\ u^b_2(x_1, x_2) &= \sum_{m,n=1}^{\infty} D^b_{2mn} \sin\alpha_m x_1 \cos\beta_n x_2, \end{aligned} \tag{2.21}$$

give the displacement field for the bottom actuator. In order to avoid term by term differentiation and to take care of the nonhomogeneous boundary conditions at the same time, we multiply equations obtained from equation $(2.7)_1$ by $\cos\alpha_m x_1 \sin\beta_n x_2$ and that obtained from equation $(2.7)_2$ by $\sin\alpha_m x_1 \cos\beta_n x_2$, and integrate the resulting equations over $0 < x_1 < a$ and $0 < x_2 < b$. With integration by parts and the use of boundary conditions $(2.7)_{6\text{-}7}$, we arrive at the following.

$$\begin{aligned} &\sum_{p=1}^{6} R^{(1)}_{mnp}(-h)D^{(1)}_{mnp} + h^b(\rho^b\omega^2 - c^b_{11}\alpha^2_m - c^b_{66}\beta^2_n)D^b_{1mn} \\ -h^b(c^b_{12} + c^b_{66})\alpha_m\beta_n D^b_{2mn} &= \frac{4e^b_{31}}{ab}\alpha_m \int_0^a \int_0^b V^b \sin\alpha_m x_1 \sin\beta_n x_2 dx_1 dx_2, \\ &\sum_{p=1}^{6} Q^{(1)}_{mnp}(-h)D^{(1)}_{mnp} - h^b(c^b_{12} + c^b_{66})\alpha_m\beta_n D^b_{1mn} \\ +h^b(\rho^b\omega^2 - c^b_{66}\alpha^2_m - c^b_{11}\beta^2_n)D^b_{2mn} &= \frac{4e^b_{31}}{ab}\beta_n \int_0^a \int_0^b V^b \sin\alpha_m x_1 \sin\beta_n x_2 dx_1 dx_2, \end{aligned} \tag{2.22}$$

where R_{mnp} and Q_{mnp} are linear functions of $F_{\alpha mnp}$ and $F_{\alpha mnp,3}$, and V^b is a function of x_1 and x_2. The continuity conditions $(2.7)_8$ at the interface between the plate and the bottom actuator give additional conditions on D_{mnp}, D^b_{1mn} and D^b_{2mn}; similar equations can be obtained for the top actuator. The end result is that we get a set of sixteen algebraic equations for the sixteen unknowns $D^{(1)}_{mnp}$, $D^{(N)}_{mnp}$, D^b_{1mn}, D^b_{2mn}, D^t_{1mn} and D^t_{2mn}. Knowing ω and V, we can solve for these sixteen unknowns and hence for displacements and stresses at any point of the structure.

2.4 Numerical Results

In order to elucidate that the deflections of a vibrating plate can be controlled by applying suitable voltage to a part of the top and bottom PZT layers, we consider a graphite-epoxy plate with PZT-G1195 actuators affixed to its top and bottom surfaces. The material parameters for the graphite-epoxy are

$$E_{11} = 150 \text{ GPa},\ E_{22} = E_{33} = 9 \text{ GPa},\ \nu_{12} = \nu_{23} = \nu_{31} = 0.3,$$
$$G_{12} = G_{31} = 7.1 \text{ GPa},\ G_{23} = 2.5 \text{ GPa},\ \rho = 1600 \text{ kg/m}^3, \tag{2.23}$$

and those for the PZT-G1195 are

$$\rho = 7500 \text{ kg/m}^3,\ [e] = \begin{bmatrix} 0 & 0 & -2.1 \\ 0 & 0 & -2.1 \\ 0 & 0 & 9.5 \\ 0 & 9.2 & 0 \\ 9.2 & 0 & 0 \\ 0 & 0 & 0 \end{bmatrix}^T C/m^2;$$

$$[c] = \begin{bmatrix} 148 & 76.2 & 74.2 & 0 & 0 & 0 \\ & 148 & 74.2 & 0 & 0 & 0 \\ & & 131 & 0 & 0 & 0 \\ & & & 25.4 & 0 & 0 \\ & & & & 25.4 & 0 \\ & & & & & 25.4 \end{bmatrix} GPa \tag{2.24}$$

For geometric dimensions, we choose $a = 40$ cm, $b = 30$ cm, $h = 1$ mm, $h^b = h^t = 0.1$ mm. Even though the analysis presented above is valid for a laminated elastic plate, results presented herein are for one lamina. We apply a uniform voltage to a rectangular region of the PZT surface and zero voltage to the rest of the PZT surface.

The structure has a series of natural bending vibration frequencies which can be ordered as ω_{mn}, $m, n = 1, 2, 3, \ldots$. The free bending vibration modes corresponding to ω_{11}, ω_{31}, $\omega_{13}, \omega_{33}, \ldots$ are symmetric about both $x_1 = a/2$ and $x_2 = b/2$, and those corresponding to

$\omega_{12}, \omega_{21}, \omega_{22}, \ldots$ are antisymmetric about either $x_1 = a/2$ or $x_2 = b/2$, or both. The natural frequencies of the structure can be roughly estimated from the results of the plate theory. When the inertia and rigidity of the actuators are neglected, we have (Jones[9])

$$\Omega_{mn} \equiv \frac{\omega_{mn}}{\left(\frac{\pi^2}{a^2}\left(\frac{D_{11}}{2\rho h}\right)^{1/2}\right)} = \left[m^4 + 2\frac{D_{12}+2D_{66}}{D_{11}}m^2\left(\frac{a}{b}n\right)^2 + \frac{D_{22}}{D_{11}}\left(\frac{a}{b}n\right)^4\right]^{1/2} \tag{2.25}$$

where $D_{\alpha\beta}$ $(\alpha, \beta = 1, 2, 6)$ is the flexural rigidity and Ω_{mn} is the normalized natural frequency. Values of Ω_{mn} computed from (2.25) are compared in Table 2.1 with those obtained from the present method for the two cases when the PZTs are considered and when their effect is made negligible by assigning very small values to their thicknesses and the mass density. Values of Ω_{mn} by the present method are obtained by plotting $|U_3(a/4, b/4, 0)| = |u_3(a/4, b/4, 0)|hc^p_{31}h^b/a^2e^b_{31}V^b$, the normalized deflection at the diagonal of the plate, as a function of the normalized forcing fequency $\Omega = \omega/\frac{\pi^2}{a^2}\left(\frac{D_{11}}{\rho 2h}\right)^{1/2}$ in Fig. 2.2. It is seen that $U_3(a/4, b/4, 0)$ becomes large at certain discrete values of Ω, which signifies the resonance phenomenon. Those values of Ω at which resonances occur should be in the sequence of Ω_{11}, Ω_{12}, Ω_{21}, Ω_{13}, Ω_{22}, Ω_{23}, Ω_{31}, Ω_{32}, $\Omega_{33}\ldots$. It is evident from the values listed in the Table 2.1 that the presently computed values of Ω_{mn} are close to those obtained from the plate theory; it is to be expected since the plate theory gives good results for low frequency vibrations. However, the present method will compute high frequencies accurately too. Also, the frequencies are shifted noticeably when thin layers of PZTs are affixed to the top and bottom surfaces of the plate. From Table 2.1 we find that the natural frequencies of the plate increase when PZT layers are affixed to it except for modes 21 and 31 in which case the natural frequencies decrease. In order to verify these results, we computed frequencies of the Graphite-Epoxy/PZT composite plate by the classical laminated plate theory. Since the PZTs is a transversely isotropic material which is a special case of an orthotropic material, it is appropriate to calculate the natural frequencies of the composite plate with equation (2.25). Table 2.2 lists the natural frequencies obtained by the plate theory for the plate with and without PZT layers. It can be seen by comparing Table 2.1 and 2.2 that both the classical plate theory and the present 3-D elasticity theory predict similar trends for natural frequencies of a thin composite plate. However, the present 3-D theory will also give accurate results for thick plates.

When Ω is near Ω_{11}, Ω_{12}, Ω_{13} etc., at most 20 terms of the Fourier series in equations (2.15) are needed for $u_3\left(\frac{a}{2}, \frac{b}{2}, 0\right)$ to be computed accurately to four significant digits. For higher values of Ω, higher order modes also become important, and therefore more terms are needed in the series. For results presented herein, eight hundred terms in the Fourier series are summed to ensure sufficient accuracy.

We now assume that the structure is vibrating at a frequency close to one of its natural

frequencies with the displacement field given by

$$u_3^0 = 0.3 \sin \frac{m\pi x_1}{a} \sin \frac{n\pi x_2}{b} e^{i\Omega_{mn}t} \; mm$$
$$u_1^0 = u_2^0 = 0 \; . \tag{2.26}$$

We apply a voltage $\pm V_0 e^{i\Omega_{mn}t}$ to a square region of the top and bottom PZTs with zero voltage applied to the rest of the PZT surfaces. The reason for selecting a square region is to evaluate exactly the integrals in equations (2.22). We first keep the size of the square region to which nonzero voltage is applied fixed and for a given location (x_1, x_2) of its centroid, find the voltage to be applied to the square region that will reduce the magnitude of vertical deflections of all points of the plate to less than one-hundreth of the amplitude of their initial vibrations. Then with the centroid of the region located at the point which requires the least voltage in the preceding exercise, we vary the length of the sides of the rectangular region but keeping the ratio of their lengths as a/b, and find the applied voltage which will effectively annul the deflections of all points of the plate.

Figures 2.3 through 2.6 depict the voltage required to annul the deflections of the plate as a function of the coordinates of the centroid of the 6 cm × 6 cm region for modes 11, 13, 21 and 22 respectively; the normalized frequencies of the applied voltage and the structure equal 1.46, 7.35, 4.06, 5.79 respectively. It is clear that the needed voltage is minimum (maximum) when the centroid of the square region is located at points where $|u_3^0|$ assumes maximum (zero) values. Thus the most effective location of the square PZT region is points where the amplitude of initial vibrations of the plate is maximum. Whereas for mode 11, there is one optimum location i.e. $\left(\frac{a}{2}, \frac{b}{2}\right)$ of the centroid of the excited square PZT region; for mode 13 there are three equally good locations viz $\left(\frac{a}{2}, \frac{b}{2}\right)$, $\left(\frac{a}{2}, \frac{b}{6}\right)$, $\left(\frac{a}{2}, \frac{5b}{6}\right)$; for mode 12 equally effective locations are $\left(\frac{a}{4}, \frac{b}{2}\right)$, $\left(\frac{3a}{4}, \frac{b}{2}\right)$; and for mode 22 four locations that require minimum value of V_0 are $\left(\frac{a}{4}, \frac{b}{4}\right)$, $\left(\frac{a}{4}, \frac{3b}{4}\right)$, $\left(\frac{3a}{4}, \frac{b}{4}\right)$ and $\left(\frac{3a}{4}, \frac{3b}{4}\right)$. We note that the sign of the voltage of the top and bottom PZT layers may have to be switched if all of the excited region crosses a nodal line. Figures 2.7 through 2.10 depict the variation of the voltage required as a function of the length of the diagonal of the rectangular region on which a voltage is applied. These plots illustrate that the voltage required to suppress the deflections of points of the plate decreases rapidly as the size of the excited region is increased provided that this region is away from the nodal lines. However, when the excited region approaches nodal lines, the voltage required to suppress the vibrations decreases rather slowly. The magnitude of the slope of these curves gradually approaches zero so that a point of diminishing return is reached when the boundaries of the excited region abut but do not cross the nodal lines. For mode 13, the required voltage suddenly increases when the excited PZT region extends over plate particles vibrating in opposite directions or crosses over the nodal line. Figures 2.11 through 2.14 depict the deflected shape of the diagonal of the plate both when similarly situated optimum rectangular regions of the top and bottom PZT layers with centroids at the optimum location are and are not activated; the voltage applied equals 159.8V, 44.8V, 103.4V, and 57.6V respectively for modes 11,13,21 and 22. It is clear that the deflections

of points of a diagonal of the plate for each one of the four modes considered have been annulled.

We have plotted in Fig. 2.15 the distribution of the non-dimensional shear stress, $T_{31}(x_1, x_2, h) = \tau_{31}(x_1, x_2, h)h^b/e_{31}^b V^b$, at the interface between the plate and the top PZT for the structure vibrating at a normalized frequency of 1.46 which is close to Ω_{11}. It is clear that the shear stress is high at the edges of the excited square region; for other modes of vibration, the shear stress is found to be high either at the other two edges of the excited square region and/or at the four corners. The high value of the shear stress at a point may result in delamination of the PZT layer there. The high value of the shear stress at a corner may be eliminated or reduced considerably by exciting a circular region of the PZT layer, but it could not be verified because of the difficulty in evaluating exactly the integrals in equations (2.22). The numerical evaluation of these integrals results in high values of T_{31} at the quadrature points used to evaluate these integrals.

Computed values of stress components T_{11}, T_{22} and T_{12} within the top PZT indicated that T_{11} assumed maximum values at points near the boundaries of the activated region. The maximum value of T_{11}/c_{11}^b equalled 1.9×10^{-5}; the maximum values of other stress components were nearly an order of magnitude lower than that of T_{11}. Thus stresses induced in the top PZT are considerably below the yield stress of the material and its deformations are infinitesimal.

As is clear from the results presented in Table 2.1, the PZTs alter the natural frequencies of the structure; in some cases this may be advantageously used to shift the natural frequency of the structure away from the frequency of the external disturbance. Our analysis technique does not extend to the case when PZT patches that do not cover the entire plate surface are used.

2.5 Conclusions

We have analysed steady state vibrations of a simply supported rectangular plate with PZT actuators bonded to its top and bottom surfaces. Three-dimensional equations of linear elasticity with mixed boundary conditions at the plate edges are solved by the method of Fourier series. It is assumed that PZTs can be modeled as thin layers, and are perfectly bonded to the plate surfaces. The location and size of the optimum regions of the PZTs that should be excited with the minimum voltage in order to control the deflections of all points of the plate have been determined for four modes of vibration. In order for the voltage required to suppress the vibrations of all points be minimum, the centroid of the excited PZT region should be located at points where the amplitude of initial vibrations of the simply supported plate is maximum. The method of Fourier series is difficult to apply to a plate

with a clamped edge because of the difficulty in choosing expressions like those given by equations (2.9) for displacements that will satisfy boundary conditions identically.

2.6 References

1. Baz, A., and Poh, S., "Performance of an Active Control System with Piezoelectric Actuators," *Journal of Sound and Vibration*, Vol. 126, 1988, pp. 327-343.

2. Tzou, H.S., and Tseng, C.I., "Distributed Modal Identification and Vibration Control of Continua: Piezoelectric Finite Element Formulation and Analysis," *Journal of Dynamic Systems, Measurement and Control*, Vol. 113, 1991, pp. 501-505.

3. Crawley, E.F. and de Luis, J., "Use of Piezoelectric Actuators as Elements of Intelligent Structures," *AIAA Journal*, Vol. 25, 1987, pp. 1373-1385.

4. Srinivas S., Rao, C.V.J. and Rao, A.K., "An Exact Analysis of Vibration of Simply-Supported Homogeneous and Laminated Thick Rectangular Plates," *J. Sound Vib.*, Vol. 12, 1970, pp. 257-269.

5. Wittrick, W.H., "Analytical, Three-dimensional Elasticity Solutions to Some Plate Problems, and some Observations on Mindlin's Plate Theory," *Int. J. Solids Structures*, Vol. 23, 1987, pp. 441-464.

6. Zhou, Y.S., and Tiersten, H.F., "Elastic Analysis of Laminated Composite Plates in Cylindrical Bending due to Piezoelectric Actuators," *Smart Materials & Structure*, Vol. 3, 1994, 255-265.

7. Yang, J.S., Batra, R.C. and Liang, X.Q., "The Cylindrical Bending Vibration of a Laminated Elastic Plate Due to Piezoelectric Actuators," *Smart Materials & Structures*, Vol. 3, 1994, 485-493.

8. Batra, R.C., Liang, X.Q., and Yang, J.S., The Vibration of a Simply Supported Rectangular Elastic Plate due to Piezoelectric Actuators", *International J. Solids & Structures* Vol.33, No.11, 1996, pp.1597-1618.

9. Jones, R.M., *Mechanics of Composite Materials*, Scripta Book Co., Washington, D.C., 1975.

Table 2.1 Values of resonant frequencies Ω_{mn} for the graphite/epoxy plate as computed by the plate theory and the present method, and also by the present method for the plate with PZTs bonded to the top and bottom surfaces.
1- Plate theory
2- Present method; the plate with no PZTs
3- Present method; the plate with PZTs.

	m=1	m=2	m=3	Case
n=1	1.260	4.217	9.208	1
	1.260	4.170	9.170	2
	1.455	4.065	8.550	3
n=2	2.373	5.041	9.919	1
	2.330	5.040	9.880	2
	3.585	5.790	10.035	3
n=3	4.466	6.761	11.343	1
	4.460	6.710	11.290	2
	7.350	9.225	13.005	3

Table 2.2 Values of natural frequencies Ω_{mn} (rad/sec) for the graphite/epoxy plate with and without PZT layers as computed by the plate theory.
1- Plate without PZT layers
2- plate with PZT layers

	m=1	m=2	m=3	Case
n=1	435.78	1458.16	3183.65	1
	524.76	1442.10	3016.62	2
n=2	820.36	1743.10	3429.71	1
	1305.27	2099.04	3594.85	2
n=3	1544.34	2337.85	3921.98	1
	2663.67	3360.65	4722.84	2

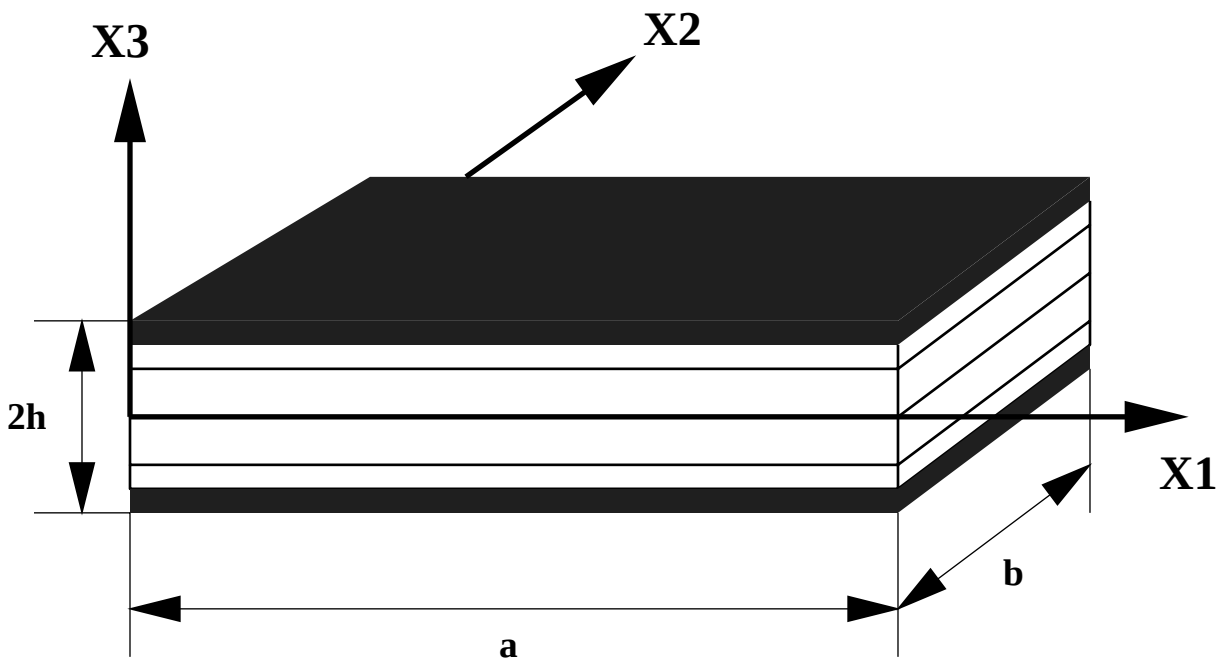

Figure 2.1: A schematic sketch of the problem studied

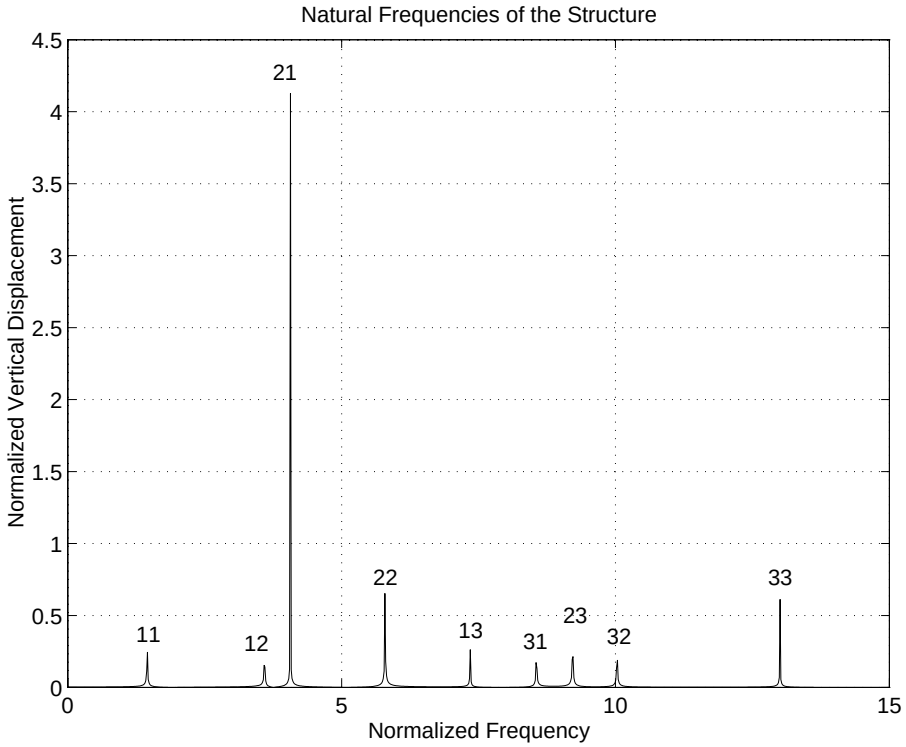

Figure 2.2: The normalized deflection, $|U_3(a/4, b/4, 0)| = |u_3(a/4, b/4, 0)|hc_{31}^p h^b/a^2 e_{31}^b V$, as a function of the nondimensional forcing frequency $\Omega = \omega/\frac{\pi^2}{a^2}\left(\frac{D_{11}}{2\rho h}\right)^{1/2}$.

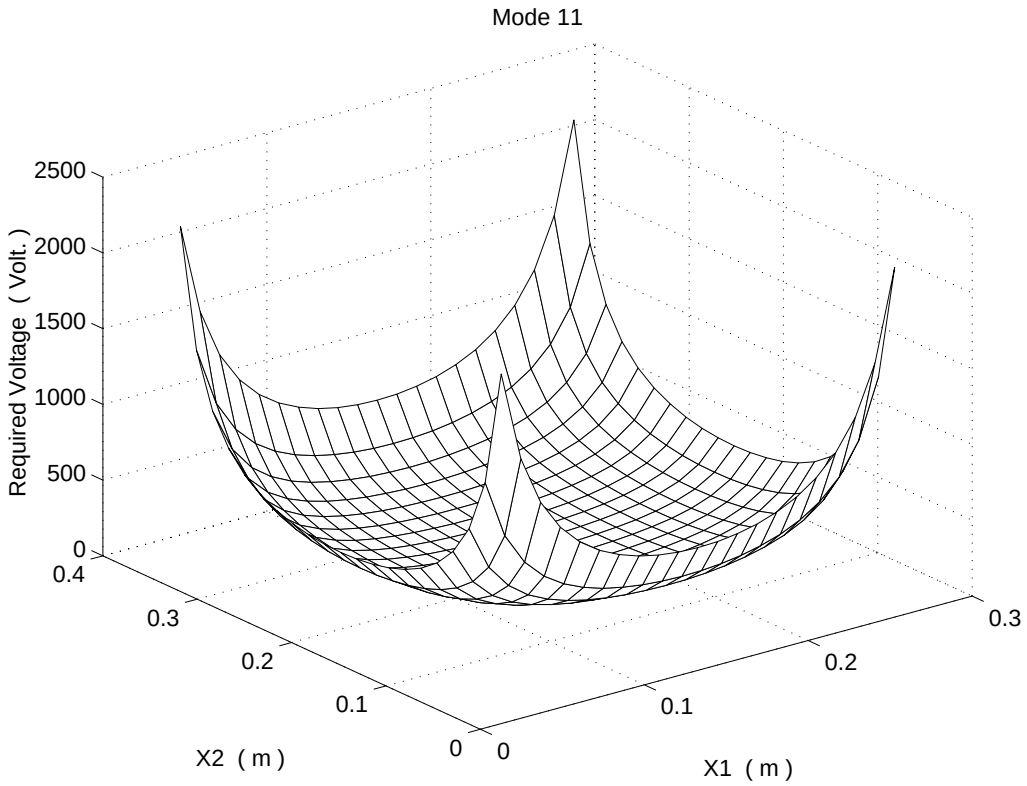

Figure 2.3: Voltage required to suppress the deflections of points on the plate diagonal as a function of the location of the centroid of the 6 cm $\times$ 6 cm PZT region that is excited. The plate is vibrating steadily at a frequency close to Ω_{11}.

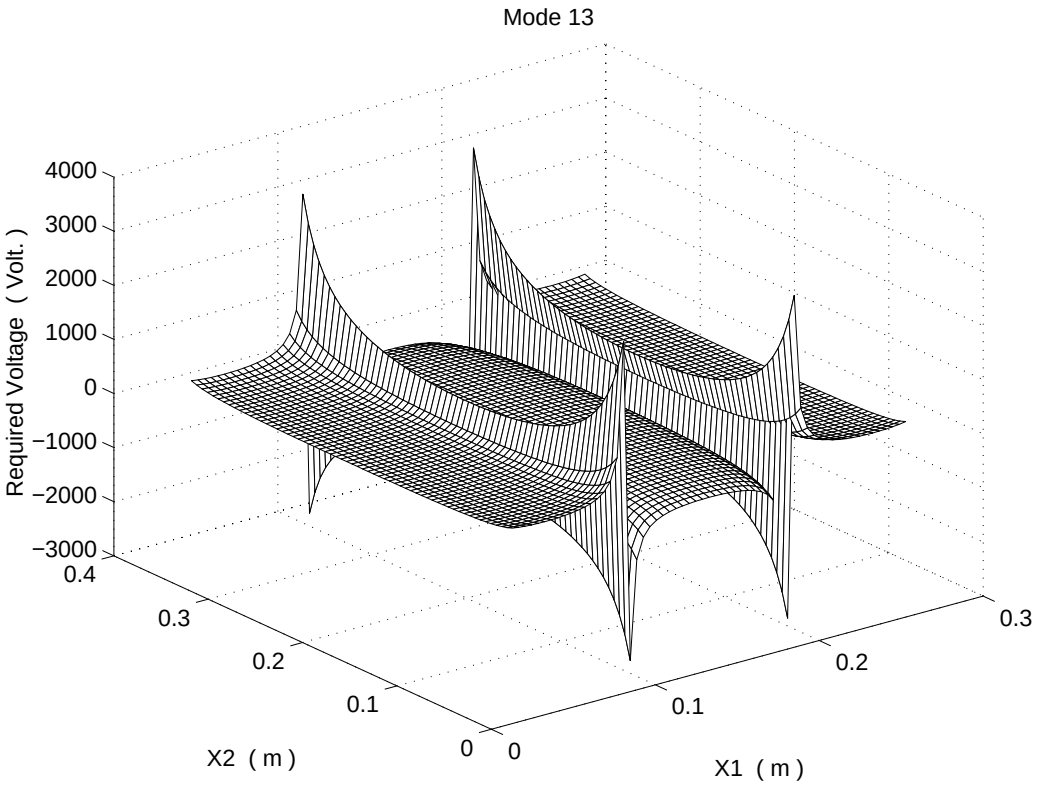

Figure 2.4: Voltage required to suppress the deflections of points on the plate diagonal as a function of the location of the centroid of the 6 cm $\times$ 6 cm PZT region that is excited. The plate is vibrating steadily at a frequency close to Ω_{13}.

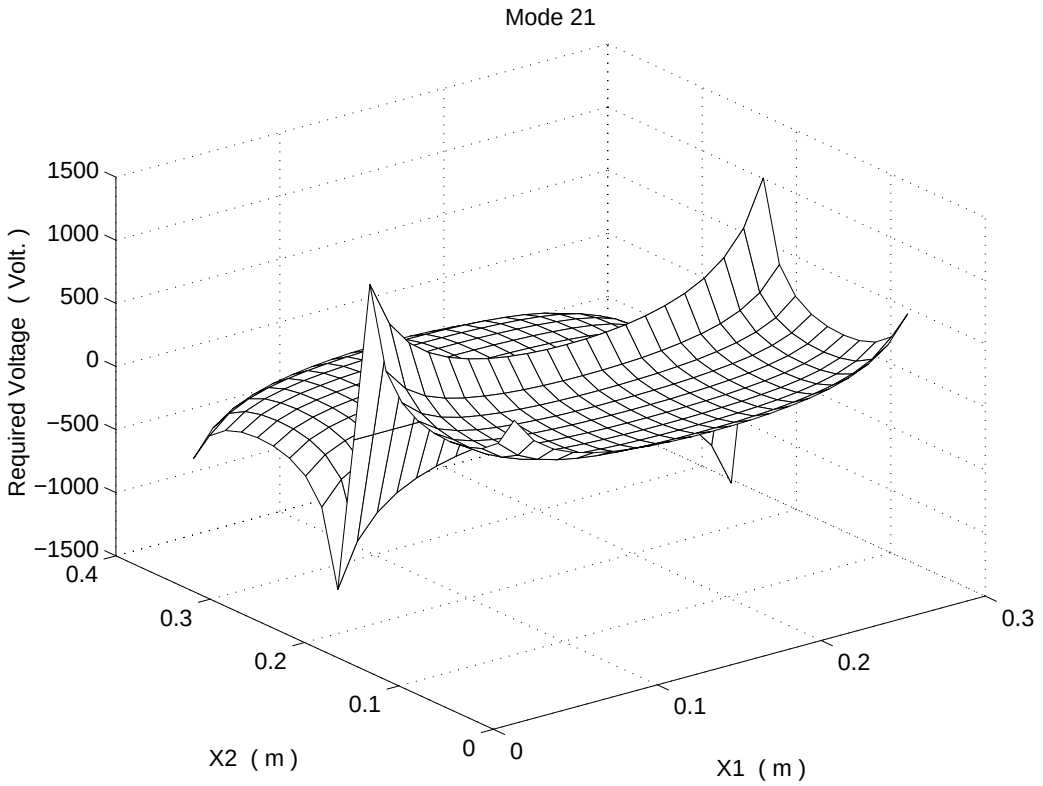

Figure 2.5: Voltage required to suppress the deflections of points on the plate diagonal as a function of the location of the centroid of the 6 cm $\times$ 6 cm PZT region that is excited. The plate is vibrating steadily at a frequency close to Ω_{21}.

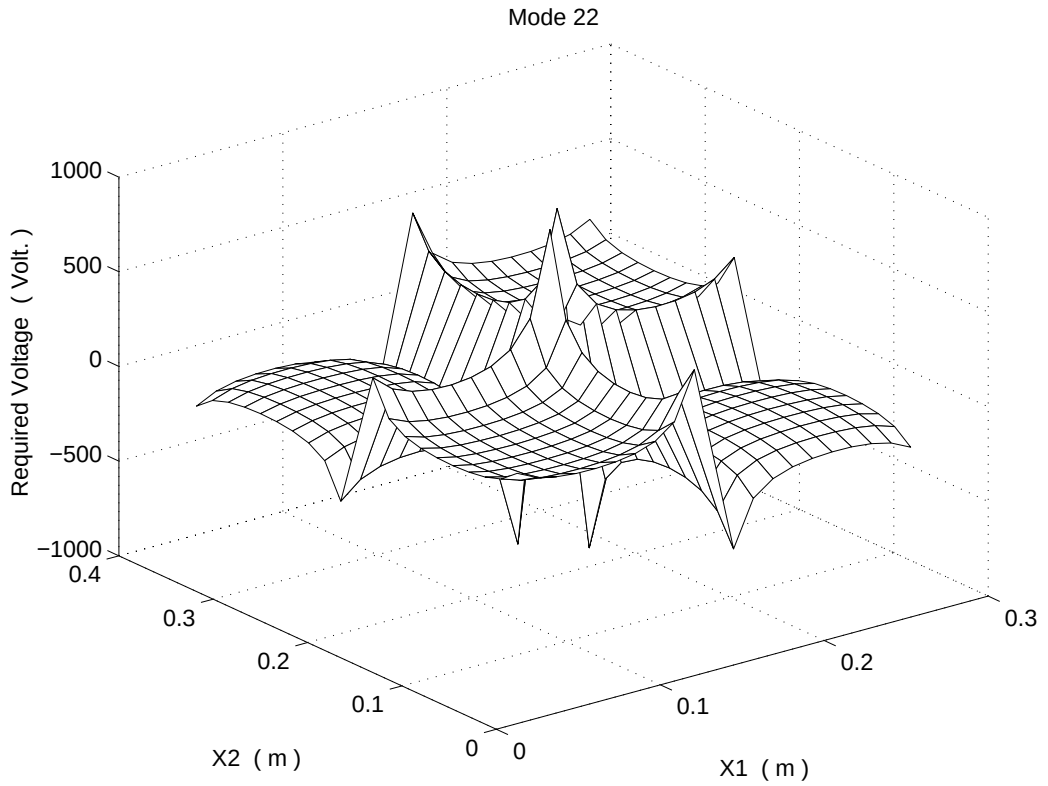

Figure 2.6: Voltage required to suppress the deflections of points on the plate diagonal as a function of the location of the centroid of the 6 cm $\times$ 6 cm PZT region that is excited. The plate is vibrating steadily at a frequency close to Ω_{22}.

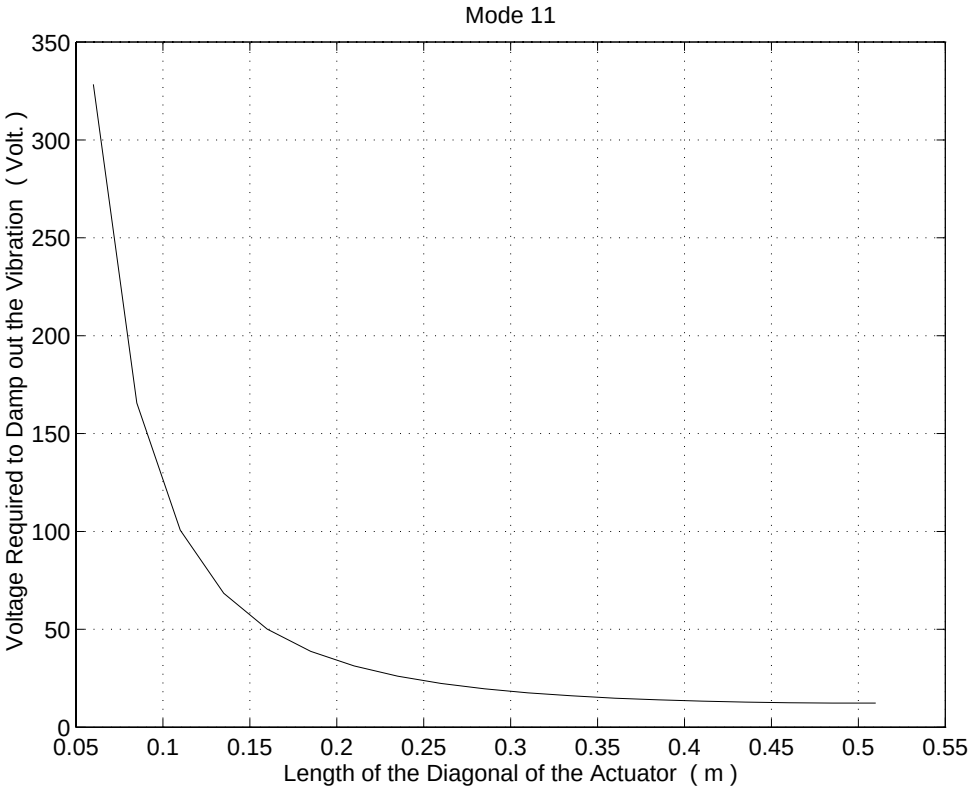

Figure 2.7: Voltage required to suppress the deflections of points on the plate diagonal as a function of the length of the diagonal of the rectangular excited PZT region with its centroid located at an optimum location. The plate is steadily vibrating at a frequency close to Ω_{11}

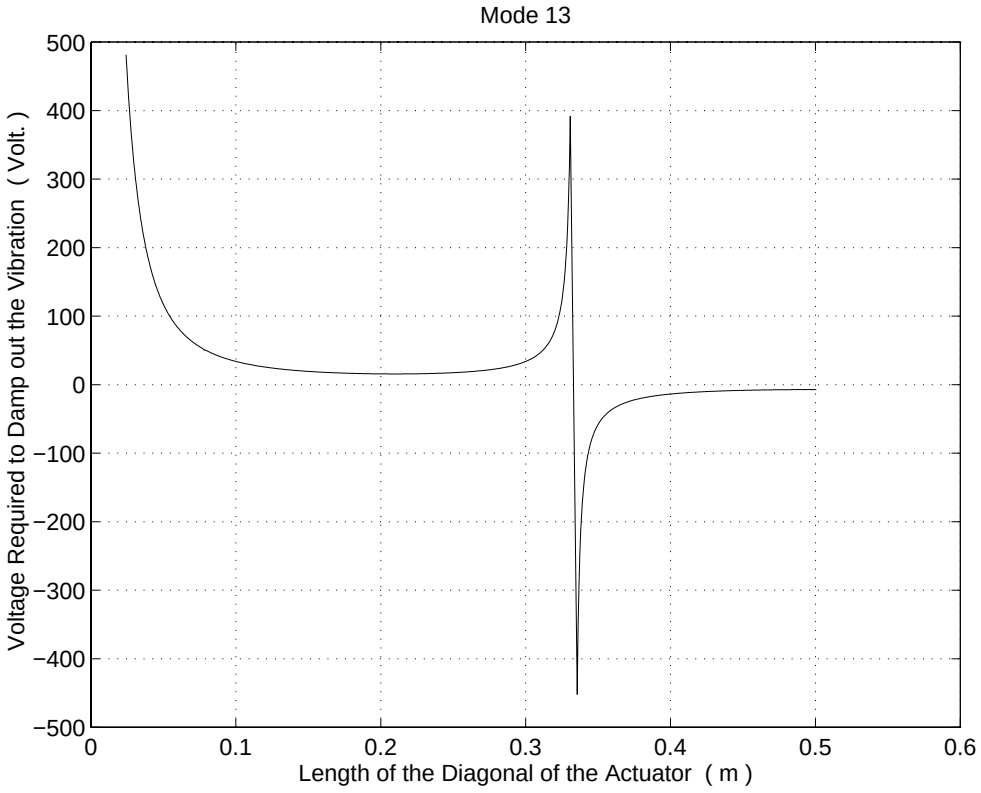

Figure 2.8: Voltage required to suppress the deflections of points on the plate diagonal as a function of the length of the diagonal of the rectangular excited PZT region with its centroid located at an optimum location. The plate is steadily vibrating at a frequency close to Ω_{13}

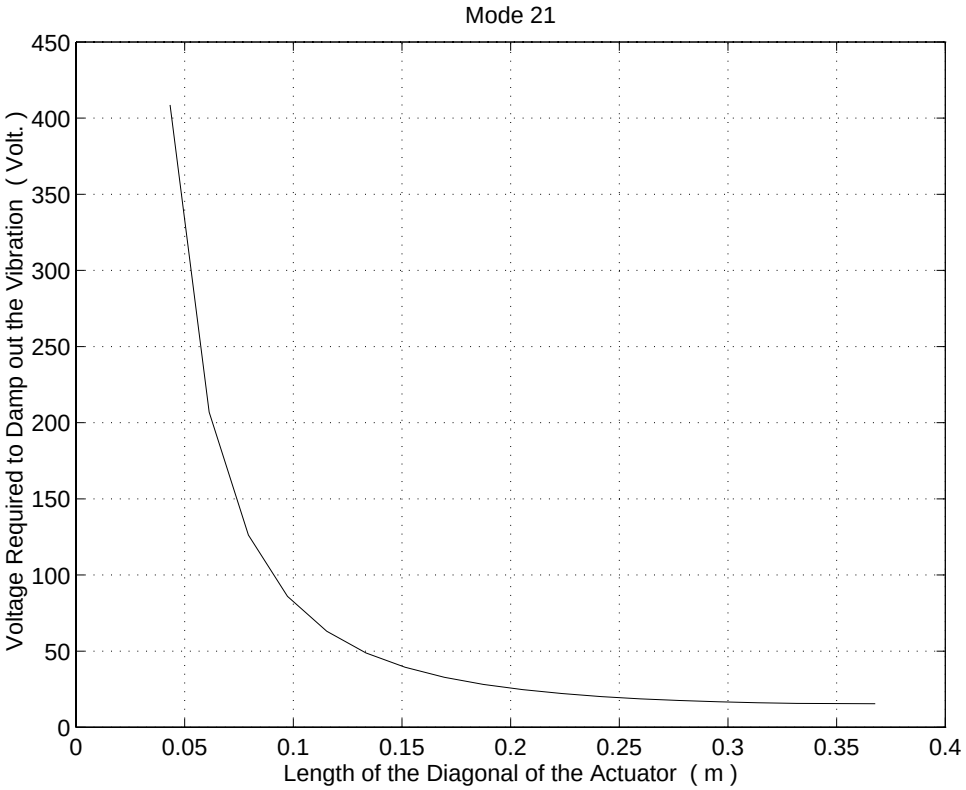

Figure 2.9: Voltage required to suppress the deflections of points on the plate diagonal as a function of the length of the diagonal of the rectangular excited PZT region with its centroid located at an optimum location. The plate is steadily vibrating at a frequency close to Ω_{21}

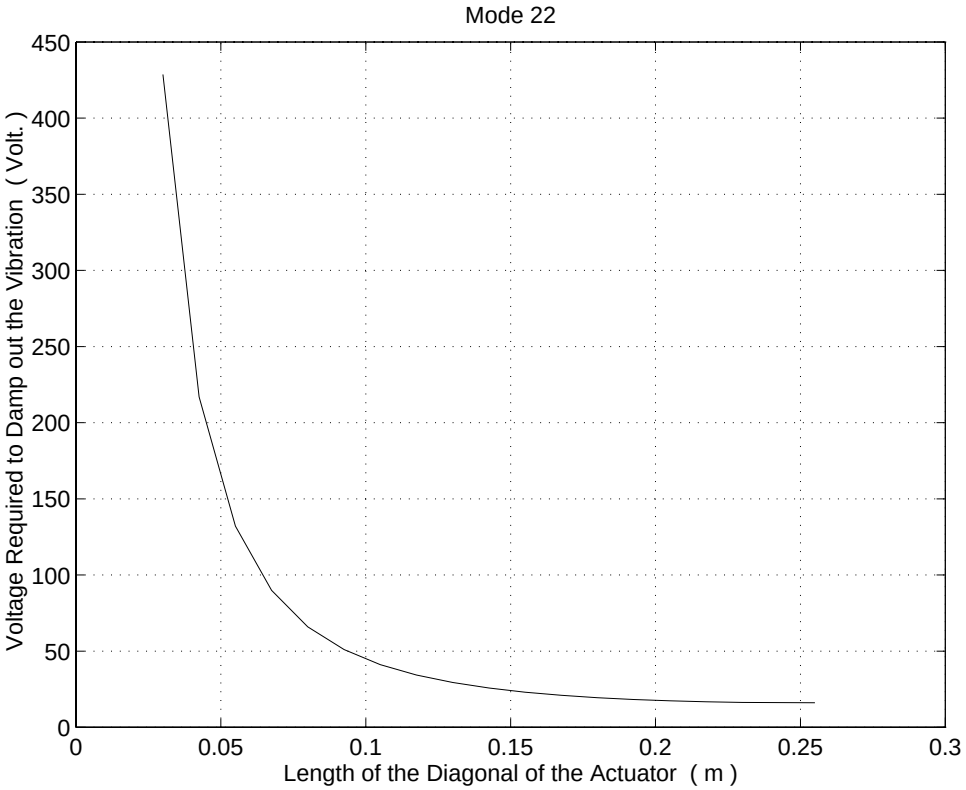

Figure 2.10: Voltage required to suppress the deflections of points on the plate diagonal as a function of the length of the diagonal of the rectangular excited PZT region with its centroid located at an optimum location. The plate is steadily vibrating at a frequency close to Ω_{22}

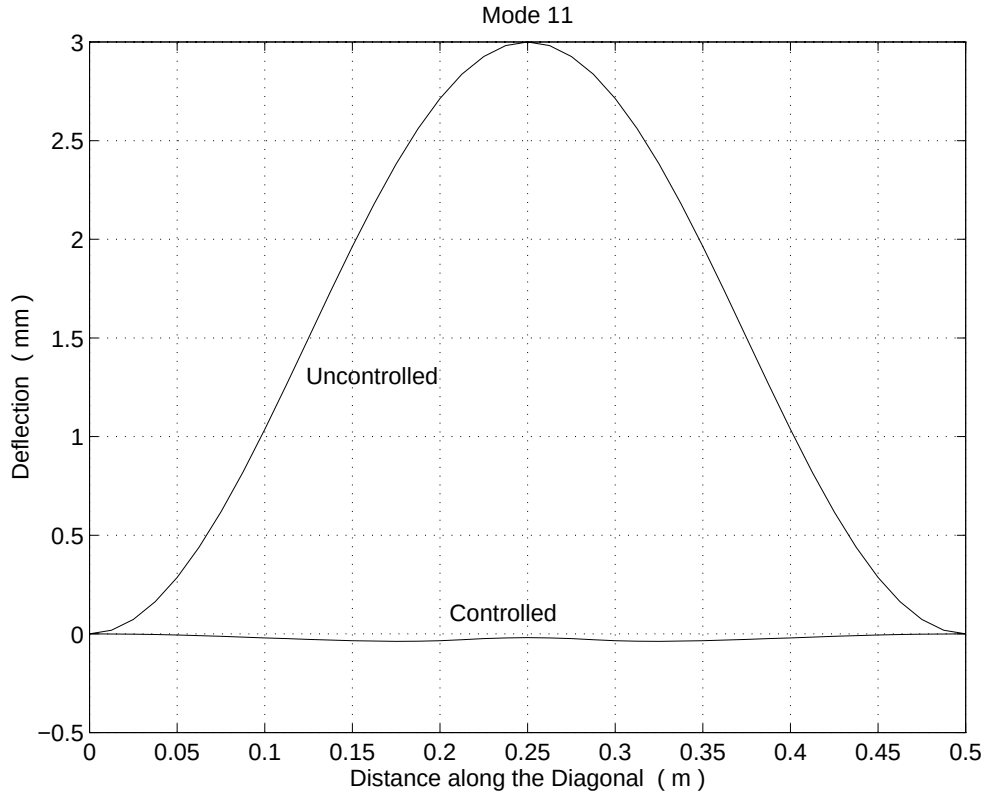

Figure 2.11: Controlled and uncontrolled deformed shape of a diagonal of the plate when it is vibrating steadily at a frequency close to Ω_{11}.

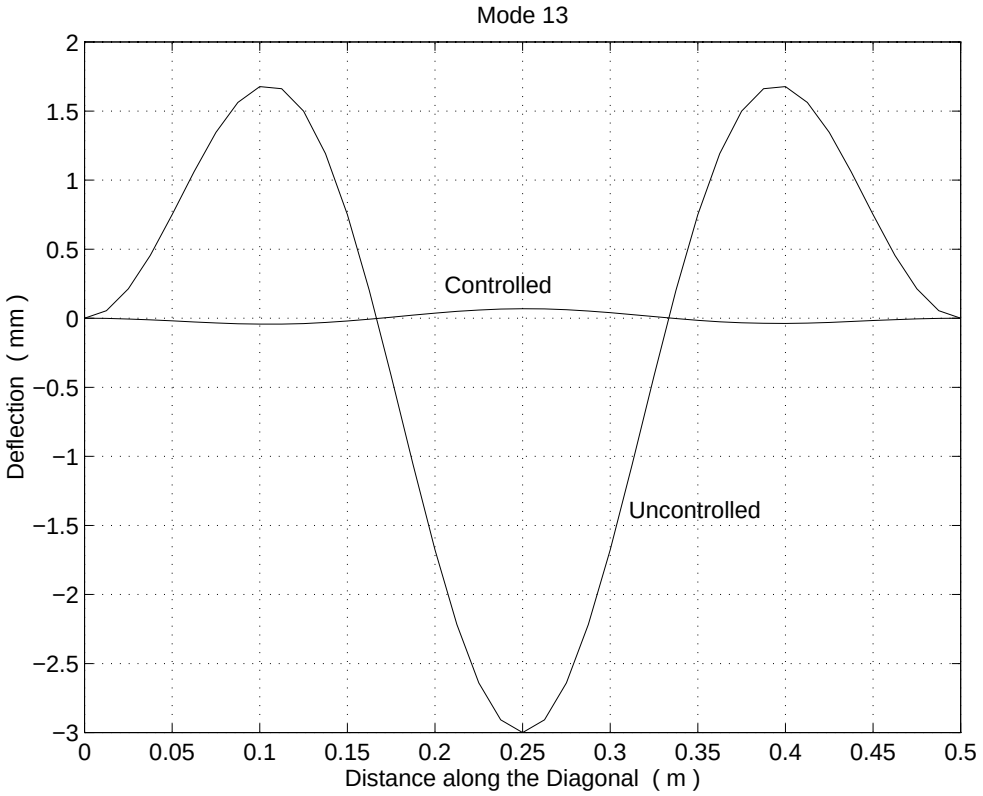

Figure 2.12: Controlled and uncontrolled deformed shape of a diagonal of the plate when it is vibrating steadily at a frequency close to Ω_{13}.

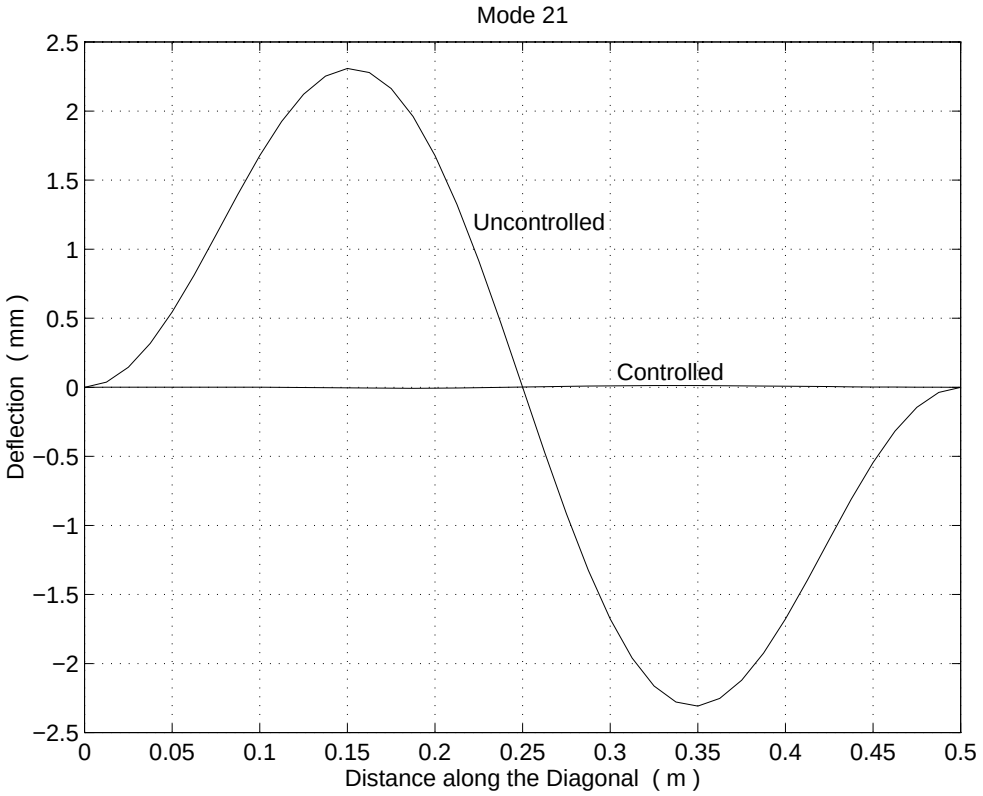

Figure 2.13: Controlled and uncontrolled deformed shape of a diagonal of the plate when it is vibrating steadily at a frequency close to Ω_{21}.

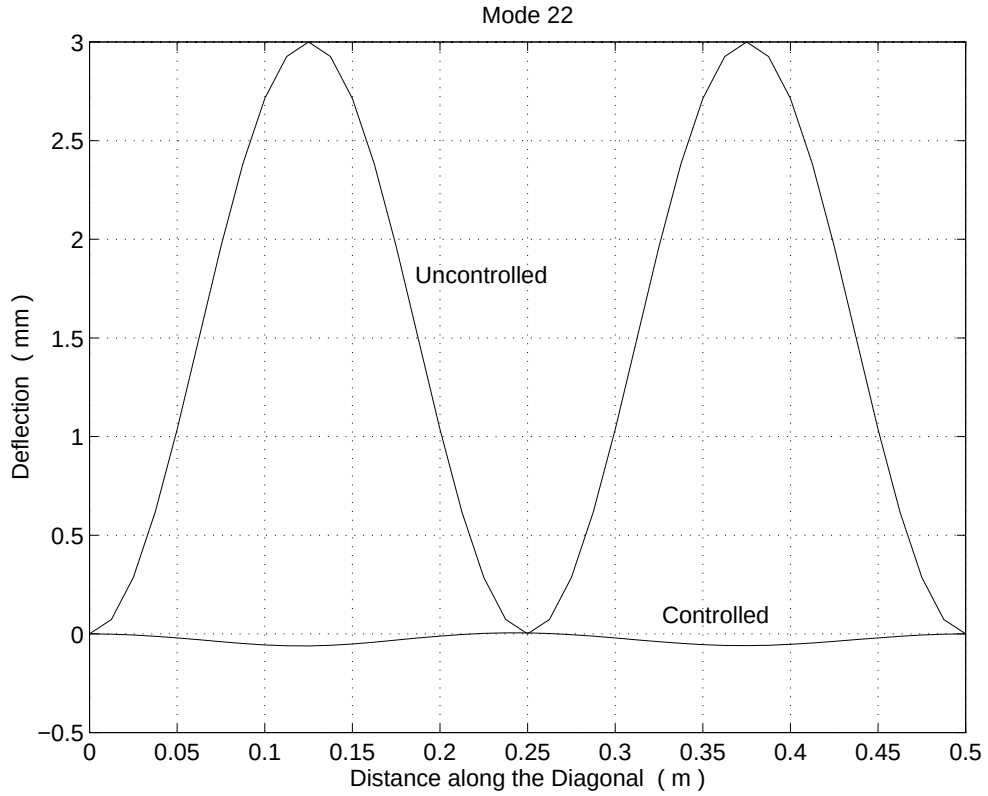

Figure 2.14: Controlled and uncontrolled deformed shape of a diagonal of the plate when it is vibrating steadily at a frequency close to Ω_{22}.

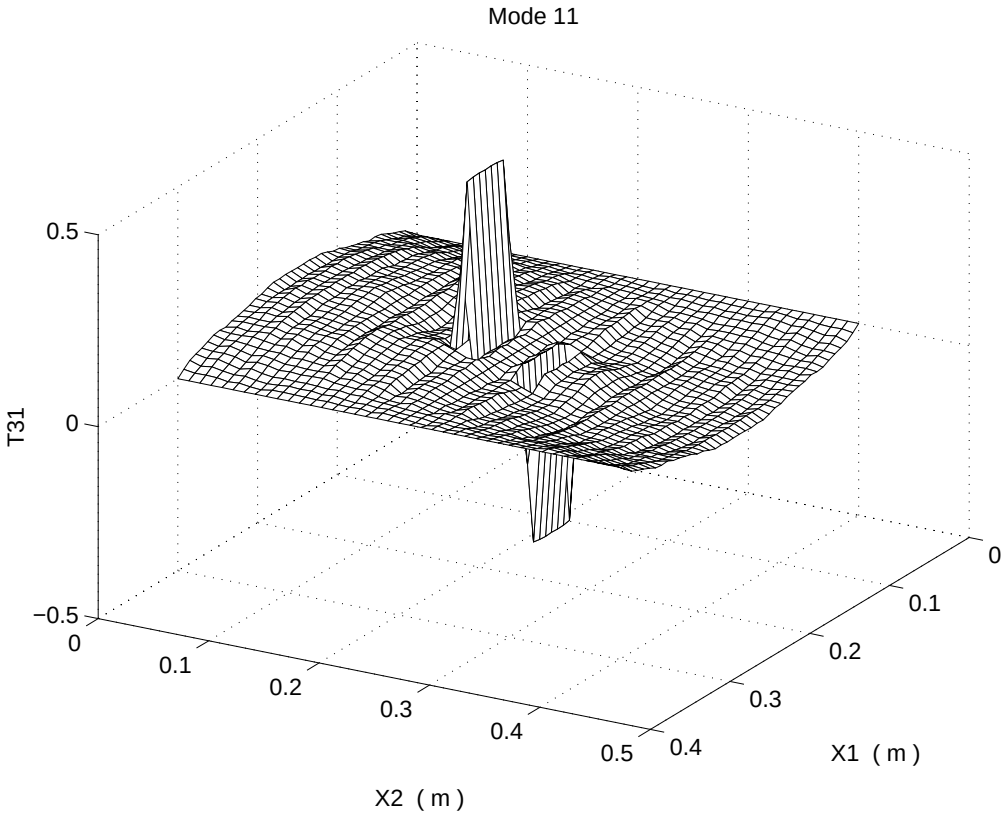

Figure 2.15: The normalized shear stress $T_{31}(x_1, x_2, h) = \tau_{31}(x_1, x_2, h)h^b/e_{31}^b V^b$ under the top actuator for Ω near Ω_{11}.

Chapter 3

Finite Dynamic Deformations of Nonlinear Smart Structures

Abstract

We study transient finite deformations of a neo-Hookean beam or plate with piezoelectric (PZT) patches bonded to its upper and lower surfaces. The constitutive relations for the PZTs are taken to be linear in the Green-Lagrange strain tensor but quadratic in the driving voltage. A finite element code using 8-noded brick elements has been developed and validated by comparing computed results with either analytical solutions or experimental observations. For flexural waves propagating through a cantilever beam, the sensor output is influenced a little by the presence of a defect placed symmetrically about the centroidal axis. A simple feedback control algorithm is shown to control the motion of a neo-Hookean plate subjected to an impulsive load.

3.1 Introduction

Smart structural elements usually consist of a composite substrate and piezoelectric (PZT) patches either bonded to the substrate's outer surfaces or embedded in it. They generally can sense and control their undesired vibrations. They are used to control vibrations of space structures (e.g. see Hall and Muller [1], Dosch et al. [2], and Won et al. [3]), improve acoustics (e.g. see Johnson and Elliot [4], Price and Napoletano [5], and Fuller et al. [6]), and suppress the flutter of aircraft panels (e.g. see Heeg et al. [7] and Song et al. [8]). Because of the difficulty in accurately modeling the interaction between PZTs and the substrate, analytical

[0]A slightly modified version of this chapter will be submitted, for possible publication, to *Computational Mechanics*.

solutions of smart structure problems are limited to their infinitesimal deformations and simple geometries (e.g. see Ray et al. [9], Lagoudas and Bo [10], Brooks and Heyliger [11], Srinivas et al. [12], Wittrick [13], Zhou and Tiersten [14], and Batra and Liang [15]). Numerous authors have used the finite element method (FEM) to analyse smart structural problems by using either beam theories (Hanagud et al. [16], Im and Atluri [17] amongst others), plate theories (Chandrashekhara and Agarwal [18], Batra and Ghosh [19], Samanta et al. [20], and Suleman and Venkayya [21] amongst others), and shell theories (Tzou and Gadre [22], Qiu and Tami [23] amongst others). The three-dimensional FEM method has been used by Allik and Hughes [24], Mollenhauer and Griffin [25], Tzou et al. [26], Hauch [27] and others. Wojicik et al. [28] have argued that the explicit algorithm is more appropriate for studying the transient response of smart structures with large numbers of DOFs.

Whereas foregoing studies have considered infinitesimal deformations and hence have used linear material models, Norwood et al. [29], Kulkarni and Hanagud [30], and Pai et al. [31] have accounted for geometric nonlinearities by using nonlinear strain-displacement relations and linear strain-stress relations in modeling piezoelectric materials. Fully nonlinear material models that account for both large deformations and large electric fields have been studied by Maugin et al. [32] and Tiersten [33,34]. They have derived general forms of constitutive relations containing higher order terms of displacement gradient and electric fields. However, the general models require too many material constants that are hard to measure experimentally. Yang and Batra [35] noticed that the commercially avaliable piezoelectric materials are either transversely isotropic or are of class $mm2$. They have derived second-order form-invariant polynomial constitutive relations for these piezoelectric materials [35]. Huang and Batra [36] have generalized these constitutive equations to include heat conduction and viscous effects. Crawley and Anderson [37] experimentally showed that the normal strain vs. electric field relation for the G1195 PZT is highly nonlinear for driving electric fields exceeding 100 V/mm. Tiersten [38] has successfully modeled these experiments by using a theory linear in displacement gradients but cubic in the electric field.

Here we analyse three-dimensional nonlinear smart structure problems by the FEM and model the substrate and the PZT by second-order form-invariant polynomial constitutive relations [35]. Because of the difficulty in ascertaining values of nonlinear material parameters, results are presented for a neo-Hookean substrate and the PZT modeled by a constitutive relation linear in the Green-Lagrange strain tensor but quadratic in the electric field. Both Crawley and Anderson's experiments on a PZT plate and Moetakef et al.'s [39] experiments on flexural waves in a cantilever aluminum beam generated by PZT patches bonded near its free end are simulated. Computed results are found to be in general agreement with the test observations. The transverse velocity of a point on the surface of a neo-Hookean cantilever beam is not affected much by the presence of a narrow defect near its centroidal axis. A simple feedback control algorithm is shown to control well the vibrations of a cantilever smart plate.

3.2 Formulation of the Problem

Consider a smart structure occupying the region Ω in the reference configuration with region Ω_s occupied by a substrate and Ω_p by a piezoelectric material bonded perfectly to the substrate at their common interface $\partial\Omega_{\text{int}} = \partial\Omega_s \cap \partial\Omega_p$. Using rectangular Cartesian coordinates and the referential description of motion, equations governing finite deformations of the structure are

$$T_{Li,L} + \rho_0 b_i = \delta_{iM}\rho_0 \ddot{u}_M \qquad \text{in} \qquad \Omega = \Omega_s \cup \Omega_p \tag{3.1}$$

$$D_{L,L} = 0 \qquad \text{in} \qquad \Omega_p. \tag{3.2}$$

Here T_{Li} is the first Piola-Kirchhoff stress tensor, upper case indices refer to Cartesian coordinates $\mathbf{X}$ in the reference configuration and lower case indices to those ($\mathbf{x}$) in the present configuration, a comma followed by an index $L(i)$ implies partial differentiation with respect to $X_L(x_i)$, a repeated index implies summation over the range of the index, δ_{iM} is the Kronecker delta, $\mathbf{b}$ the present body force per unit mass, ρ_0 the mass density, $\mathbf{u}$ the displacement of a material point, a superimposed dot indicates the material time derivative, and $\mathbf{D}$ is the electric displacement. Because of small permittivity of the free space, the Maxwell electrostatic stress tensor has been neglected. We have also neglected the effect of body charges and inertia associated with the electric displacement field. The pertinent boundary conditions are

$$\mathbf{u} = \hat{\mathbf{u}} \qquad \text{on} \qquad \partial\Omega_u, \tag{3.3.1}$$

$$T_{Li}N_L = \hat{f}_i \qquad \text{on} \qquad \partial\Omega_t, \tag{3.3.2}$$

$$\phi = \hat{\phi} \qquad \text{on} \qquad \partial\Omega_\phi, \tag{3.3.3}$$

$$D_L N_L = \hat{D} \qquad \text{on} \qquad \partial\Omega_e, \tag{3.3.4}$$

$$[\![\mathbf{u}]\!] = \mathbf{0},\ [\![T_{Li}]\!]N_L = 0 \qquad \text{on} \qquad \partial\Omega_{\text{int}}. \tag{3.3.5}$$

That is displacements are prescribed as $\hat{\mathbf{u}}$ on $\partial\Omega_u$, surface tractions as $\hat{\mathbf{f}}$ on $\partial\Omega_t$, the electric potential as $\hat{\phi}$ on $\partial\Omega_\phi$ and the normal component of electric displacement as $\hat{D}$ on $\partial\Omega_e$. Here $\mathbf{N}$ is an outward unit normal to $\partial\Omega$. In eqns. (3.3.5), $[\![\mathbf{u}]\!] = \mathbf{u}^P - \mathbf{u}^S$ where $\mathbf{u}^P(\mathbf{u}^S)$ denotes the displacements of a piezoelectric (substrate) point on $\partial\Omega_{\text{int}}$. Equations (3.3.5) imply that displacements and surface tractions are continuous across $\partial\Omega_{\text{int}}$ which is equivalent to the assumption that the piezoelectric material and the substrate are perfectly bonded to each other. The electric displacement $\mathbf{D}$ is related to the electric potential ϕ through

$$D_L = P_L + \epsilon_o J X_{L,i} X_{K,i} W_K, \tag{3.4.1}$$

$$W_L = -\phi_{,L}, \tag{3.4.2}$$

where $\mathbf{P}$ is the electric polarization vector, ϵ_0 the permittivity of the free space, $J = \det(F_{iL})$, $F_{iL} = x_{i,L}$, $\mathbf{W}$ is the material electric field vector, and ϕ the electric potential.

We assume that the piezoelectric material is transversely isotropic. Because of the difficulty in determining from the scant experimental data explicit expressions for the response functions of a nonlinear transversely isotropic piezoelectric material, we employ a second-order theory for it. With unit vector $\mathbf{a}$ pointing in the direction of transverse isotropy and assuming that the piezoelectric plate is initially stress free, we postulate the following (Yang and Batra [35]).

$$\begin{aligned}\overline{\mathbf{T}} = &(2c_1I_1 + c_3I_2 + e_1I_3 + 3\lambda_1I_1^2 + 2\lambda_3I_1I_2 + \lambda_4I_2^2 + \lambda_5II_1 + \lambda_7II_2\\ &+ 2\nu_1I_1I_3 + \nu_2I_3^2 + \nu_7II_3 + \nu_9II_4 + \nu_{14}I_2I_3)\mathbf{a}\otimes\mathbf{a}\\ &+ (2c_2I_2 + c_3I_1 + e_2I_3 + 3\lambda_2I_2^2 + \lambda_3I_1^2 + 2\lambda_4I_1I_2 + \lambda_6II_1\\ &+ \lambda_8II_2 + 2\nu_3I_2I_3 + \nu_4I_3^2 + \nu_8II_3 + \nu_{10}II_4 + \nu_{14}I_1I_3)\mathbf{1}\\ &+ (c_4 + \lambda_5I_1 + \lambda_6I_2 + \nu_5I_3)(\mathbf{a}\otimes\mathbf{E}\cdot\mathbf{a} + \mathbf{a}\cdot\mathbf{E}\otimes\mathbf{a})\\ &+ 2(c_5 + \lambda_7I_1 + \lambda_8I_2 + \nu_6I_3)\mathbf{E}\\ &+ (e_3 + \nu_9I_1 + \nu_{10}I_2 + \nu_{11}I_3)(\mathbf{a}\otimes\mathbf{W} + \mathbf{W}\otimes\mathbf{a})\\ &+ 3\lambda_9\mathbf{E}^2 + \nu_{12}\mathbf{W}\otimes\mathbf{W} + \nu_{13}(\mathbf{a}\otimes\mathbf{E}\cdot\mathbf{W} + \mathbf{W}\cdot\mathbf{E}\otimes\mathbf{a} + \mathbf{W}\otimes\mathbf{E}\cdot\mathbf{a} + \mathbf{a}\cdot\mathbf{E}\otimes\mathbf{W}),\end{aligned} \tag{3.5}$$

$$\begin{aligned}-\mathbf{P} = &(2\epsilon_1I_3 + e_1I_1 + e_2I_2 + 3\mu_1I_3^2 + \mu_2II_3 + \nu_1I_1^2 + 2\nu_2I_3I_1 + \nu_3I_2^2\\ &+ 2\nu_4I_3I_2 + \nu_5II_1 + \nu_6II_2 + \nu_{11}II_4 + \nu_{14}I_1I_2)\mathbf{a}\\ &+ 2(\epsilon_2 + \mu_2I_3 + \nu_7I_1 + \nu_8I_2)\mathbf{W} + 2(e_3 + \nu_9I_1 + \nu_{10}I_2 + \nu_{11}I_3)\mathbf{E}\cdot\mathbf{a}\\ &+ 2\nu_{12}\mathbf{E}\cdot\mathbf{W} + 2\nu_{13}\mathbf{E}^2\cdot\mathbf{a}.\end{aligned} \tag{3.6}$$

Here $\overline{\mathbf{T}}$ is the second Piola-Kirchhoff stress tensor, $\mathbf{E}$ the Green-Lagrange strain tensor, and $\mathbf{1}$ the identity tensor. $c_1, c_2 \ldots c_5$, $\lambda_1, \ldots, \lambda_8$, $\nu_1, \ldots, \nu_{14}$, e_1, e_2, e_3, ϵ_1, ϵ_2, μ_1 and μ_2 are material constants, and

$$\begin{aligned}&I_1 = \mathbf{a}\cdot\mathbf{E}\cdot\mathbf{a},\ I_2 = tr\mathbf{E},\ I_3 = \mathbf{a}\cdot\mathbf{W},\ II_1 = \mathbf{a}\cdot\mathbf{E}^2\cdot\mathbf{a},\\ &II_2 = tr\mathbf{E}^2,\ II_3 = \mathbf{W}\cdot\mathbf{W},\ II_4 = \mathbf{a}\cdot\mathbf{E}\cdot\mathbf{W} + \mathbf{W}\cdot\mathbf{E}\cdot\mathbf{a},\end{aligned} \tag{3.7}$$

and $\mathbf{u}\otimes\mathbf{v}$ denotes the tensor product between vectors $\mathbf{u}$ and $\mathbf{v}$. The neo-Hookean model follows from equations (3.5) and (3.6) by keeping only terms linear in $\mathbf{E}$ and $\mathbf{W}$, the small-deformation/large driving voltage theory of Tiersten [38] follows from equations (3.5) and (3.6) when $\mathbf{E}$ is replaced by the infinitesimal strain tensor, and the conventional linear piezoelectric constitutive relations are obtained by keeping only terms linear in $\mathbf{W}$ and the displacement gradients; these equations have been derived by Yang and Batra [35]. The second-order constitutive relation for a transversely isotropic substrate follows from equation (5) by setting $\mathbf{W} = \mathbf{0}$, and that for a neo-Hookean transversely isotropic substrate by keeping terms linear in $\mathbf{E}$. For an orthotropic neo-Hookean substrate

$$\overline{\mathbf{T}} = \mathbf{C}\mathbf{E} \tag{3.8}$$

where the fourth order elasticity tensor $\mathbf{C}$ has the same form as the one in linear elasticity.

The Green-Lagrange strain tensor is related to displacements $\mathbf{u}$ through

$$E_{KL} = (u_{K,L} + u_{L,K} + u_{M,K}u_{M,L})/2, \tag{3.9}$$

and the first and second Piola-Kirchhoff stress tensors are related as

$$T_{Ki} = x_{i,L}\overline{T}_{KL}. \tag{3.10}$$

The Cauchy stress tensor σ_{ij} can be computed from $\overline{T}_{KL}$ by using

$$\sigma_{ij} = J^{-1}x_{i,K}x_{j,L}\overline{T}_{KL}. \tag{3.11}$$

In order to complete the formulation of the problem, we need to specify initial displacements, initial velocities and initial electric potentials; we take these to be zero.

3.3 Finite Element Formulation

Following Hughes [40] the weak formulation of equations (3.1) and (3.2) can be written as

$$\delta_{iM}\delta_{iN}\int_\Omega \rho\ddot{u}_M v_N d\Omega = \delta_{iN}\left[\int_{\partial\Omega_t}\hat{f}_i v_N dS - \int_\Omega T_{Li}v_{N,L}d\Omega\right], \tag{3.12.1}$$

$$\int_\Omega D_L\psi_{,L}d\Omega = \int_{\partial\Omega_e}\hat{D}\psi dS, \tag{3.12.2}$$

where v_N is a virtual displacement vector that vanishes on $\partial\Omega_u$ and ψ is a virtual electric potential that vanishes on $\partial\Omega_\phi$. The left-hand side of equation (3.12.1) equals the virtual work of inertia forces, the first term on its right-hand side represents the virtual work of externally applied tractions, and the second term equals the virtual work done by internal stresses. Note that internal stresses depend upon the mechanical deformation and the electric charge in piezoelectric materials. In equation (3.12.1) we have neglected the body force in the structure. The left-hand side of equation (3.12.2) equals the virtual internal electric energy, and the right-hand side is the virtual electric energy due to surface charge on the piezoelectric material. Substitution for T_{Li} from (3.5) and (3.8), and for D_L from (3.4.1), (3.4.2) and (3.6) yields equations for the determination of displacements $\mathbf{u}$ and the electric potential ϕ.

We discretize the domain Ω into the union of 8-noded brick elements and employ a $2\times 2\times 2$ quadrature rule to numerically evaluate various integrals over an element. Referring the

reader to Hughes [40] for details, we note that equations (3.12) yield the following set of coupled nonlinear ordinary differential-algebraic equations.

$$\mathbf{M}\ddot{\mathbf{d}} = \mathbf{F}^{\text{ext}}(t) - \mathbf{F}^{\text{int}}(t), \tag{3.13}$$

$$\mathbf{P}_{\text{int}}(\mathbf{d}(t),\ \mathbf{\Phi}(t)) = \mathbf{P}_{\text{ext}}(t). \tag{3.14}$$

Here $\mathbf{M}$ is the mass matrix which we take as lumped, $\mathbf{d}$ the vector of nodal mechanical displacements in both the substrate and piezoelectric elements, $\mathbf{\Phi}$ the vector of nodal electric potential in piezoelectric elements only, $\mathbf{F}^{\text{ext}}$ and $\mathbf{F}^{\text{int}}$ are vectors of nodal forces equivalent to externally applied surface tractions and internal stresses respectively, $\mathbf{P}_{\text{int}}$ is the nodal charge vector equivalent to internal polarization in piezoelectric elements, and $\mathbf{P}_{\text{ext}}$ is the externally applied nodal charge vector.

Equations (3.13) are solved by the central-difference method. For linear problems, this technique and the lumped mass matrix yield exact time periods for the waves; it is hoped that the error, if any, in the time period for nonlinear waves will be small. Thus knowing the nodal mechanical displacements and electric potentials at time t_n, their values at time $t = t_{n+1}$ are given by

$$\mathbf{d}(t_{n+1}) = \Delta t_2 \left[\mathbf{M}^{-1} \left(\mathbf{F}^{\text{ext}}(t_{n+1}) - \mathbf{F}^{\text{int}}(t_n) \right) \frac{\Delta t_1 + \Delta t_2}{2} + \left(\frac{1}{\Delta t_1} + \frac{1}{\Delta t_2} \right) \mathbf{d}(t_n) + \frac{\mathbf{d}(t_{n-1})}{\Delta t_1} \right] \tag{3.15}$$

where $\Delta t_1 = t_n - t_{n-1},\ \Delta t_2 = t_{n+1} - t_n$. Recalling that the central-difference method with the lumped mass matrix is explicit and conditionally stable, we take

$$\Delta t = 1.8/\omega_{\max} \tag{3.16}$$

where $\omega_{\max}$ is the maximum frequency of free vibration of the discretized structure. Essential boundary conditions must be enforced when solving equations (3.13) or (3.15). Because the problem being studied is nonlinear, $\omega_{\max}$ needs to be computed after every time step. In equation (3.15), the calculation of $\mathbf{d}(t_{n+1})$ involves $\mathbf{d}(t_n)$ and $\mathbf{d}(t_{n-1})$. Therefore, a special starting procedure must be used to calculate $\mathbf{d}(\Delta t_2)$. Since the displacement and velocity at time 0 are known and the acceleration at time 0 can be solved from equation (3.13); $\mathbf{d}(-\Delta t_1)$ can be obtained (Bathe [43]). Equation (3.15) can then be used repeatly for subsequent time steps.

We use the Newton-Raphson iterative method to solve equation (3.14) fot $\mathbf{\Phi}(t_{n+1})$and write it in the incremental form as

$$\mathbf{J}(\mathbf{\Phi}(t_n), \mathbf{d}(t_{n+1}))\Delta\mathbf{\Phi}^{(i)}(t_{n+1}) = -\mathbf{P}_{\text{int}}(\mathbf{\Phi}^{(i-1)}(t_{n+1}),\ \mathbf{d}(t_{n+1})) + \mathbf{P}_{\text{ext}}(t_{n+1}), \tag{3.17}$$

where

$$
\begin{aligned}
&J(\mathbf{\Phi}(t_n), \mathbf{d}(t_{n+1})) = \left.\frac{\partial \mathbf{P}_{\text{int}}}{\partial \mathbf{\Phi}}\right|_{(\Phi(t_n), \mathbf{d}(t_{n+1}))}, \\
&\mathbf{\Phi}^{(i)}(t_{n+1}) = \mathbf{\Phi}^{(i-1)}(t_{n+1}) + \Delta\mathbf{\Phi}^{(i)}(t_{n+1}), \\
&\mathbf{\Phi}^{(0)}(t_{n+1}) = \mathbf{\Phi}(t_n).
\end{aligned} \tag{3.18}
$$

The iterative process is stopped when

$$
\|\Delta\mathbf{\Phi}^{(i)}(t_{n+1})\| / \|\mathbf{\Phi}^{(i)}(t_{n+1})\| \leq \epsilon, \tag{3.19}
$$

ϵ being a preassigned small tolerance; it was set equal to 10^{-5} for results presented below.

For a smart structure, the number of nodal mechanical displacements far exceeds the number of nodal electrical potentials and the aforementioned explicit/implicit technique of analysing the problem is computationally more effective than the conventional implicit techniques.

3.4 Computation and Discussion of Results

3.4.1 Validation of the code

A finite element code based on the formulation given above has been developed and debugged. It was validated first by solving a dynamic problem for a clamped-clamped square graphite/epoxy plate modeled as a linear elastic orthotropic lamina. The response of the plate subjected to a suddenly applied point load at its center computed with the present code matched very well with that computed with ABAQUS [41]. We note that ABAQUS first computes the eigenmodes and thus decouples the mechanical degrees of freedom. For the quarter of the 200 mm $\times$ 200 mm $\times$ 1 mm plate divided into $10 \times 10 \times 1$ elements, we considered the first 100 eigenmodes to compute the solution with ABAQUS.

For the second test problem, we assumed the following displacement fields:

$$
\begin{aligned}
&\text{Case 1: } u_1 = 20X_L X_L \sin\Omega t,\ u_2 = 0,\ u_3 = 0; \\
&\text{Case 2: } u_1 = 0,\ u_2 = 20X_L X_L \sin\Omega t,\ u_3 = 0; \\
&\text{Case 3: } u_1 = u_2 = 0,\ u_3 = 10^5 X_2^2 X_3^2 \sin\Omega t;
\end{aligned} \tag{3.20}
$$

and set $\Omega = 0.1257 \times 10^6/s$. For an orthotropic neo-Hookean plate, we computed the body force required to satisfy the balance of linear momentum in equation (3.1), the initial displacement and velocity field, and displacements at the edges of the plate. The developed code was used to analyse the problem with these initial and boundary conditions and body

forces. The computed displacements were compared with those given by equations (3.20). In each case, the computed solution was found to match well with the corresponding analytical solution of the problem.

A third test problem analysed was an 80 mm $\times$ 8 mm $\times$ 0.5 mm graphite/epoxy cantilever lamina with an 8 mm $\times$ 8 mm $\times$ 0.5 mm piezoelectric (PZT) sensor affixed, with its left edge 40 mm from the clamped edge, to its top surface. An other PZT sensor, with the same geometry, was symmetrically fixed to the bottom of the lamina. Both materials were modeled as linear elastic with the lamina as orthotropic and the PZT as transversely isotropic; values of material parameters given in Batra and Liang [15] were used. A point load was applied at each corner of the free end; the load increased linearly from 0 to 1N in 200 μs, was maintained at 1N for 100 μs and then decreased linearly to 0 in 200 μs. The time histories of the transverse displacement of the point of application of the point load and the voltage output at the top right corner of the PZT patch as computed by ABAQUS (Version 5.2) and the present code are plotted in Figs. 3.1 and 3.2; it is clear that the two results agree well. We note that problems involving nonlinear response of PZTs can not be analysed with ABAQUS.

Crawley and Anderson [37] applied large driving voltages to both the top and bottom surfaces of an unconstrained PZT-G1195 plate and found the induced tensile strain to be highly nonlinear with respect to the electric field. Tiersten [38] modeled the experiment as a plane-stress problem and used a theory linear in displacement gradients but cubic in the driving electric field. He determined the material constants for the PZT by the least squares method and found that the computed response matched very well with the observed one. Here we simulate Crawley and Anderson's experiment by using our code for a 20 mm $\times$ 10 mm $\times$ 0.25 mm plate. The edges of the unconstrained PZT plate are taken to be stress free, and points on the bottom surface are constrained from moving in the thickness direction. A uniform voltage increasing linearly at 100 V/μs is applied to the top surface with the bottom surface grounded. Because of the symmetry of the problem about the two centroidal axes, only a quarter of the plate is modeled by a $20 \times 10 \times 2$ uniform mesh. To study the small deformation/large electric field problem, it is reasonable to model the PZT-G1195 by the following constitutive relation, obtained from (3.5) and (3.6) by retaining terms linear in $\mathbf{E}$ but quadratic in $\mathbf{W}$

$$
\begin{aligned}
\overline{\mathbf{T}} &= (2c_1 I_1 + c_3 I_2 + e_1 I_3 + \nu_2 I_3^2 + \nu_7 I I_3)\mathbf{a}\otimes\mathbf{a} \\
&\quad + (2c_2 I_2 + c_3 I_1 + e_2 I_3 + \nu_4 I_3^2 + \nu_8 I I_3)\mathbf{1} + c_4(\mathbf{a}\otimes\mathbf{E}\cdot\mathbf{a} + \mathbf{a}\cdot\mathbf{E}\otimes\mathbf{a}) + 2c_5\mathbf{E} \\
&\quad + (e_3 + \nu_{11} I_3)(\mathbf{a}\otimes\mathbf{W} + \mathbf{W}\otimes\mathbf{a}) + \nu_{12}\mathbf{W}\otimes\mathbf{W}, \\
-\mathbf{P} &= (2\epsilon_1 I_3 + e_1 I_1 + e_2 I_2 + \mu_2 I I_3 + 2\nu_2 I_1 I_3 + 2\nu_4 I_2 I_3 + \nu_{11} I I_4)\mathbf{a} \\
&\quad + 2(\epsilon_2 + \mu_2 I_3 + \nu_7 I_1 + \nu_8 I_2)\mathbf{W} + 2(e_3 + \nu_{11} I_3)\mathbf{E}\cdot\mathbf{a} + 2\nu_{12}\mathbf{E}\cdot\mathbf{W}.
\end{aligned} \tag{3.21}
$$

We note that equations (3.21) account for both geometric nonlinearity due to finite deformation and material nonlinearity due to large electric field for piezoelectric materials. The

values of material constants for PZT-G1195 corresponding to terms linear in **E** and **W** are easy to get from conventional piezoelectric constants (Yang and Batra [35]). The material constants multiplying nonlinear terms are, however, hard to find. When a thin PZT actuator is poled in the x_3-direction and the voltage difference is also applied in the x_3-direction, W_1 and W_2 are so small compared to W_3 that they are negligible. For thin PZT actuators, ν_4 and ν_{12} can represent the contributions from terms quadratic in **W**. Their values for PZT-G1195, determined in [38], are used herein. We assigned following values to material parameters for PZT-G1195 (see Tiersten [38]).

$$\begin{aligned}
&c_1 = 29 \text{ GPa},\ c_2 = 38.1 \text{ GPa},\ c_3 = -2 \text{ GPa},\ c_4 = -21 \text{ GPa},\ c_5 = 35.9 \text{ GPa},\\
&e_1 = 13.4757 C/m^2,\ e_2 = -39.8583 C/m^2,\ e_3 = 0,\ \rho = 7,500 \text{ kg/m}^3,\\
&\nu_4 = -0.903 \times 10^{-4}\ Pa\ m^2/V^2,\ \nu_{12} = 0.3054 \times 10^{-4}\ Pa\ m^2/V^2,\\
&\epsilon_0 = 8.8419 \times 10^{-12}\ N/V^2,\ \epsilon_1 = 1.081 \times 10^{-9}\ N/V^2,\ \epsilon_2 = -2.22558 \times 10^{-9}\ N/V^2.
\end{aligned} \tag{3.22}$$

The computed variation at the PZT centroid of the lateral tensile strain with the transverse electric field is compared in Fig. 3.3 with the test results and also with that given by Tiersten. It is clear that our result is in excellent agreement with Tiersten's analytical result, and in good agreement with Crawley and Anderson's experimental result. Tiersten incorporated a third-order term in the electric field, and obtained results very close to the test values.

3.4.2 Flexural Waves in a Cantilever Beam

We now simulate experiments of Moetakef et al. [39] on wave propagation in a beam and delineate the effects of the nonlinear response of PZTs. Their experimental set up, consists of a 1500 mm × 25.4 mm × 3.175 mm cantilever 6061-T65 aluminum beam with two 25.4 mm × 25.4 mm × 1.3716 mm PZT-850 patches bonded to its upper and lower surfaces abutting the free edge (Fig. 3.4). A single sinusoidal pulse of electric potential difference of 500 V amplitude and 500 μs time period is applied to the PZT patches. The transverse velocity at six points A through F on the top surface of the beam was measured by a fiber optic interferometer. With the origin of the rectangular Cartesian coordinate system at the centroid of the free end, x_3-axis pointing upwards and x_1-axis into the beam, coordinates (in mm) of points A through F are (0, 1.5875, 2.9591), (6.35, 1.5875, 2.9591), (19.05, 1.5875, 2.9591), (101.6, 1.5875, 1.5875), (152.4, 1.5875, 1.5875), (203.2, 1.5875, 1.5875). Thus points A, B and C are on the longitudinal edge of the top surface of the PZT patch, and D, E and F are on the longitudinal edge of the top surface of the aluminum beam. Due to the symmetry about the x_1-x_3 plane, only half of the structure is modeled. Additionally, because the generated disturbance is in the form of plane waves perpendicular to the direction of propagation, a one-element model in the x_2-direction is sufficent in the FEM simulation (Moetakef et al. [39]). In the present study, we take one element in the x_2-direction in order to save on the computational time. The aluminum beam is divided into two portions. In the region with $x_1 < 476.25$ mm, wherein points A through F are located, a finer mesh with

the element size (in mm) $1.5875 \times 1.5875 \times 0.79375$ is used; elsewhere a coarser mesh with the element size (in mm) $3.175 \times 1.5875 \times 0.79375$ is used. The element size for the PZT actuators is (in mm) $1.5875 \times 1.5875 \times 0.6858$. As a result, the Aluminum beam is divided into $622 \times 1 \times 4$ 8-node brick elements, and each PZT patch into $16 \times 1 \times 2$ 8-node brick elements. The values of material constants for the PZT-850 are taken to be the same as those for the PZT-2 (the two are equivalent according to the American Piezoceramics Inc.). These and material paramters for aluminum modeled as an isotropic material are listed below.

Piezoelectric material:

$$\begin{aligned} &c_1 = 23.1 \text{ GPa},\ c_2 = 33.944 \text{ GPa},\ c_3 = 199.6 \text{ MPa},\ c_4 = -22.535 \text{ GPa}, c_5 = 33.49 \text{ GPa}, \\ &e_1 = 8.67544 \text{ C/m}^2,\ e_2 = 1.85657 \text{ C/m}^2,\ e_3 = -9.77768 \text{ C/m}^2, \\ &\epsilon_0 = 8.8419 \times 10^{-12} \text{ N/V}^2,\ \epsilon_1 = 1.08 \times 10^{-9} \text{ N/V}^2,\ \epsilon_2 = -2.22558 \times 10^{-9} \text{ N/V}^2, \\ &\rho = 7,600 \text{ kg/m}^3 \end{aligned} \tag{3.23}$$

Aluminum:

$$\rho = 2,700 \text{ kg/m}^3,\ \text{Young's modulus} = 68.965 \text{ GPa},\ \text{Poisson's ratio} = 0.3269.$$

Time histories of the transverse velocity at points A through F as computed by the present code using the infinitesimal theory, observed experimentally, and computed by Moetakef et al. [39] by the finite element method are plotted in Figs. 3.5 through 3.10; Moetakef et al. used tetrahedral elements and a Newmark-Wilson time integration scheme, and modeled a quarter of the structure. Their finite element mesh had one element in the thickness direction in the PZT and in the aluminum beam. The two sets of computed results agree well for point A. However, both results differ noticeably from the experimental data. For points B and C present numerical results agree well with the experimental results. For points D, E, and F on the aluminum beam, our computed results are closer to the experimental results than those of Moetakef et al.. However, the frequencies of numerical results (both our and Moetakef et al.'s simulations) are higher than those of the experimental results for points D, E and F. Factors for the difference between the computed and experimental results include the higher stiffness of the discrete model, neglecting in the FE model the effect of the adhesive layer between the PZT patch and the aluminum beam, differences between the values of material constants for the PZT-850 and the PZT-2, ignoring hysteresis in the PZT, collecting every eighth data point in the experiment, smoothening of the test data, and the generated wave being not a plane wave.

Time histories of the axial and lateral strains and the axial and lateral normal stresses at four points on the vertical line through the point (6.685 mm, 0.335 mm, 0) are exhibited in Figs. 3.11 through 3.14; time histories of the other components of strain and stress are omitted for brevity. Note that points P and Q are in the beam, and R and S are in the top PZT patch. The inplane shear strain E_{12} was found to be three orders of magnitude smaller than the axial strain, and E_{13} an order of magnitude smaller than the axial strain. E_{23} in the PZT patches was found to be nearly one-tenth of the axial strain, and was of the

same order of magnitude as the axial strain in the Aluminum beam. The transverse normal strain, E_{33}, was found to be of the smae order as the axial strain but 180° out of phase with E_{11}. The normal strains in the x_1- and x_2-directions are of the same order of magnitude, and are in phase with each other; each curve is a sine wave of 500 μs duration implying that a sinusoidal impulse generates sinusoidal strains and stresses. We recall that the vertical line under consideration passes through the PZT patches and the computed results indicate that the axial and lateral normal stresses at points P and Q in the PZT patch are compressive but those at points R and S are tensile.

Since values of ν_4 and ν_{12} for PZT-850 or PZT-2 are unknown, we assume that they are in the same range as those for PZT-G1195 tested by Crawley and Anderson [37] and examined above. In the present study, we computed results for three different values (in $Pa\ m^2/V^2$) 0, -1×10^{-4}, -2×10^{-4} for ν_4, and three different values (in $Pa\ m^2/V^2$) 0, 0.3×10^{-4}, 0.5×10^{-4} for ν_{12}. In order to account for possible finite deformations of the structure, the Green-Lagrange strain tensor was used in the simulations. Figures 3.15 through 3.20 depict, for three different values of ν_4, with $\nu_{12} = 0$, the time-histories of the transverse velocity and displacement of points B and C, and of the axial strain and stress at the point (6.685, 0.335, 2.418) mm in the top PZT patch; results for other points are omitted. It is found that ν_4 has a small effect on the transverse veolcity and deflection of point A, and has no effect on the transverse velocity and displacement of points D, E, and F. However, ν_4 affects noticeably the transverse velocity and displacement of points B and C. The overall agreement between the computed and observed transverse velocities at the six points A through F, described above, is not improved by considering the terms with ν_4. We notice, however, that the agreement between the computed and observed transverse velocities at point B is better for $\nu_4 = -1\times10^{-4}\ Pa\ m^2/V^2$. Figures 3.21 through 3.26 depict, for three different values of ν_{12}, with $\nu_4 = 0$, the time-histories of the transverse velocity and displacement of points B and C, and of the axial strain and stress at the point (6.685, 0.335, 2.418) mm in the top PZT patch; results for other points are omitted. As was the case for ν_4, ν_{12} has a small effect on the transverse velocity and displacement at point A, has no effect on the transverse velocity and displacement at points D, E, and F, but has noticeable effect at points B and C.

All components of the strain and stress tensors at the point (6.685, 0.335, 2.418) mm in the top PZT patch are significantly influenced by the values of ν_4 and ν_{12}. The longitudinal strain and stress are no longer a sinusoidal function of time for the nonlinear PZTs. The magnitude of T_{11} is much higher for the nonlinear PZTs as compared to that for the linear PZTs. Also, the response for the positive applied voltage is quite different from that for the negative applied voltage. In their experiment, Moetakef et al. studied the propagation of waves for 1 ms only. This time period is not long enough for the flexural wave to reach the fixed end of the beam, and the response observed at the actuators is due to the input waves only. In order to save computer time, we simulated the problem for the same time period as Moetakef et al.'s experiment.

3.4.3 Flexural Waves in a Defective Cantilever Beam

In an attempt to see if the propagation of flexural waves in a cantilever beam can be used to delineate a defect in it, we use Moetakef et al.'s ([39]) set up discussed above but introduce a 9.525 mm $\times$ 1.5875 mm $\times$ 1.5875 mm weak region located symmetrically about the midplane at 184.15 mm from the free edge. The elastic constants for the material in the weak region equalled 10^{-5} of those in the remainder of the beam. Figures 3.27 through 3.29 depict the time histories of the transverse displacement, transverse velocity, and the voltage output from the PZT sensor bonded to the upper surface of the beam at a distance of 233.36 mm from the free edge. The results exhibited are for a neo-Hookean beam, but similar results were obtained for a linear elastic beam. The differences in the time-history of the transverse displacements, velocities and electric potentials for beams with and without defects are not large enough for the technique to be of practical use.

3.4.4 Active Control of a Nonlinear Cantilever Plate

We now consider a three-layer (0/90/0) 60 mm $\times$ 40 mm $\times$ 3 mm graphite/epoxy cantilever plate with nine PZT-G1195 sensors bonded to its top surface and nine PZT-G1195 actuators affixed to its bottom surface as shown in Fig. 3.30. Each PZT patch is prepoled in the x_3-direction. We use aforestated values of material parameters for the PZT (equation (3.22)) and the graphite/epoxy layer. The goal is to suppress vibrations of the plate when a sinusoidal impact force of amplitude 20 N and time period 2 ms is applied for 1 ms at each node on the free edge.

In order to actively control the structure, each sensor is connected to a corresponding actuator to form a closed-loop system. In the present study, a simple constant-gain position feedback control algorithm is employed (Ha et al.[42]). The ith sensor output is multiplied by a gainfactor, G_i, and the resulting voltage is uniformly applied to the ith actuator. In practical smart structures, the voltage induced in a sensor generally does not affect much its mechanical response through the converse piezoelectric effect. Hence we presume that the dynamic output from a sensor is due to its mechanical deformations only. We assume that the gain factor, $G_i = 10^7\ V/m$, is the same for each sensor-actuator pair. The open-loop responses of the structure using both linear elastic and neo-Hookean material models were found to be virtually indistinguishable from each other because of the infinitesimal strains induced. Results presented herein are for the neo-Hookean material and the response of the piezoelectric material represented by equations (3.21) with material parameters given by (3.22).

We focus on suppressing the vibrations of points A through F shown in Fig. 3.30, and accomplish this by using first the two sensors and the two actuators nearest to the fixed support, then by using these two and also the adjoining pairs, and finally all six pairs.

Figures 3.31 through 3.36 depict the time histories of the transverse displacement of points A-F for these three cases, and also for the uncontrolled case. We notice that for the closed-loop smart plate, the following two loads contribute to its deflections. The applied impulse force at the free edge of the plate drives the points in the direction of the applied force. At the same time, the tractions at the interfaces between the actuator patches and the plate, due to the feed-back voltage on the actuator, drive the points in a direction opposite to that of the applied force. As a result, the magnitude of the deflection of the plate is smaller for the closed-loop plate than that for the uncontrolled plate. It can be seen from Figures 3.31 through 3.36 that after the removal of the applied force, the plate vibrates with a constant amplitude, which is much smaller than that of the uncontrolled plate. It is clear that the actuators placed near the free end are more effective in diminishing the vibrations of points A-F, and the sensor/actuator pairs located close to the fixed end of the plate slightly reduce the amplitude of vibrations of points A-F.

3.5 Conclusions

We have developed and validated a finite element code to analyse 3-dimensional transient deformations of a neo-Hookean body with nonlinear piezoelectric patches either affixed to its bounding surfaces or embedded in it. The code has been used to analyse Crawley and Anderson's experiment on ascertaining the response of an unconstrained PZT plate to large driving voltages, and Moetakef et al.'s experiment on the propagation of flexural waves in a cantilever beam. In each case the computed and observed results are found to agree with each other within acceptable limits. The code is then used to study the propagation of flexural waves in a defective neoHookean cantilever beam, and the sensor output is found to be essentially insensitive to the defect considered. It is found that a simple feedback control algorithm in which the actuator input voltage is proportional to the transverse displacement of the sensor effectively annuls the vibrations of a neo-Hookean cantilever plate subjected to an impulsive load.

3.6 References

1. Hall, E.K. II and Muller, J.T., "Coupled vibration isolation/suppression system for space applications", *Aspects of structural design* (I. Chopra, ed.) SPIE, 2443, 1995, pp. 136-144

2. Dosch, J., Leo, D. and Inman, D.J., "Modeling and control for vibration suppression of a flexible smart structure", in *Dynamics and Control of Structures in Space II* (C.H. Kirk and P.C. Hughes, eds.) Computational Mechanics Publication, 1993, pp. 603-618

3. Won, C.C., Sulla, J.L., Sparks, D.W. Jr. and Belvin, W.K., "Application of piezoelectric device to vibration suppression",*J. of Guidance, Control, and Dynamics*, 17, 1994, pp. 1333-1338

4. Johnson, M.E. and Elliott, S.J., "Experiments on the active control of sound radiation using a volume velocity sensor", *Smart Structures and Integrated Systems*, (I. Chopra, ed.) SPIE, 2443, 1995, pp. 658-669

5. Price, J.G. and Napoletano, F.M., "Reducing interior acoustic field in vibrating cylinders", in *Smart Structures and Integrated Systems*, (I. Chopra, ed.), SPIE, 2443, 1995, pp. 682-691

6. Fuller, C.R., Hanson, C.H. and Snyder, S.D., " Active control of sound radiation from a vibrating rectangular panel by sound source and vibration inputs, an experimental comparison", *J. Sound and Vibration*, 145, 1991, pp. 195-215

7. Heeg, J., McGowan, A., Crawley, E. and Lin, C., "The piezoelectric aeroelastic response tailoring investigation: A status report", in *Industrial and Commerical Applications of Smart Structures Technologies*, SPIE, 2447, 1995, pp. 2-12

8. Song, O., Librescu, L. and Rogers, C.A., "Application of adaptive technology to static aeroelastic control of wing structures", *AIAA J*, 30, 1992, pp. 2882-2889

9. Ray, M.C.H., Rao, K.M. and Samanta, B., "Exact solution for static analysis of an intelligent structure under cylindrical bending", *Comput. Struct.*, 47, 1993, pp. 1031-1042

10. Lagoudas, D.C. and Bo, Z., "The cylindrical bending of composite plates with piezoelectric and SMA layers", *Smart Mater. Struct.*, 3, 1994, pp. 309-317

11. Brooks, S. and Heyliger, P., "Static behavior of piezoelectric laminates with distributed and patched actuators", *J. Intelligent Mater. Struct.*, 5, 1994, pp. 635-646

12. Srinivas, S., Rao, C.V.J. and Rao, A.K., " An exact analysis of vibration of simply supported homogeneous and laminated thick rectangular plates", *J. Sound Vib.*, 12, 1970, pp. 257-269

13. Wittrick, W.H., "Analytical, three-dimensional elasticity solutions to some plate problems, and some observations on Mindlin's plate theory", *Int. J. Solids Struct.*, 23, 1987, pp. 441-464

14. Zhou, Y.S. and Tiersten, H.F., "Elastic analysis of laminated composite plates in cylindrical bending due to piezoelectric actuators", *Smart. Mater. Struct.*, 3, 1994, pp. 225-265

15. Batra, R.C. and Liang, X.Q., "Shape control of vibrating simply supported rectangular plates", *AIAA J.*, 34, 1996, pp. 116-122

16. Hanagud, S., Obal, M.W. and Calise, A.J., "Optimal vibration control by the use of piezoceramic sensors and actuators", in *Proc. AIAA/ASME/AHS/ASEE 28th Structures, Structural Dynamics, and Materials Conference*, Paper #87-0959, Monterey, CA, April 6-8, 1987

17. Im, S. and Atluri, S.N., "Effects of a piezo-actuator on a finitely deformed beam subjected to general loading", *AIAA J.*, 27, 1989, pp. 1801-1807

18. Chandrashekhara, K. and Agarwal, A.N., "Active vibration control of laminated composite plates using piezoelectric devices: A finite element approach", *J. of Intelligent Material Systems and Structures*, 4, 1993, pp. 496-508

19. Batra, R.C. and Ghosh, K., "Deflection control during dynamic deformations of rectangular plate using piezoceramic elements", *AIAA J.*, 33, 1995, pp. 1547-1549

20. Samanta, B., Ray, M.C. and Bhattacharyya, R., "Finite element model for active control of intelligent structures", *AIAA J.*, 34, 1996, pp. 1885-1892

21. Suleman, A. and Venkayya, V.B., "A simple finite element formulation for a laminated composite plate with piezoelectric layers", *J. of Intelligent Material Systems and Structures*, 6, 1995, pp. 776-782

22. Tzou, H.S. and Gadre, M., "Theoretical analysis of a multi-layer thin shell coupled with piezoelectric shell actuators for distributed vibration controls", *J. Sound and Vibrations*, 132, 1989, pp. 433-450

23. Qiu, J.H. and Tani, J., "Vibration suppression of a cylindrical shell using a hybrid control method", *J. of Intelligent Material Systems and Structures*, 7, 1996, pp. 278-287

24. Allik, H. and Hughes, T.J.R., "Finite element method for piezoelectric vibration", *Int. J. for Numer. Method in Engr.*, 2, 1970, pp. 151-157

25. Mollenhauer, D.H. and Griffin, O.H. Jr., "Induced strain of actuation of surface bonded piezoceramic patches: A numerical and experimental study", *J. of Intelligent Material Systems and Structures*, 5, 1994, pp. 355-362

26. Tzou, H.S., Tseng, C.I. and Bahrami H., "A thin piezoelectric hexahedron finite element applied to design of smart continua", *Finite Elements in Analysis and Design*, 16, 1994, pp. 27-42

27. Hauch, R.M., "An industrial approach to static and dynamic finite element modeling of composite structures with embedded actuators", in *Smart Structures and Integrated Systems* (I. Chopra, ed.) SPIE, 2443, 1995, pp. 458-469

28. Wojicik, G.L., Vaughan, D.K., Abboud, N. and Mould, J. Jr., "Electromechanical modeling using explicit time-domain finite elements", in *Proc. of IEEE Ultrasonics Symposium*, 1993, pp. 1107-1112

29. Norwood, D.S., Shuart, M.J. and Herakovich, C.T., "Geometrically nonlinear analysis of interlaminar stress in unsymmetrically laminated plates subjected to inplane mechanical loading", in *Proc. AIAA/ASME/ASCE/AHS/ACS 32nd Structures, Structural Dynamics and Material Conference*, (AIAA, Washington, DC.), 1991, pp. 938-955

30. Kulkarni, G. and Hanagud, S., "Modeling issue in the vibration control with piezoceramic actuators", *Smart Structures and Materials*, (G.K. Haritos and A.V. Srinivasan, eds.) ASME, AD-24/AMD-123, 1991, pp. 7-45

31. Pai, P.F., Nayfeh, A.H., and Oh, K., "A nonlinear theory of laminated piezoelectric plates", in *Proceedings of 33rd AIAA/ASME/ASCE/AHS/ASC Structures, Structural Dynamics and Materials Conference*, (AIAA, Washington, DC), AIAA-92-2407-CP, 1992, pp. 577-585

32. Maugin, G.A., Pouget, J., Drouot, R., and Collect, B., "Nonlinear Electromechanical Coupling", John Willey and Sons, 1992

33. Tiersten, H.F., "On the nonlinear equations of thermoelectroelasticity", *Int. J. Eng. Sci.*, 9, 1971, pp. 587-604

34. Tiersten, H.F., "Nonlinear electroelastic equations cubic in small field variables", *J. Acoust. Soc. Am.*, 57, 1975, pp. 660-666

35. Yang, J.S. and Batra, R.C., "A second order theory for piezoelectric materials", *J. Accoust. Soc. Am.*, 97, 1995, pp. 280-288

36. Huang, Y.N. and Batra, R.C., "A theory of thermoviscoelastic dielectrics", *J. Thermal Stresses*, 19, 1996, pp. 419-430

37. Crawley, E.F. and Anderson, E.H., "Detailed models of piezoceramic actuation of beams", *J. Intell. Mater. Struct.*, 1, 1990, pp. 4-24

38. Tiersten, H.F., "Electroelastic equations for electroded thin plates subjected to large driving voltages", *J. Appl. Phys.*, 74, 1993, pp. 3389-3393

39. Moetakef, M.A., Joshi, S.P., and Lawrence, K.L., "Elastic wave generation by piezoceramic patches", *AIAA J.*, 34, 1996, pp.2110-2117

40. Hughes, T.J.R., "The finite element method, linear static and dynamic finite element analysis", Prentice-Hall, Englewood, NJ, 1987

41. ABAQUS User's Manual, Hibbitt, Karlsson and Sorensen, Inc., Version 5.2 (1992)

42. Ha, S.K., Keilers, C., and Chang, F.K., "Finite element analysis of composite structures containing distributed piezoceramic sensors and actuators", *AIAA J.*, 30, 1992, pp.772-780

43. Bathe, K.J., "Finite element procedures in engineering analysis", Prentice-Hall, Inc., Englewood Cliffs, NJ, 1982

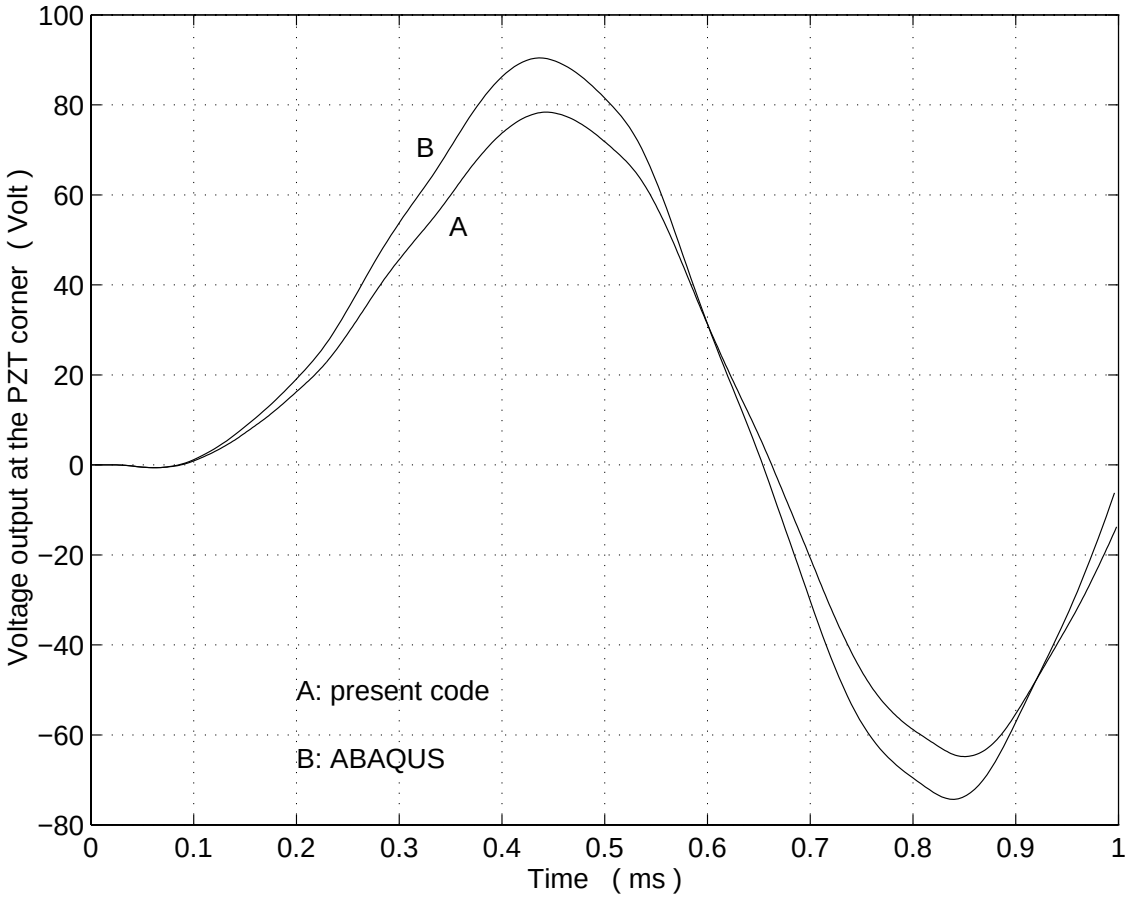

Figure 3.1: A comparison of the time histories of the voltage output at the top right corner of the PZT patch, as computed by ABAQUS and the present code

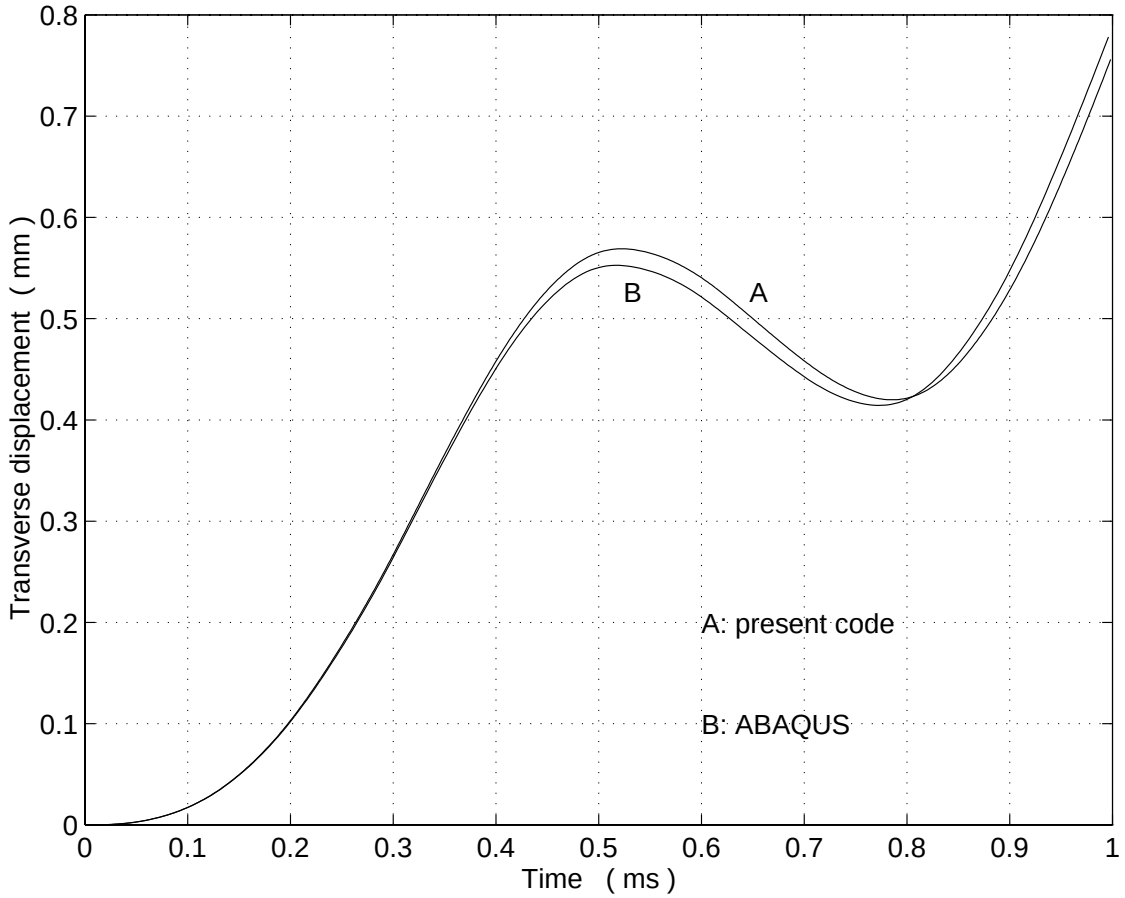

Figure 3.2: A comparison of the time histories of the transverse displacement under the point load applied to a composite plate, as computed by ABAQUS and the present code

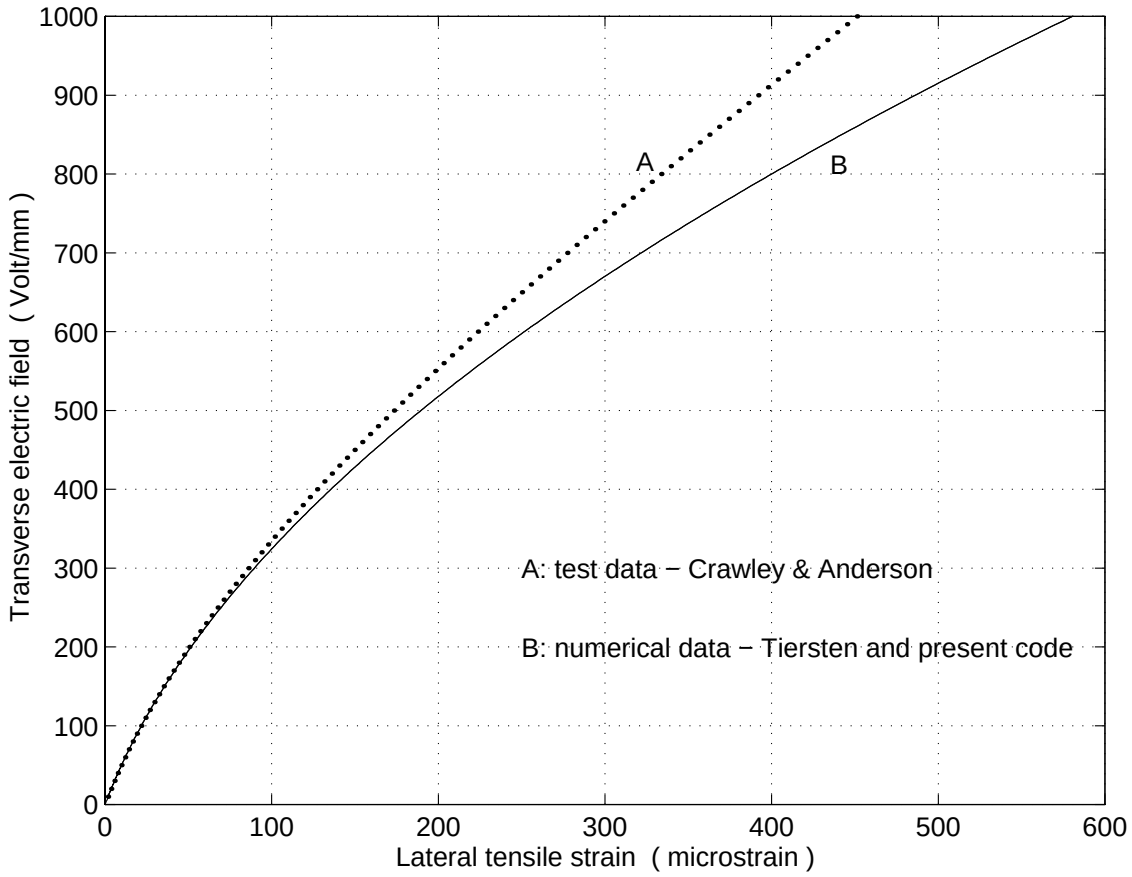

Figure 3.3: A comparison of Crawley and Anderson's test data and Tiersten's results of the lateral tensile strain at the centroid of the PZT-plate vs. the transverse electric field with that computed using the present code

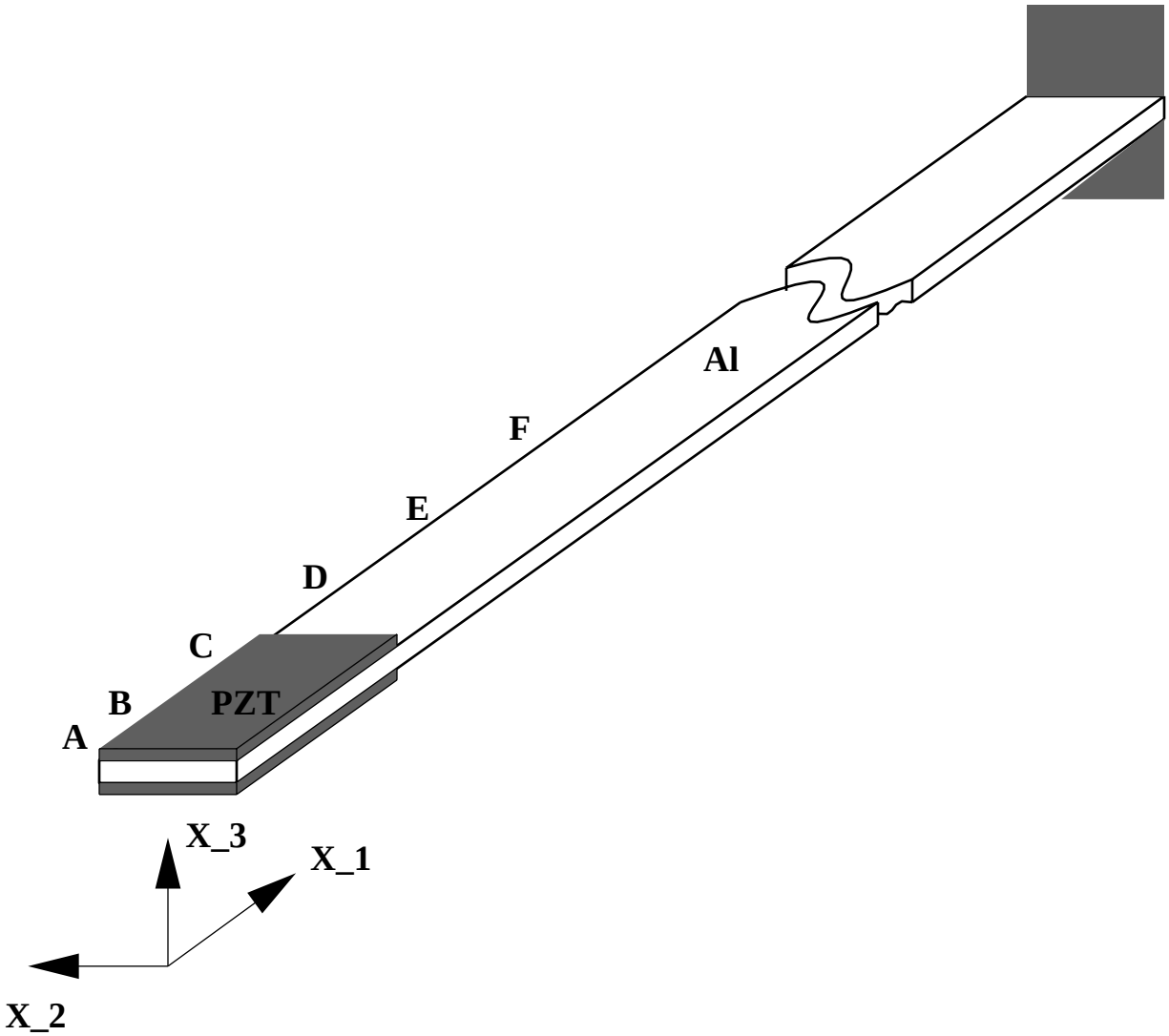

Figure 3.4: A sketch of the setup of Moetakef et al.'s experiment on wave propagation in a cantilever aluminum beam (not to scale)

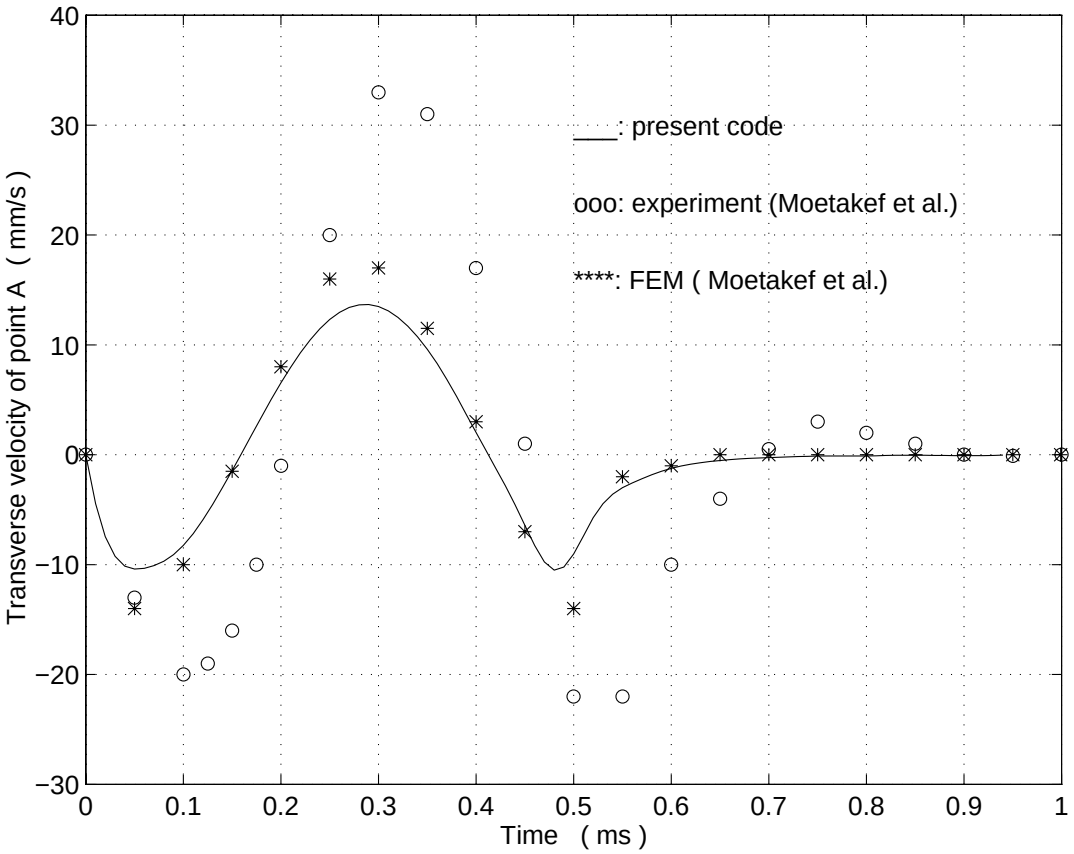

Figure 3.5: A comparison of the test data of Moetakef et al. and their computed results of the time history of the transverse velocity of point A on a cantilever beam actuated by two PZT patches bonded near its free edge with the corresponding result computed by using the present code.

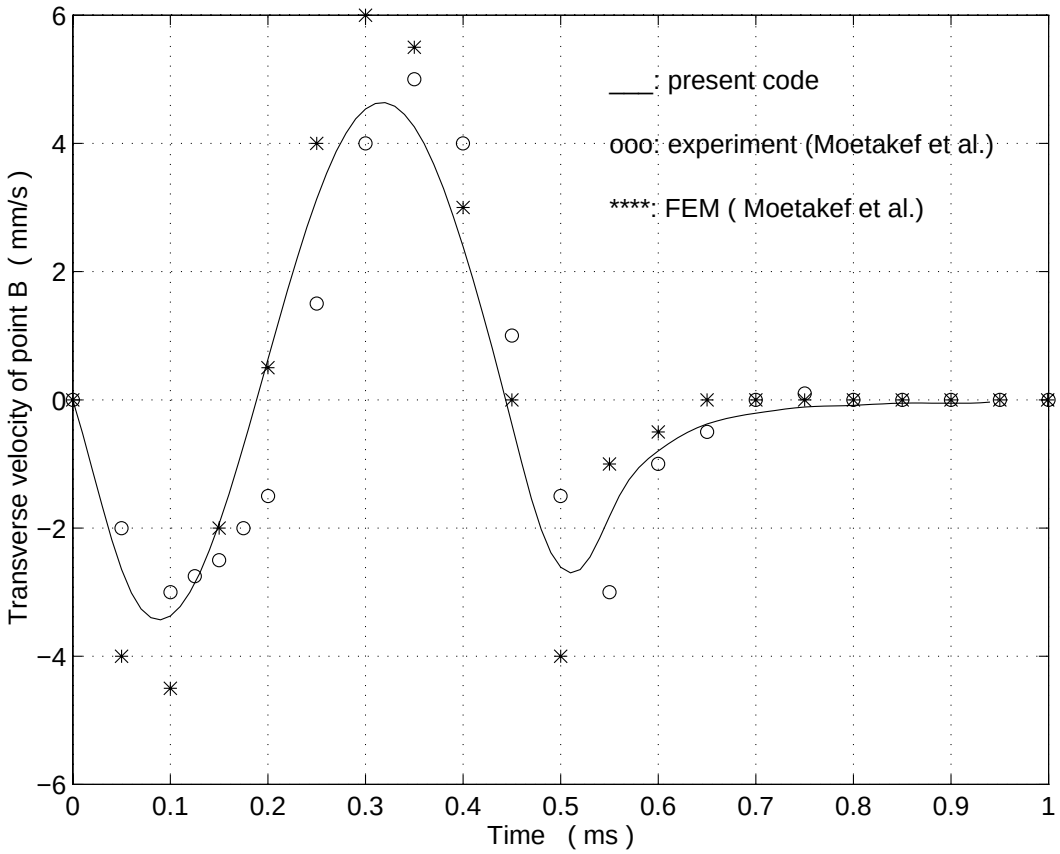

Figure 3.6: A comparison of the test data of Moetakef et al. and their computed results of the time history of the transverse velocity of point B on a cantilever beam actuated by two PZT patches bonded near its free edge with the corresponding result computed by using the present code.

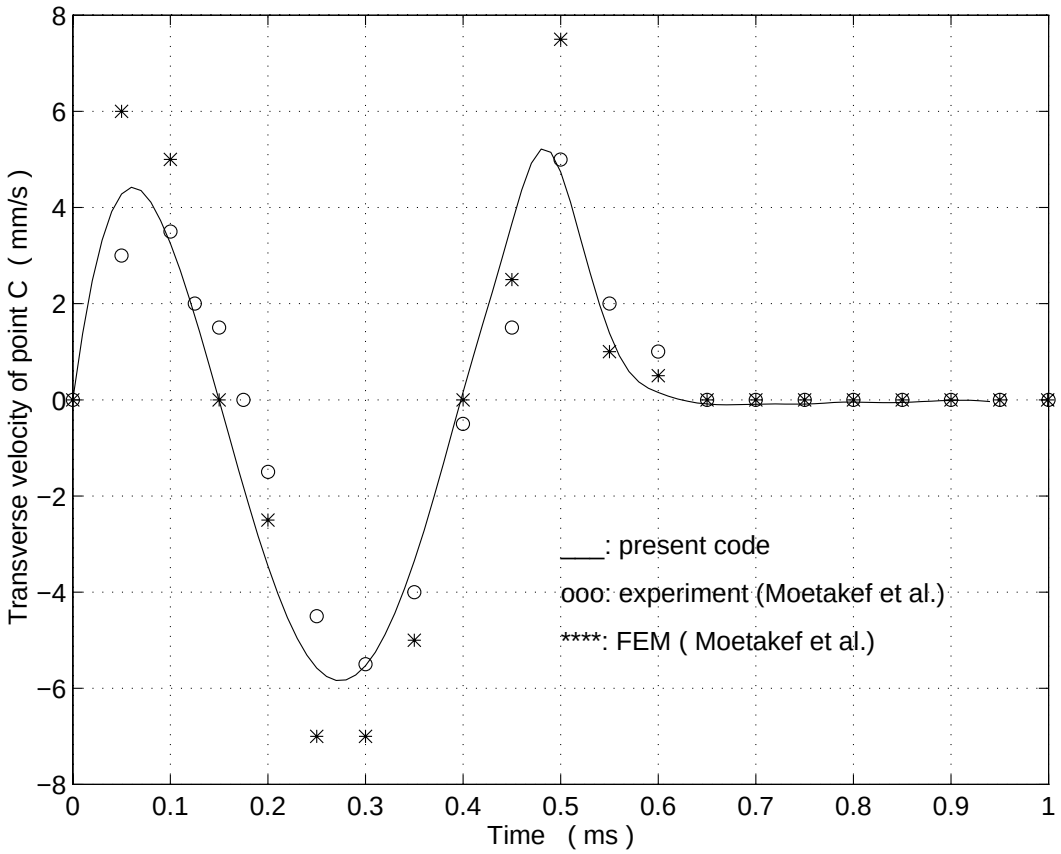

Figure 3.7: A comparison of the test data of Moetakef et al. and their computed results of the time history of the transverse velocity of point C on a cantilever beam actuated by two PZT patches bonded near its free edge with the corresponding result computed by using the present code.

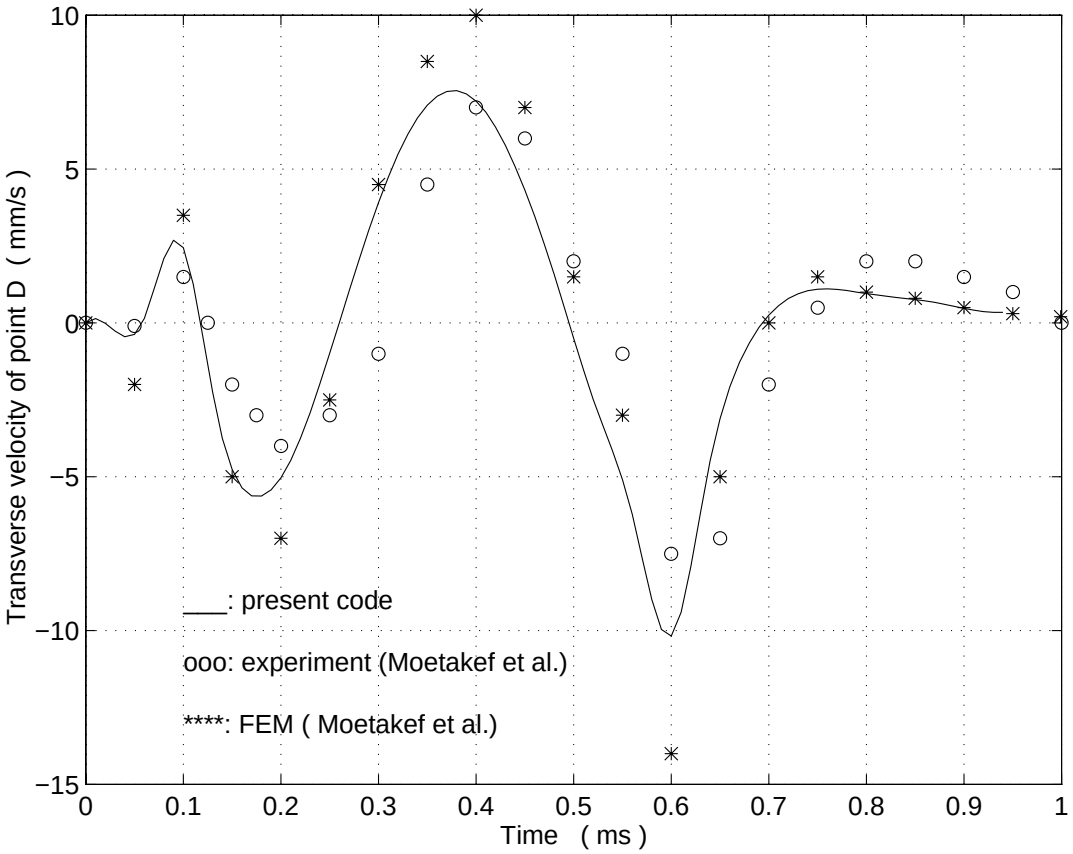

Figure 3.8: A comparison of the test data of Moetakef et al. and their computed results of the time history of the transverse velocity of point D on a cantilever beam actuated by two PZT patches bonded near its free edge with the corresponding result computed by using the present code.

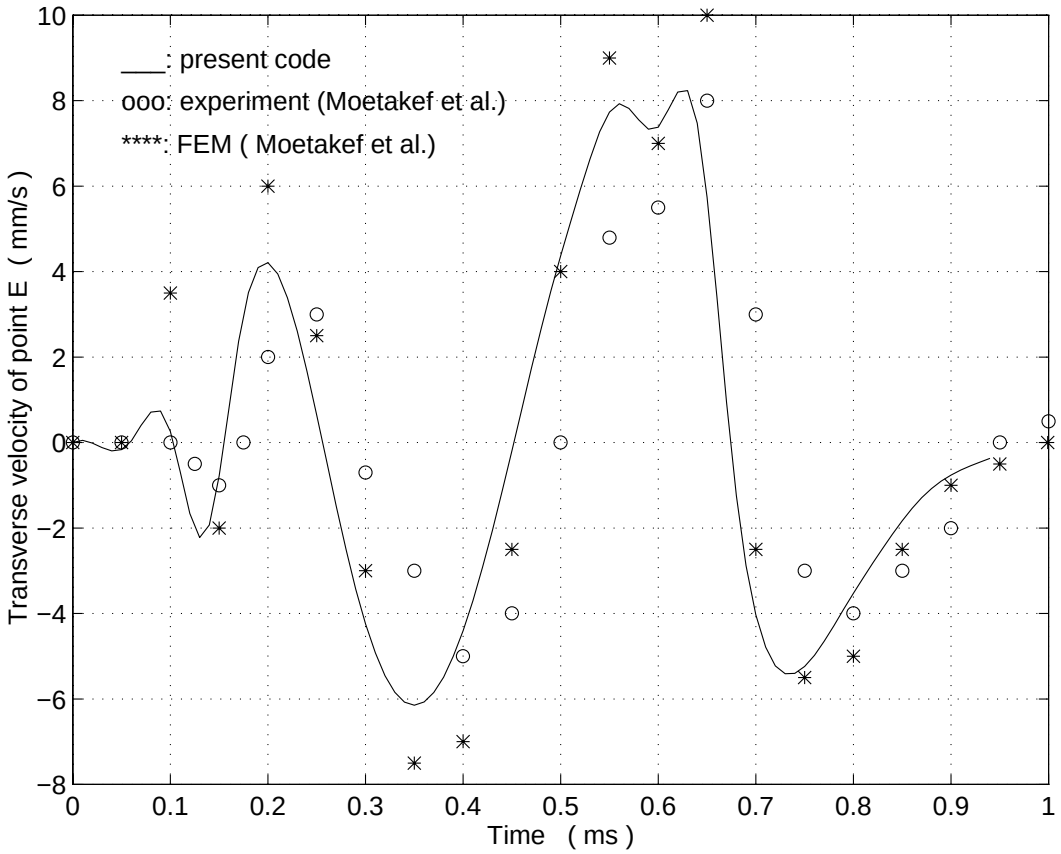

Figure 3.9: A comparison of the test data of Moetakef et al. and their computed results of the time history of the transverse velocity of point E on a cantilever beam actuated by two PZT patches bonded near its free edge with the corresponding result computed by using the present code.

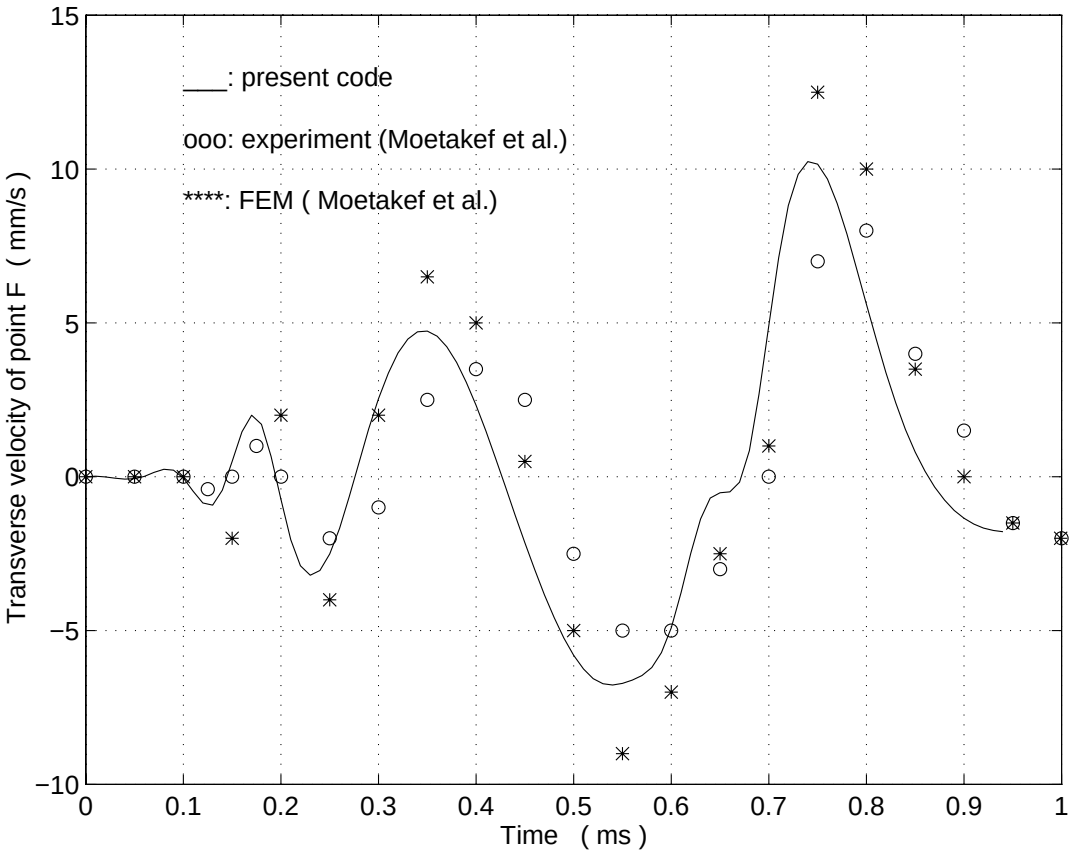

Figure 3.10: A comparison of the test data of Moetakef et al. and their computed results of the time history of the transverse velocity of point F on a cantilever beam actuated by two PZT patches bonded near its free edge with the corresponding result computed by using the present code.

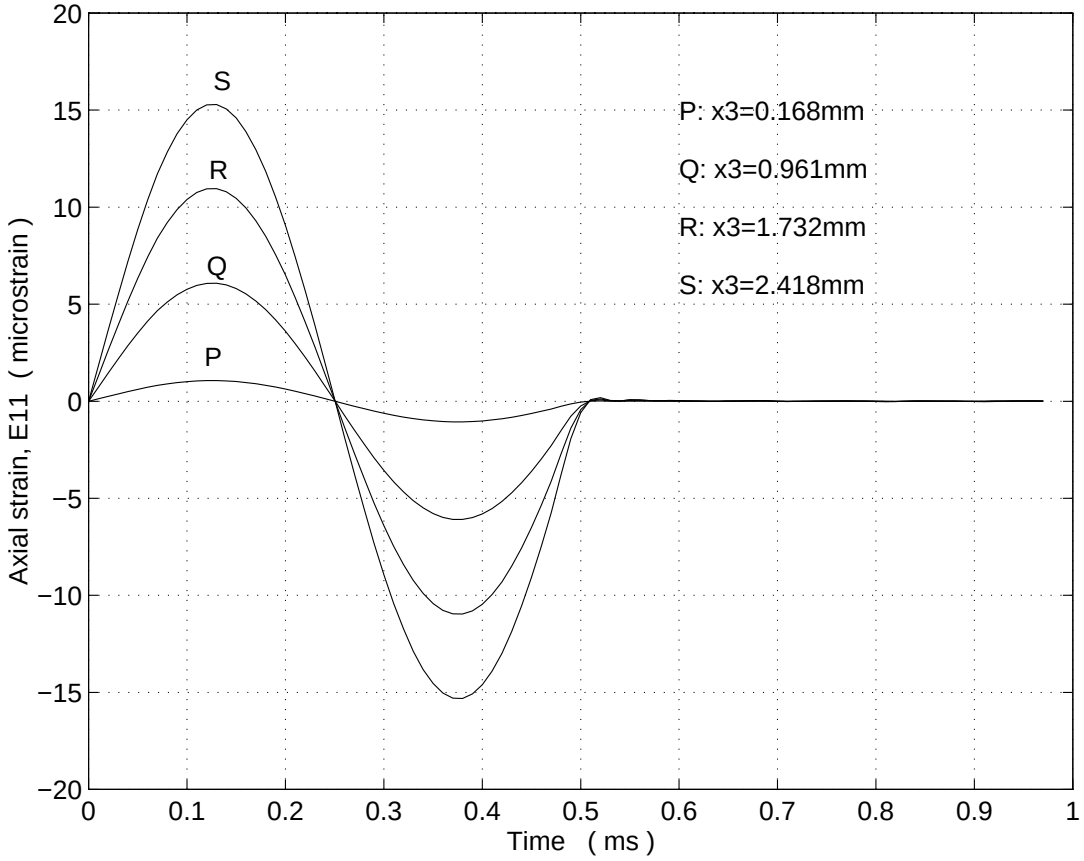

Figure 3.11: Time histories of the axial strain at four points on a vertical line in Moetakef et al.'s experiment on flexural vibrations of a beam.

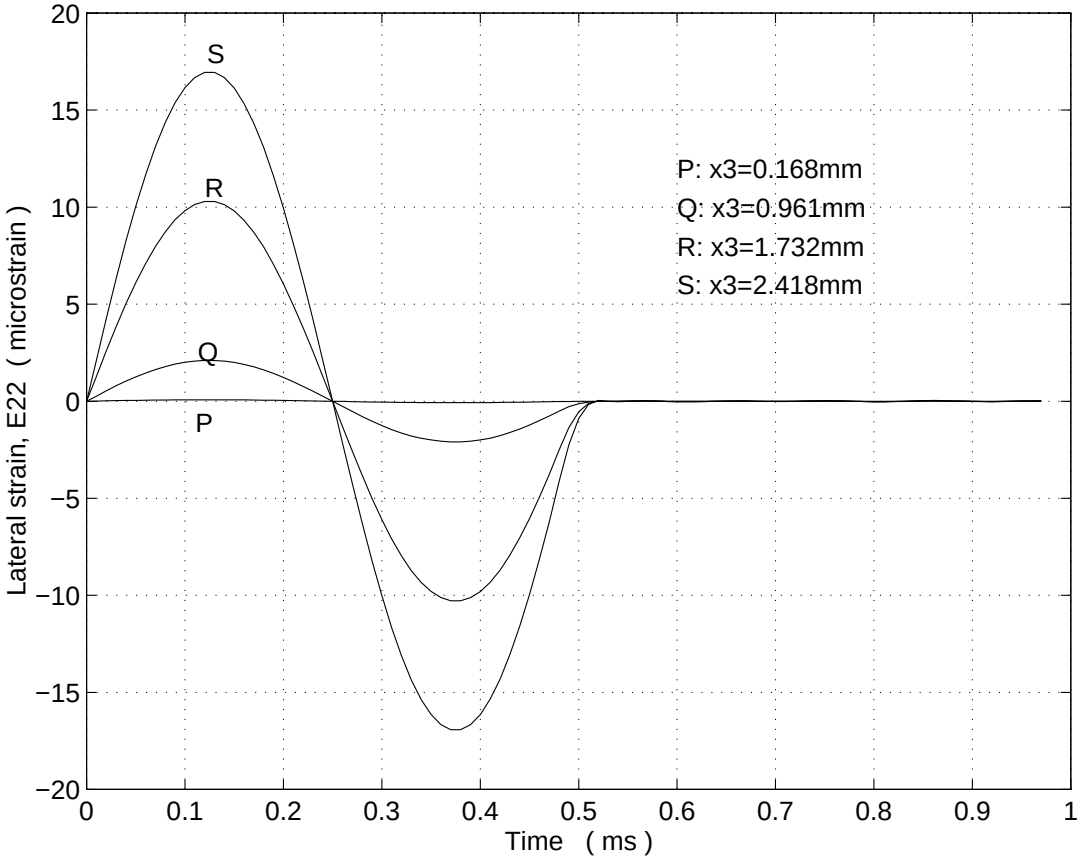

Figure 3.12: Time histories of the lateral strain at four points on a vertical line in Moetakef et al.'s experiment on flexural vibrations of a beam.

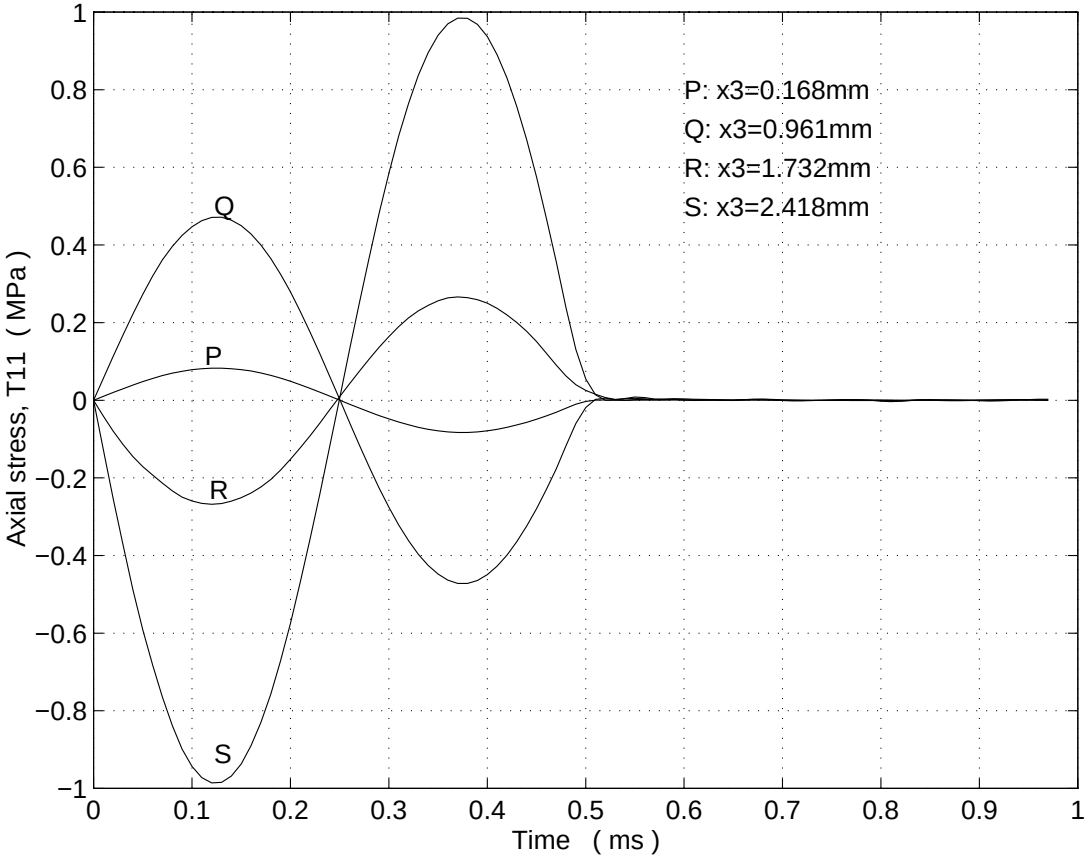

Figure 3.13: Time histories of the axial stress at four points on a vertical line in Moetakef et al.'s experiment on flexural vibrations of a beam.

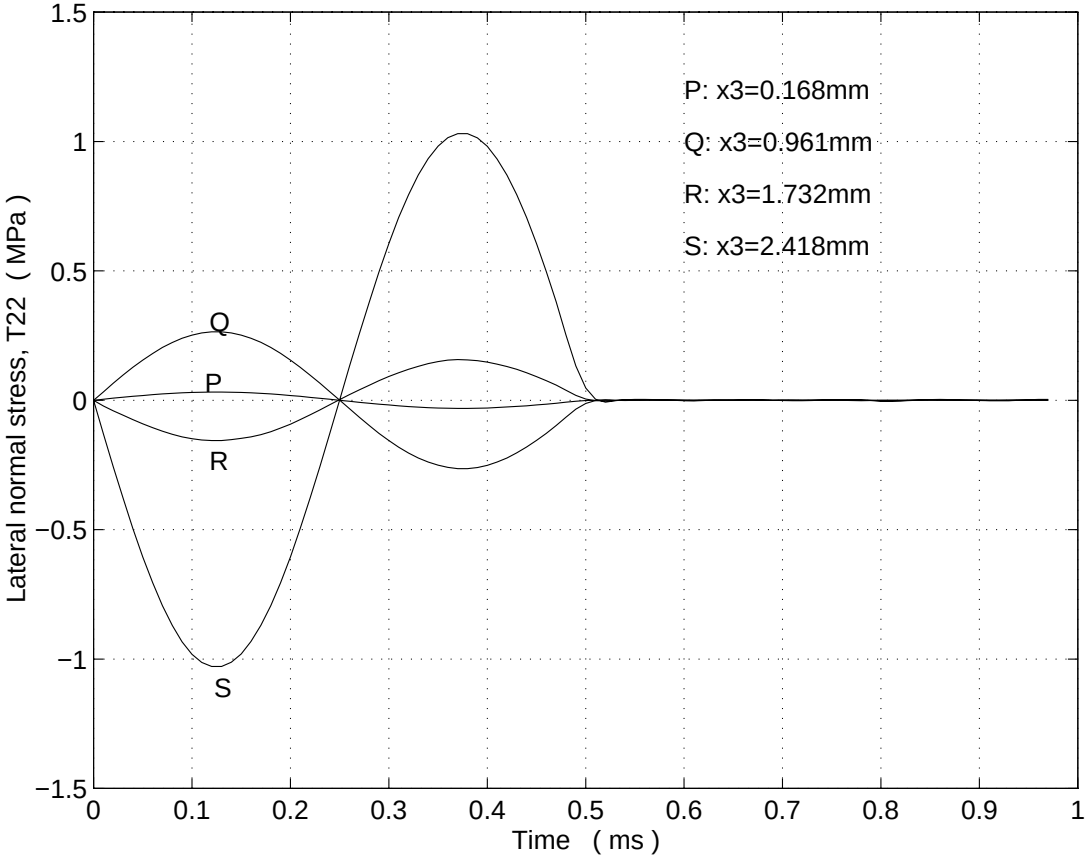

Figure 3.14: Time histories of the lateral stress at four points on a vertical line in Moetakef et al.'s experiment on flexural vibrations of a beam.

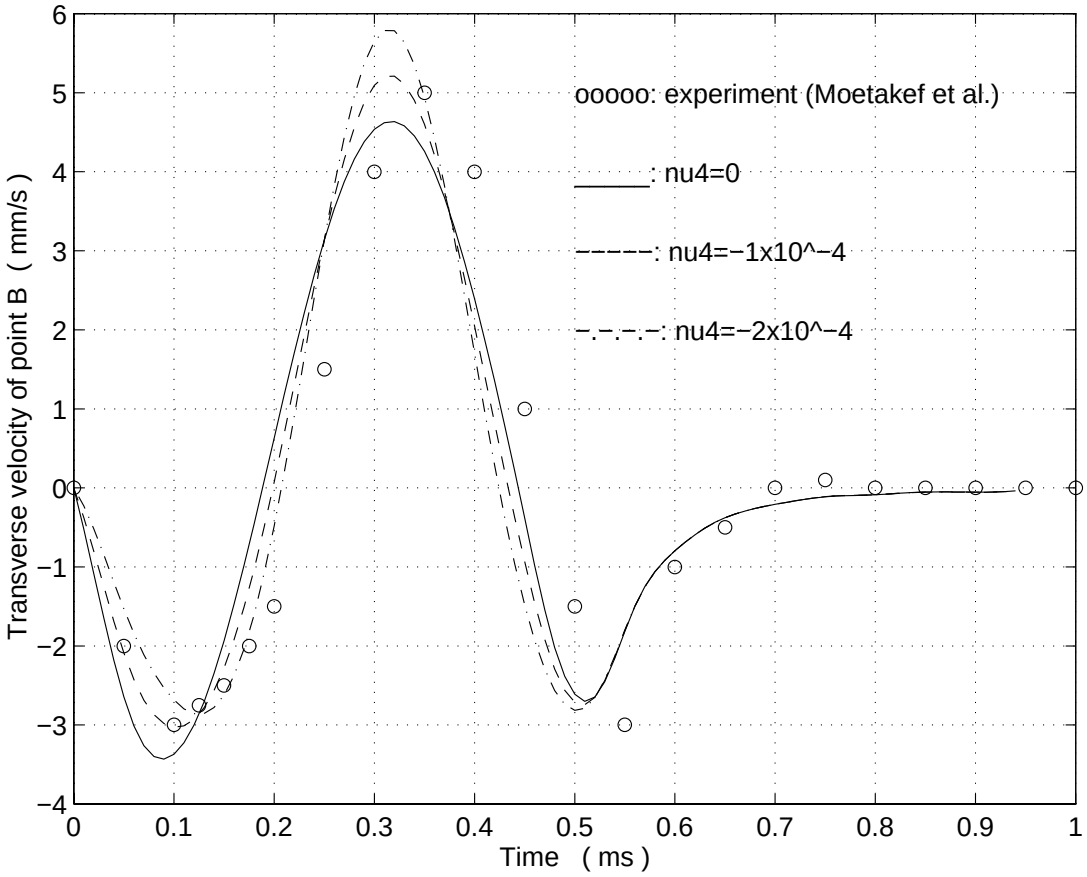

Figure 3.15: Time history of the transverse velocity of point B for three different values of ν_4 with $\nu_{12} = 0$.

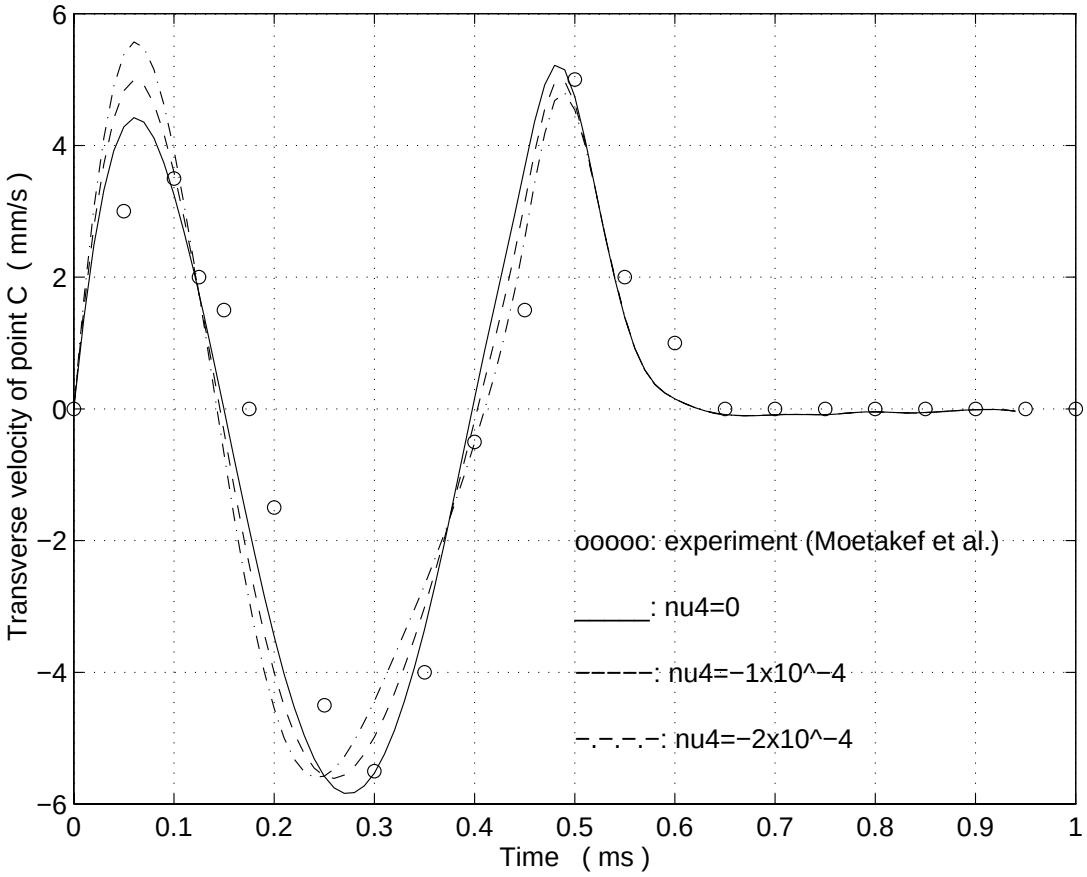

Figure 3.16: Time history of the transverse velocity of point C for three different values of ν_4 with $\nu_{12} = 0$.

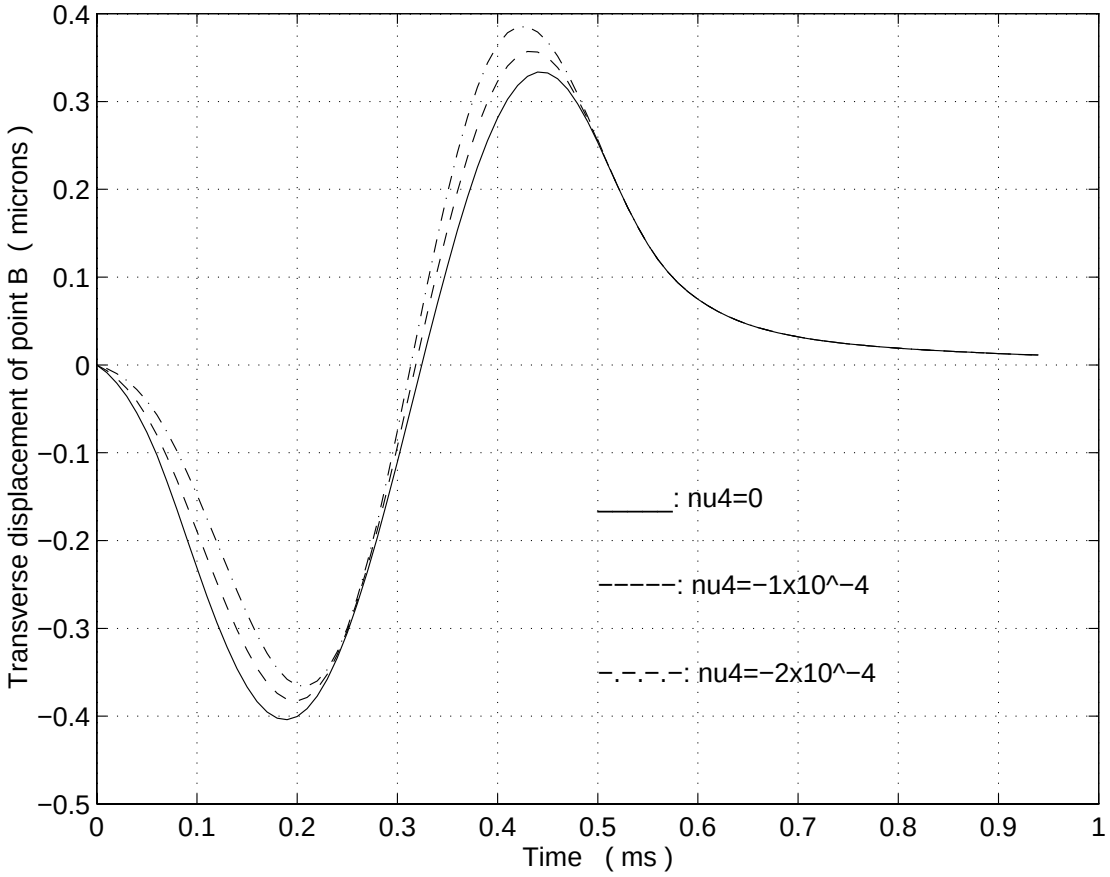

Figure 3.17: Time history of the transverse displacement of point B for three different values of ν_4 with $\nu_{12} = 0$.

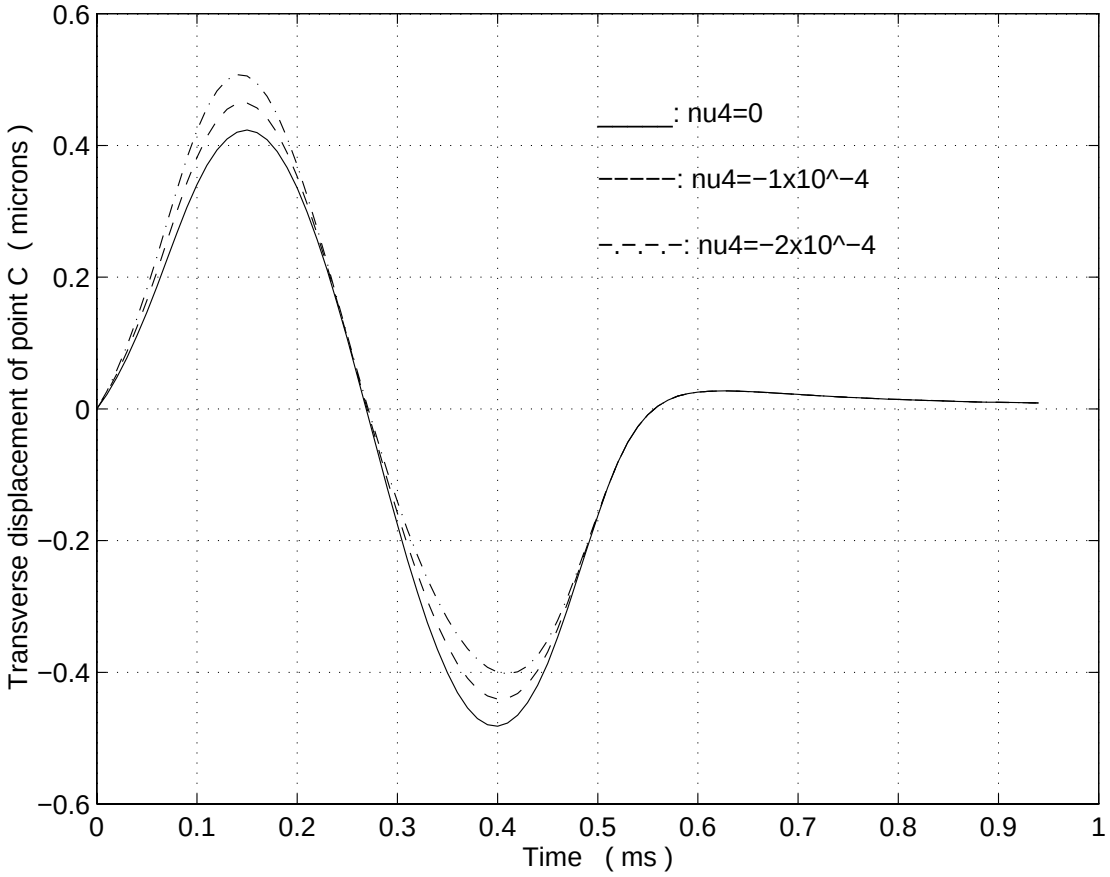

Figure 3.18: Time history of the transverse displacement of point C for three different values of ν_4 with $\nu_{12} = 0$.

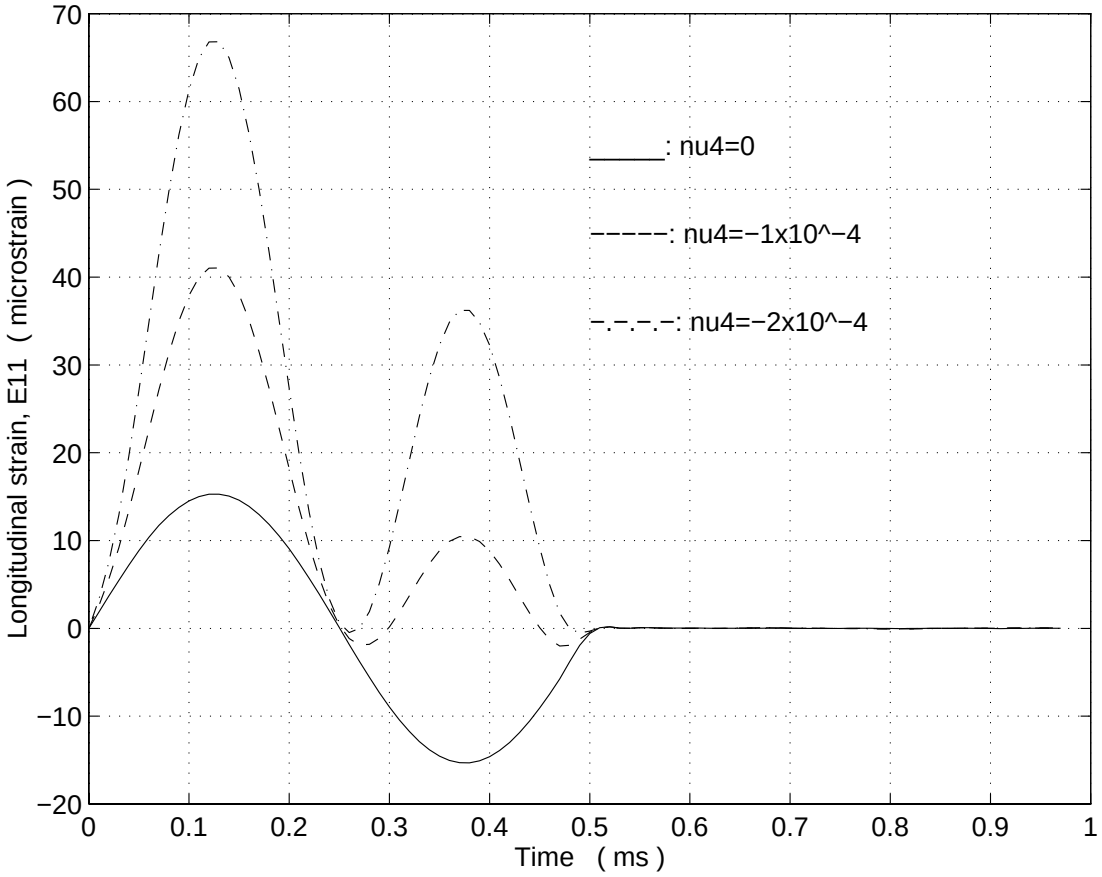

Figure 3.19: Time history of the axial strain at the point (6.685, 0.335, 2.418) mm in the PZT for three different values of ν_4 with $\nu_{12} = 0$.

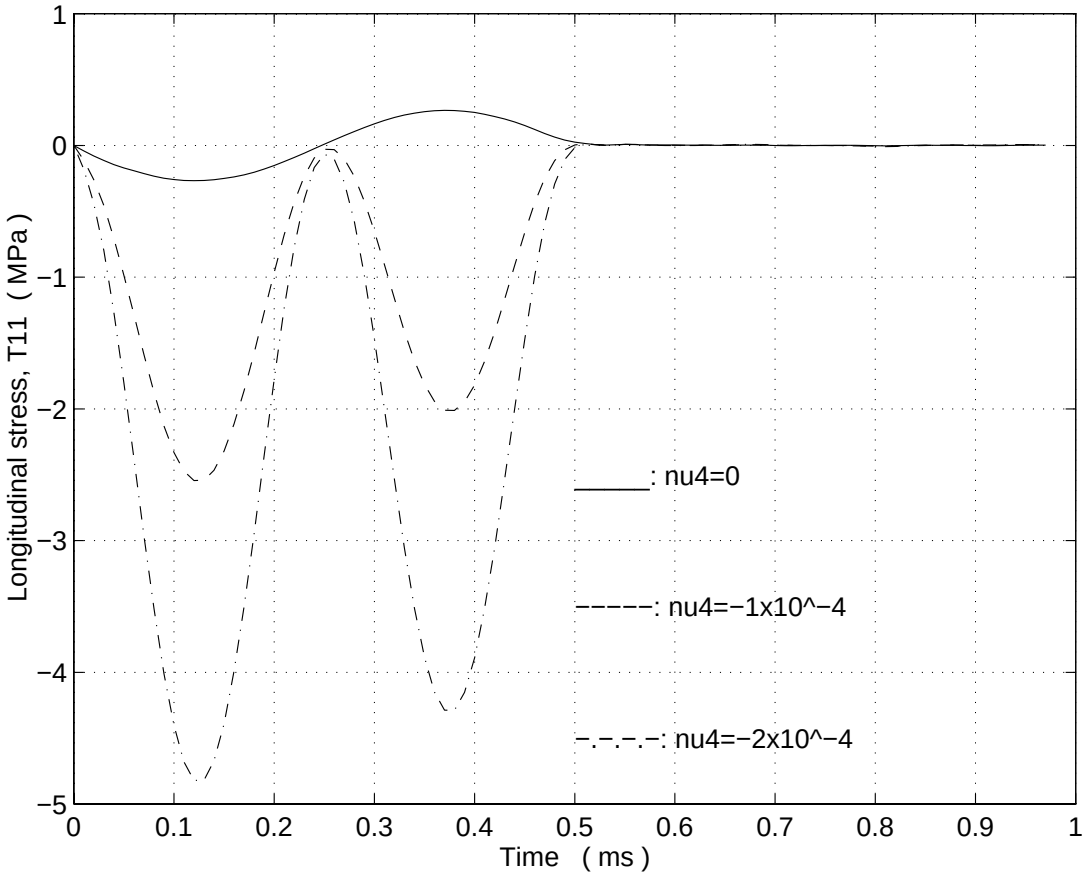

Figure 3.20: Time history of the axial stress at the point (6.685, 0.335, 2.418) mm in the PZT for three different values of ν_4 with $\nu_{12} = 0$.

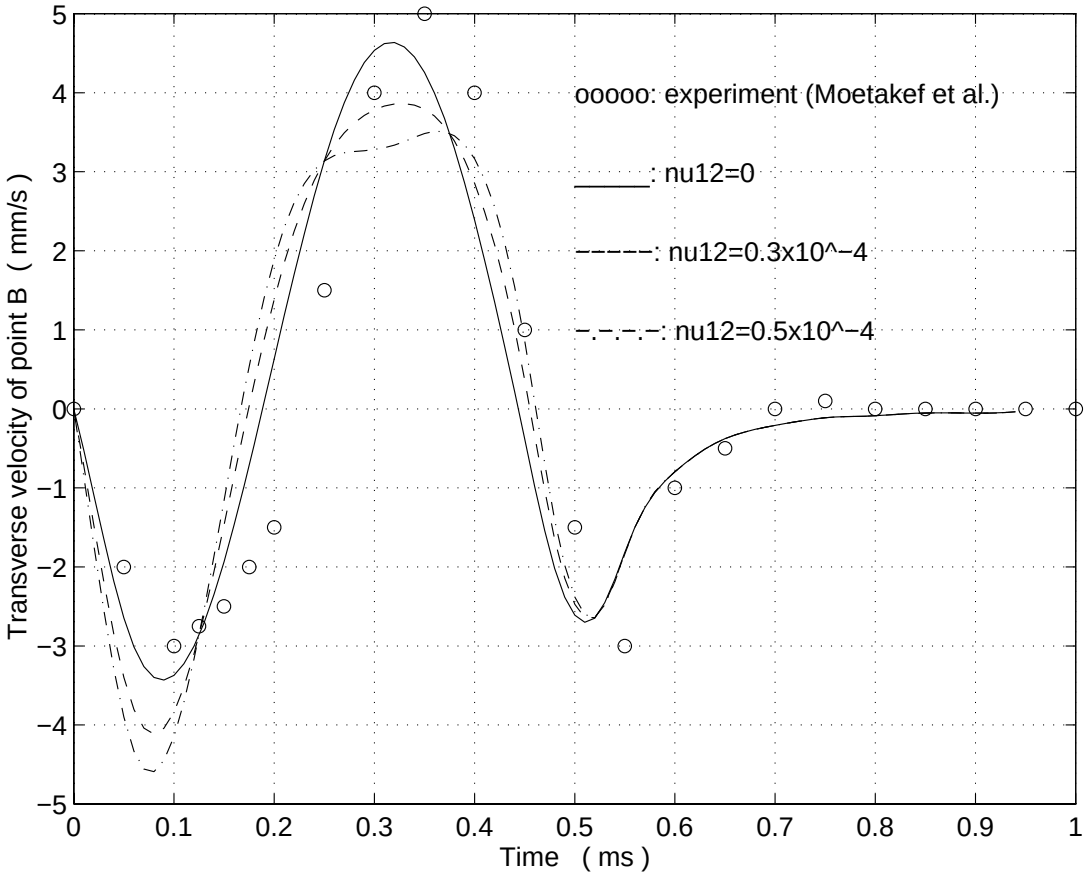

Figure 3.21: Time history of the transverse velocity of point B for three different values of ν_{12} with $\nu_4 = 0$.

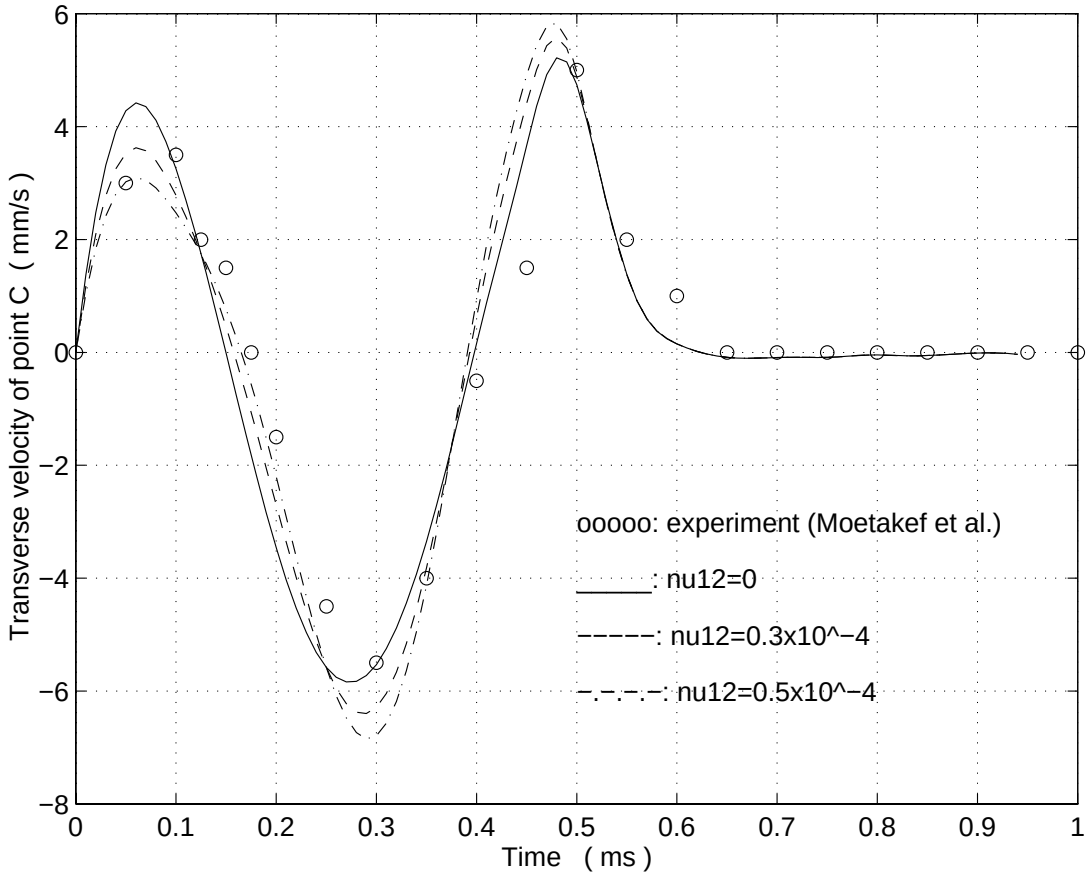

Figure 3.22: Time history of the transverse velocity of point C for three different values of ν_{12} with $\nu_4 = 0$.

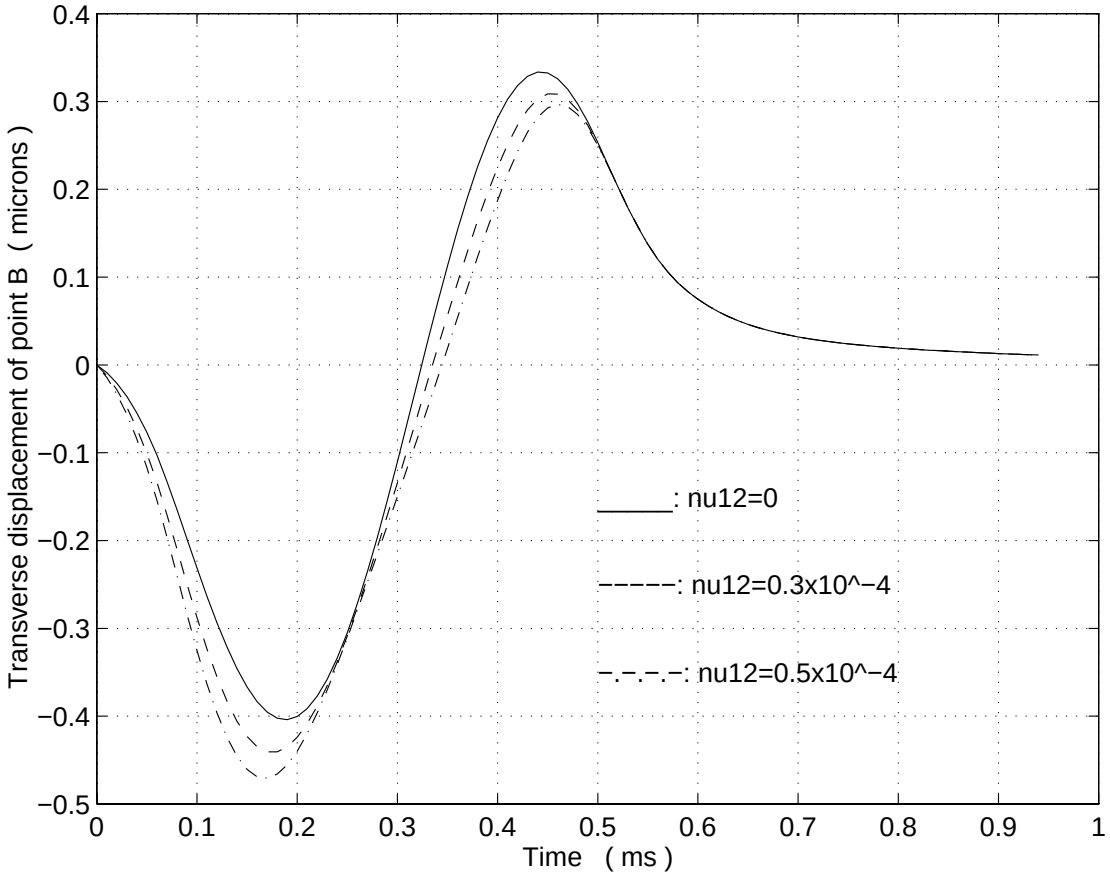

Figure 3.23: Time history of the transverse displacement of point B for three different values of ν_{12} with $\nu_4 = 0$.

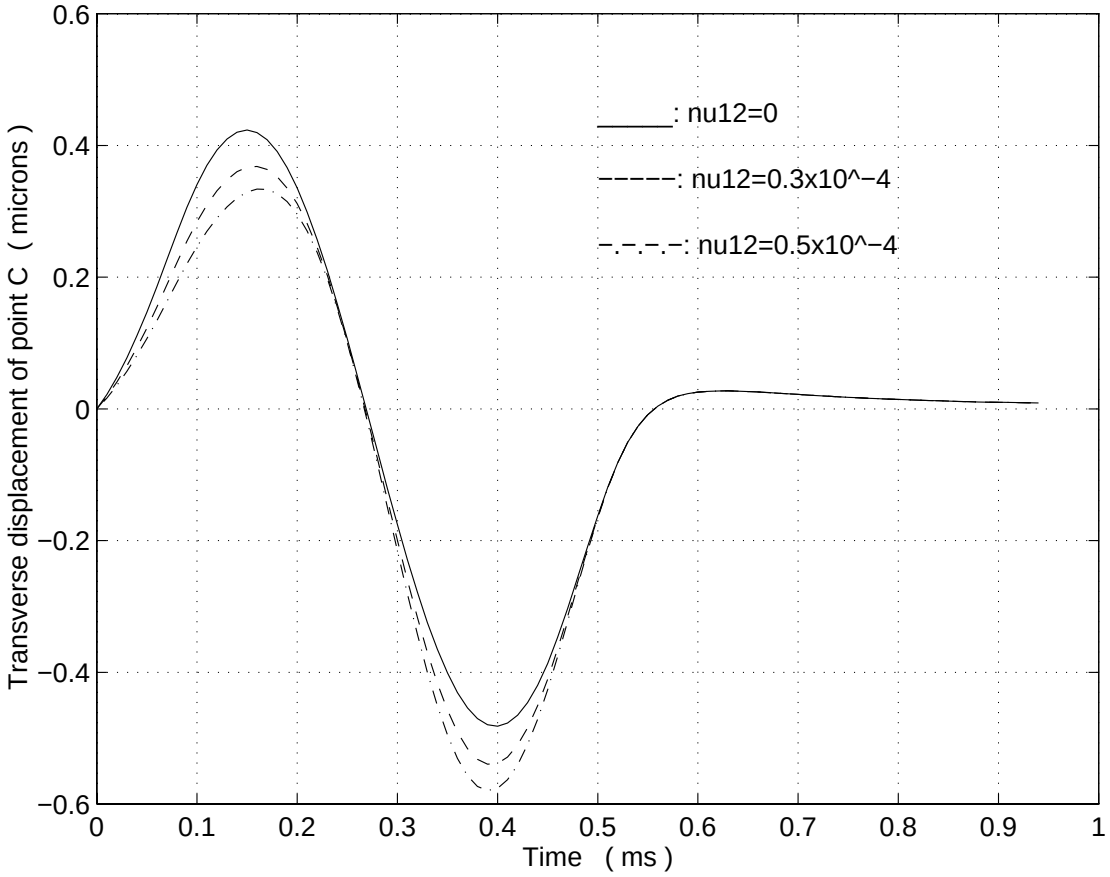

Figure 3.24: Time history of the transverse displacement of point C for three different values of ν_{12} with $\nu_4 = 0$.

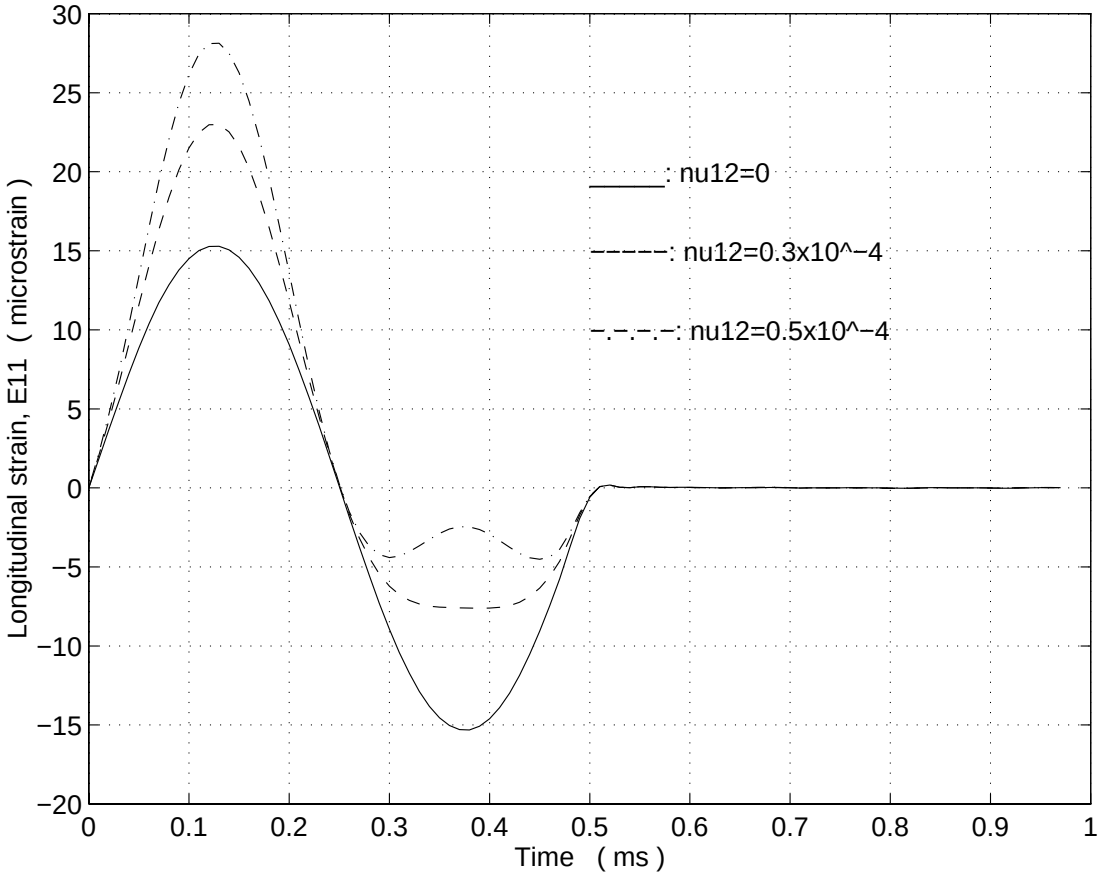

Figure 3.25: Time history of the axial strain at the point (6.685, 0.335, 2.418) mm in the PZT for three different values of ν_{12} with $\nu_4 = 0$.

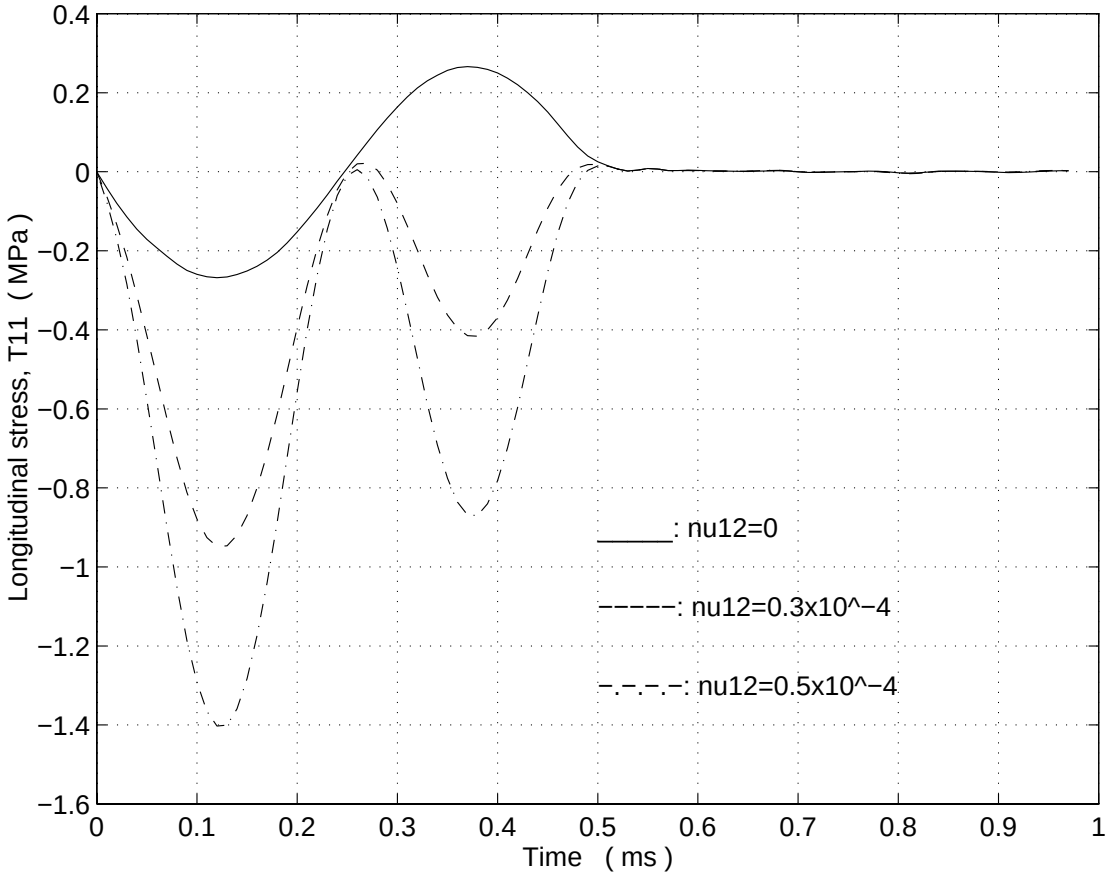

Figure 3.26: Time history of the axial stress at the point (6.685, 0.335, 2.418) mm in the PZT for three different values of ν_{12} with $\nu_4 = 0$.

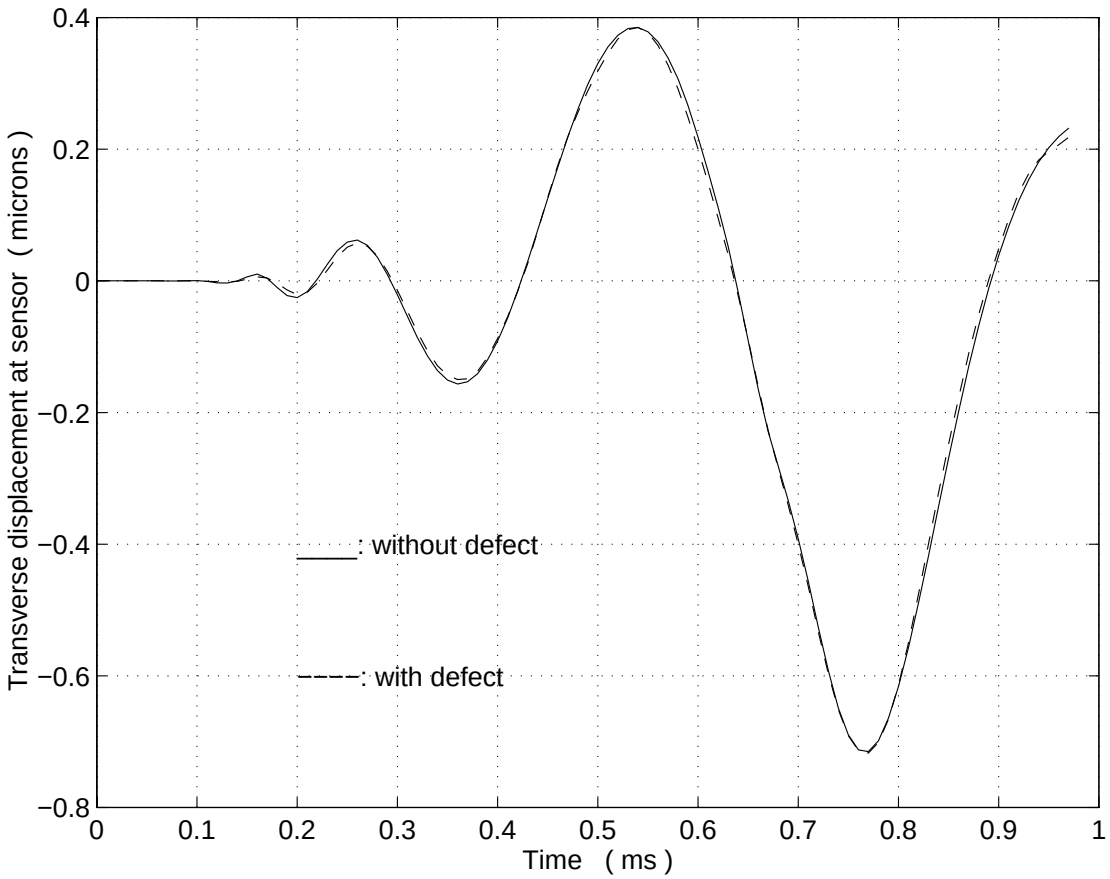

Figure 3.27: Time history of the transverse displacement of the top right corner of the sensor on the cantilever beam, used in Moetakef et al.'s experiment, with and without a defect in it.

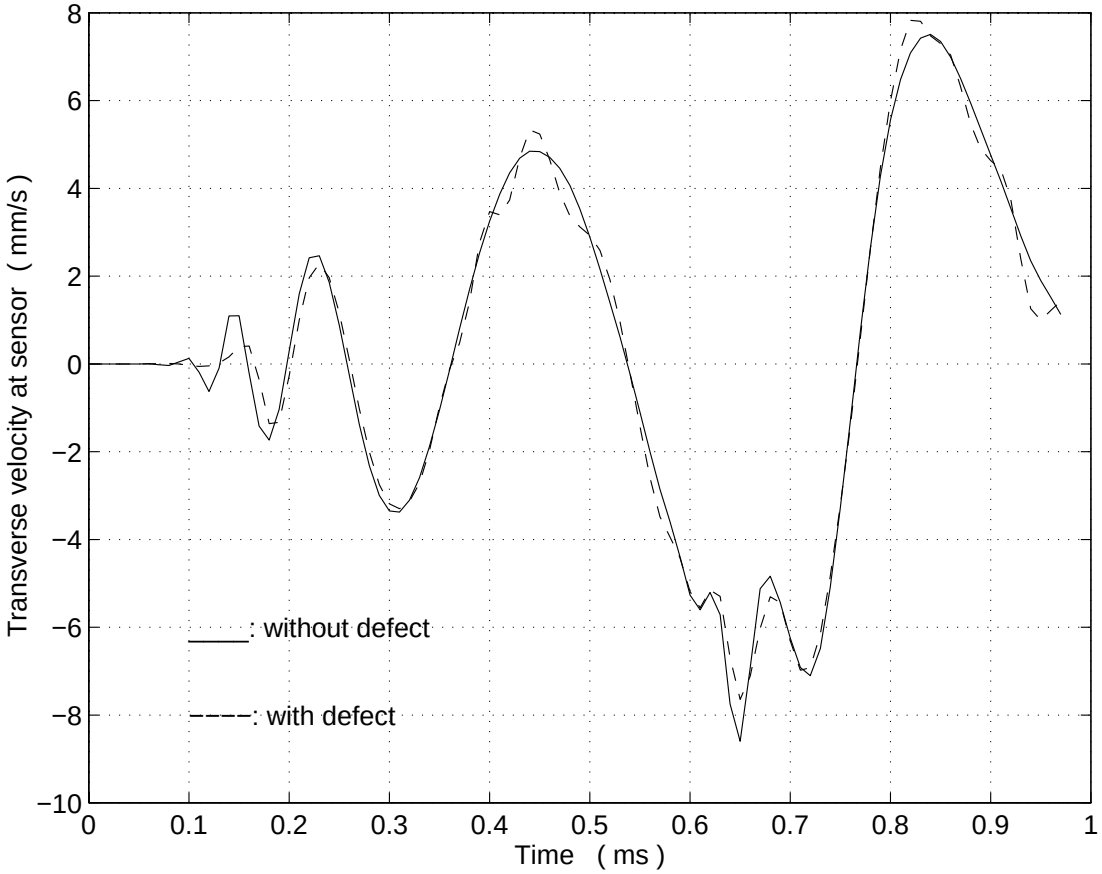

Figure 3.28: Time history of the transverse velocity of the top right corner of the sensor on the cantilever beam, used in Moetakef et al.'s experiment, with and without a defect in it.

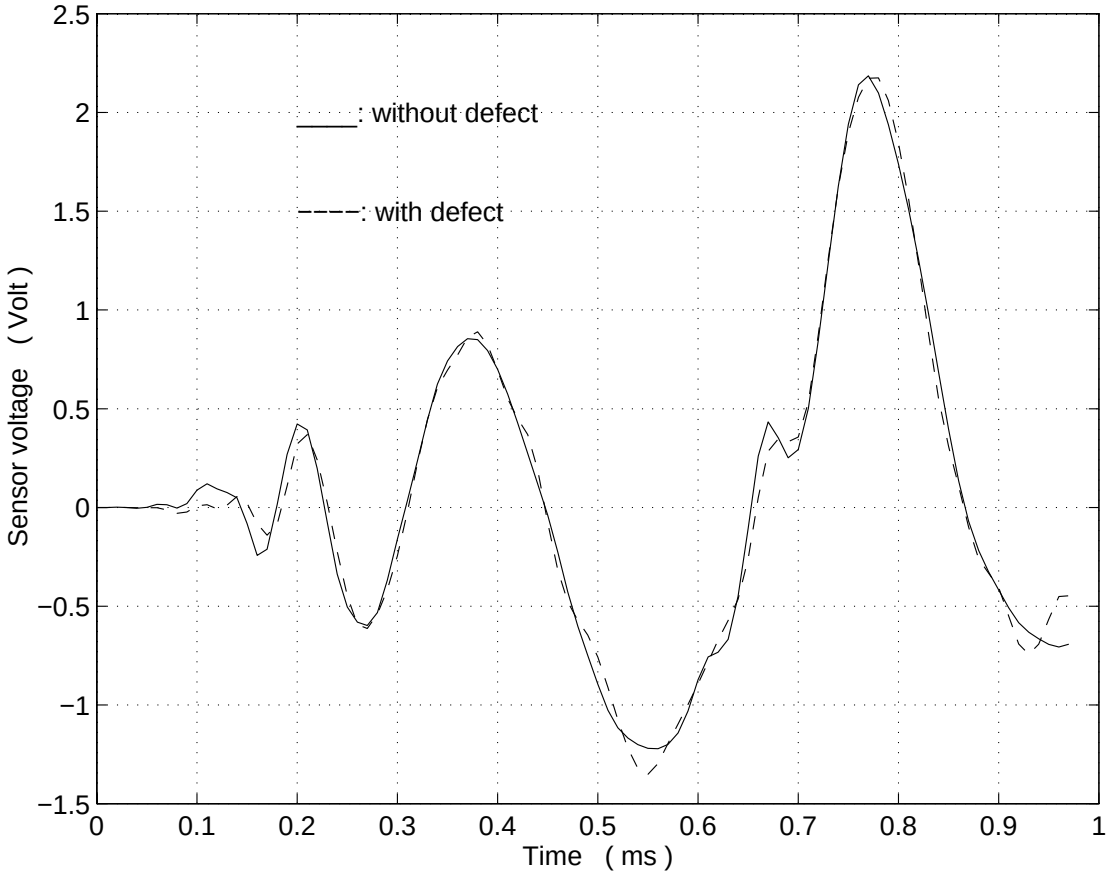

Figure 3.29: Time history of the sensor voltage in Moetakef et al.'s experiment, with and without a defect in the cantilever beam.

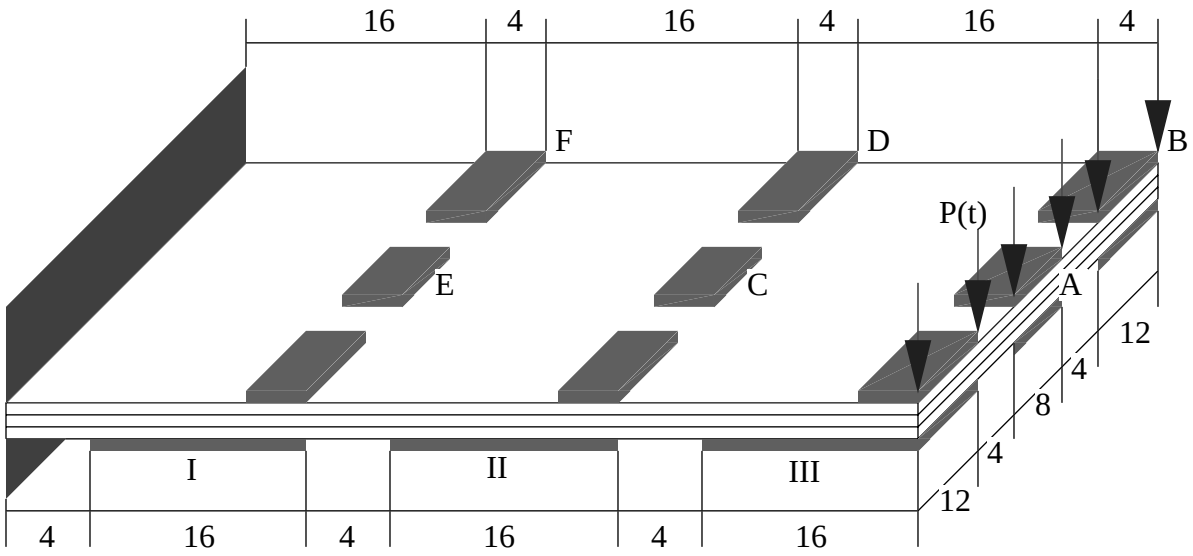

Figure 3.30: A set up of the smart plate (all dimensions are in mm)

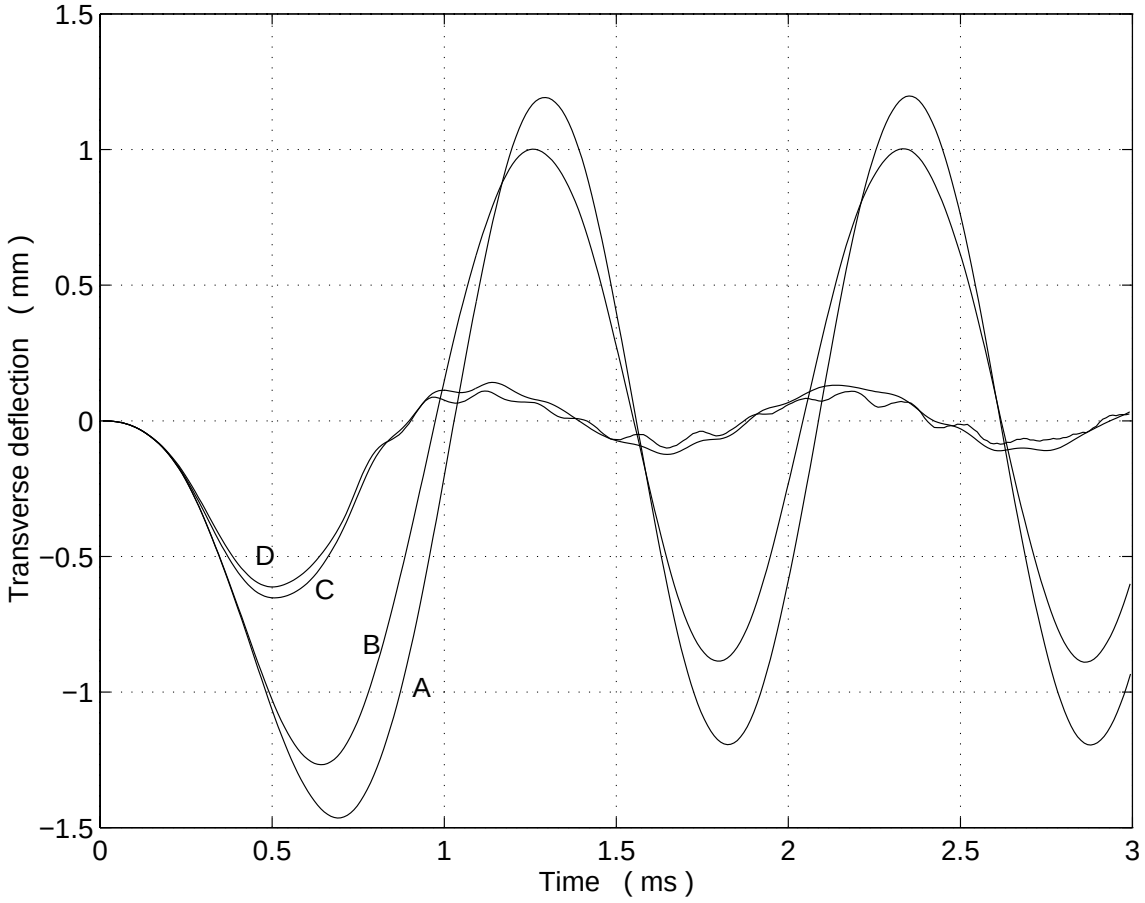

Figure 3.31: Time histories of the transverse displacements of point A when (A) the plate is uncontrolled; (B) sensors/actuators in column I are activated; (C) sensors/actuators in columns I and II are activated; and (D) all sensors/actuators are activated.

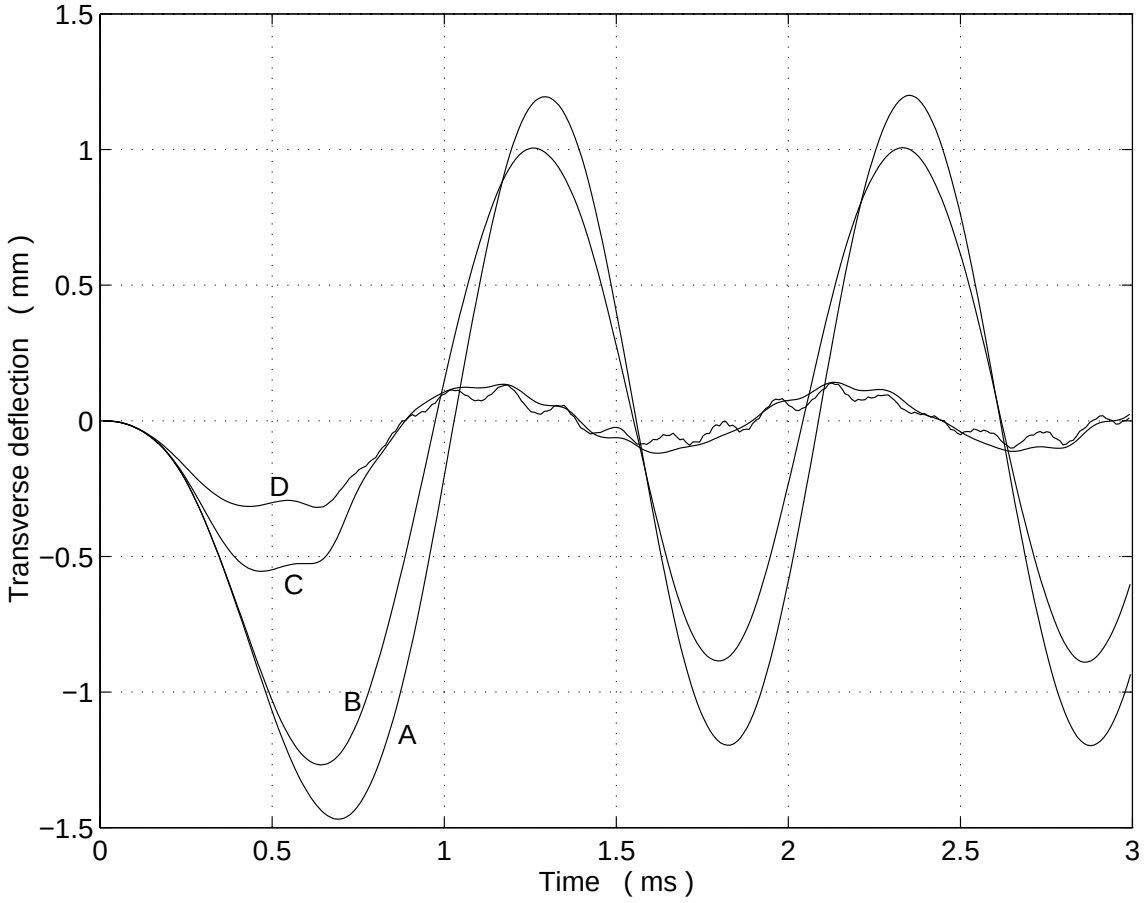

Figure 3.32: Time histories of the transverse displacements of point B when (A) the plate is uncontrolled; (B) sensors/actuators in column I are activated; (C) sensors/actuators in columns I and II are activated; and (D) all sensors/actuators are activated.

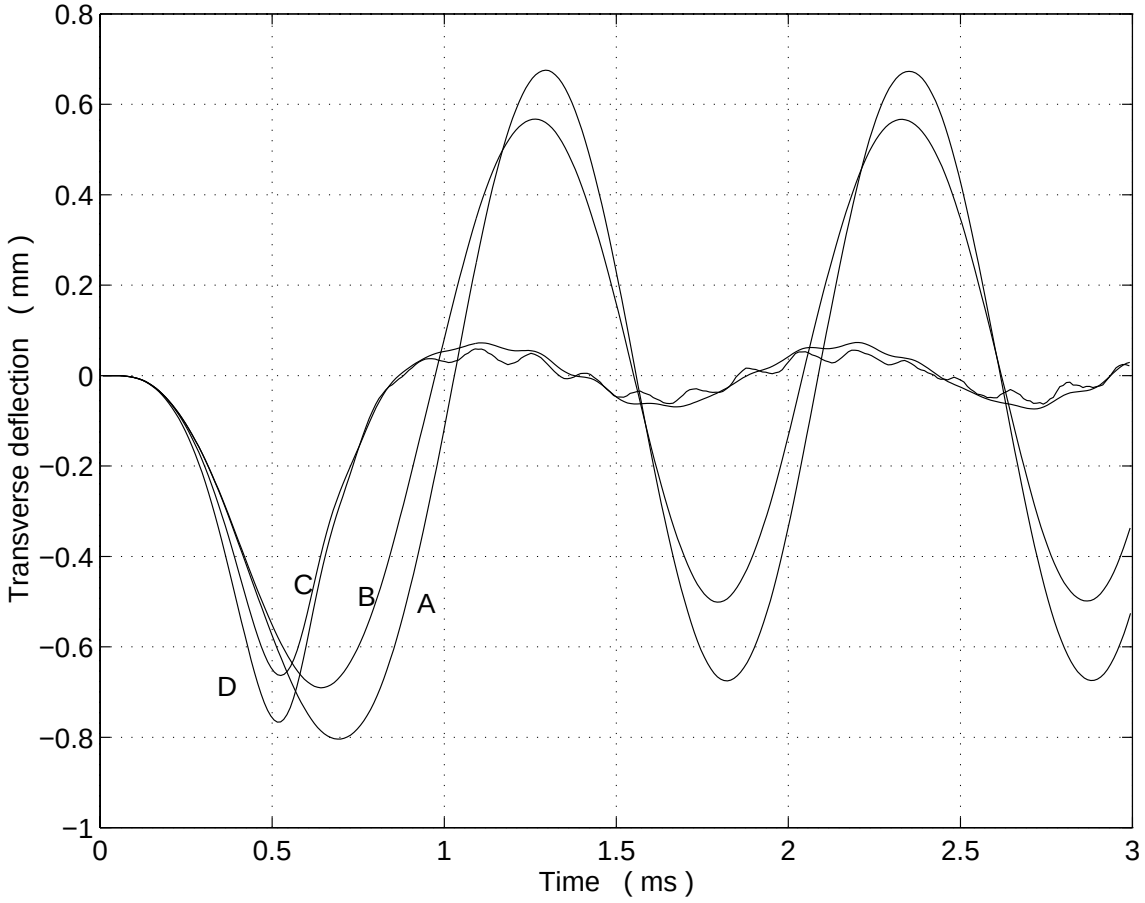

Figure 3.33: Time histories of the transverse displacements of point C when (A) the plate is uncontrolled; (B) sensors/actuators in column I are activated; (C) sensors/actuators in columns I and II are activated; and (D) all sensors/actuators are activated.

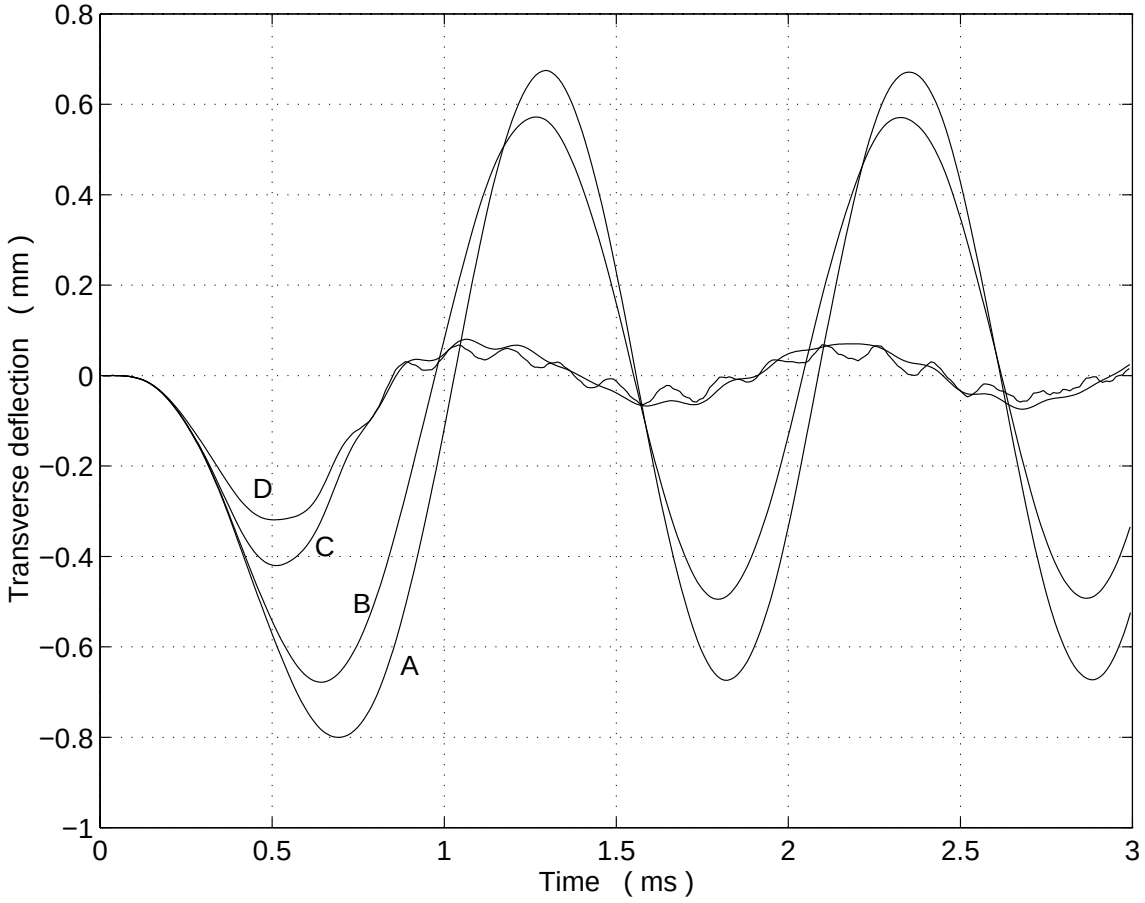

Figure 3.34: Time histories of the transverse displacements of point D when (A) the plate is uncontrolled; (B) sensors/actuators in column I are activated; (C) sensors/actuators in columns I and II are activated; and (D) all sensors/actuators are activated.

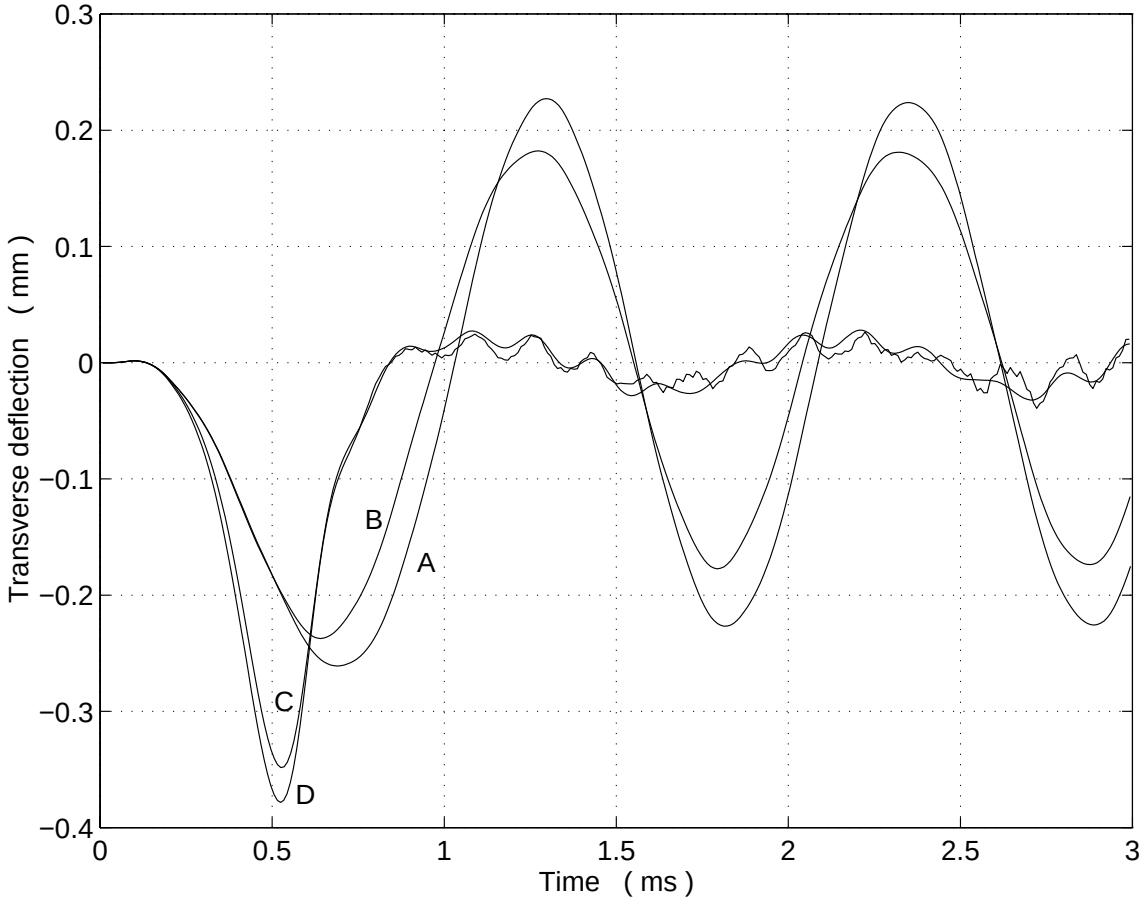

Figure 3.35: Time histories of the transverse displacements of point E when (A) the plate is uncontrolled; (B) sensors/actuators in column I are activated; (C) sensors/actuators in columns I and II are activated; and (D) all sensors/actuators are activated.

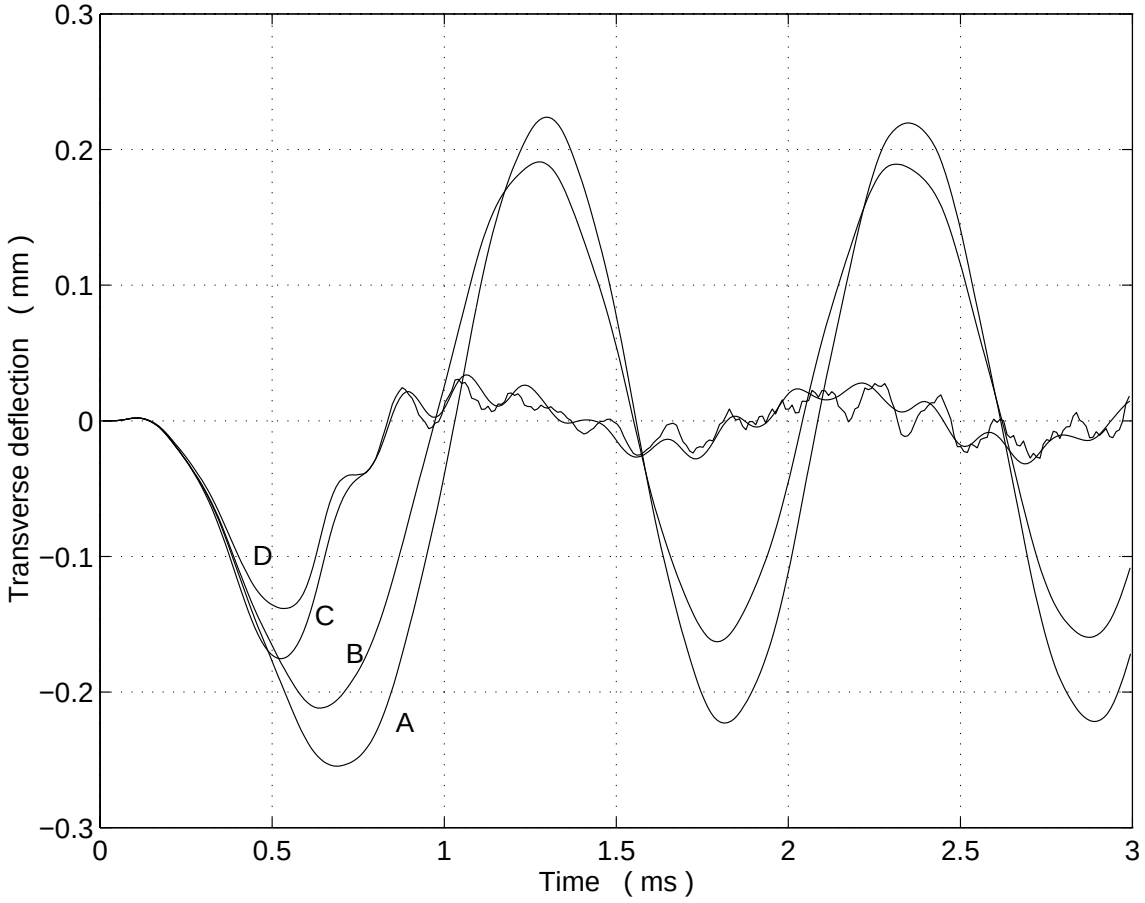

Figure 3.36: Time histories of the transverse displacements of point F when (A) the plate is uncontrolled; (B) sensors/actuators in column I are activated; (C) sensors/actuators in columns I and II are activated; and (D) all sensors/actuators are activated.

Chapter 4

Summary

Dynamic response of linear and nonlinear laminated composite structures with PZT lamina has been studied using three dimensional linear and nonlinear theory of elasticity.

An analytical solution for steady state vibrations of a simply supported rectangular linear elastic laminated plate with piezoelectric actuator and sensor layers either embedded in it or bonded to its surfaces has been found using the method of Fourier series. The piezoelectric actuator and sensor layers are modeled as thin films and are perfectly affixed to the adjoining lamina. Numerical results for thin and thick plates are presented. For a $40cm \times 30cm \times 2mm$ Graphite/Epoxy one-ply plate, the difference in the first six natural frequencies computed by the classical laminated plate theory and the 3-D elasticity theory is less than 2%, which suggests that our technique to use 3-D elasticity theory to compute natural frequencies of the plate is correct. When two $0.1mm$ thick PZT-G1195 films are attached to the top and bottom surfaces of the plate, the maximum difference between the first six natural frequencies for the plate without PZT layers and the plate with PZT layers is 64%. For a $42.4cm \times 30cm$ plate made of 10 layers of Graphite/Epoxy laminates each $0.4mm$ thick arranged symmetrically as 0/90/0/90..., with a PZT-G1195 actuator $0.02mm$ thick embedded between the second and the third substrate layers from the bottom of the plate and a PZT sensor also $0.02mm$ thick embedded between the second and the third substrate layers from the top of the plate, the maximum difference between the first five natural frequencies computed from the thin plate theory with no PZT layers and the present analysis employing the three dimensional elasticity theory and considering the inertia and rigidity of the PZT layers is 3%. Thus for a thin plate with very thin piezoelectric films embedded in it, both theories give nearly identical values of the natural frequencies, and thin PZT films do not affect noticeably the dynamic response of the structure. However, when the thickness of the PZT layers approaches the thickness of the lamina, the maximum difference between first five natural frequencies of the plate as computed by the 3-dimensional linear elasticity theory with and without PZT layers is 15%. The numerical results for a thick plate are also presented. The configuration

of the thick plate is similar to the ten-ply thin laminated plate mentioned above except that the thickness of both laminates and PZT layers is 10 times larger. The maximum difference between the first six natural frequencies of the plate computed by the classical plate theory and the present 3-D elasticity theory is about 44%. The distributions of shear stresses on the interface between the actuator and the adjoining lamina and on the interface between the sensor layer and the adjoining lamina are found to be very high at the edges of the actuator patch, which indicates the possibility of delamination there. However, the delamination will first occur at an interface between the actuator and the lamina rather than between the sensor and the lamina. The distribution of the sensor voltage is found to be similar to that of the out-of-plane displacement of the plate. For the thin and the thick plates, the in-plane displacements vary nearly linearly with the distance from the midplane but the out-of-plane displacement varies parabolically.

The above analytical solution is then applied to study the shape control of a linear elastic laminated plate. Assuming that a composite plate is vibrating freely at a frequency close to one of its natural frequencies, we find the optimum location and size of the actuator patch on which a minimum voltage is applied to suppress the motion of the plate. In this study, the actuator patch is modeled by applying voltage only on a portion of the actuator layer which fully covers the surface of the plate. This is justified for thin actuator patches because the mass and rigidity of the piezoelectric layers do not affect significantly the dynamic response of the plate. It is found that the optimum location(s) of the centriod of the actuator patch coincides with the points where the out-of-plane plate displacement for the corresponding mode is maximum. Keeping the location and the shape of the actuator fixed, we ascertain the voltage required as a function of the length of its diagonal to nullify the vibrations of the plate.

A finite element (FE) program has been developed and validated to analyze three dimensional transient deformations of a neo-Hookean body with both geometrically and materially nonlinear piezoelectric sensors and actuators either affixed to its bounding surface or embedded in it. The constitutive relation for the piezoelectric material is taken to be linear in the Green-Lagrange finite strain tensor but quadratic in the electric field vector. The FE code has been used to successfully simulate Crawley and Anderson's experiment on ascertaining the response of an unconstrained PZT-G1195 plate to large driving voltages, and Moetakef et al.'s experiment on the propagation of flexural waves in an aluminum cantilever beam generated by a pair of PZT-850 actuators attached symmetrically to its free end. In each case the computed and observed results are found to agree with each other within acceptable limits. The program is then used to simulate the propagation of flexural waves generated by nonlinear actuators. Since the necessary nonlinear material constants for PZT-850 are not available, we conduct parametric studies of the material by choosing different nonlinear material constants in the same range as those for the PZT-G1195. It is found that the variation of nonlinear constants of the actuator does not affect much the transverse displacement and velocity of the monitored points located in the aluminum beam. However, the nonlin-

ear constants affect noticeably the transverse displacement and velocity of the monitored points located on the actuator. The overall agreement between the computed and observed transverse velocity of the monitored points is not significantly improved by considering the nonlinear effects of the actuators. The strain and stress fields in the structure are dramatically affected by the nonlinear actuators. The propagation of flexural waves in a defective neo-Hookean cantilever beam is simulated. We use Moetakef et al's set up mentioned above but introduce a $9.525mm \times 1.5875mm \times 1.5875mm$ weak region located symmetrically about the midplane at $184.15mm$ from the free edge. The elastic constants for the material in the weak region equalled 10^{-5} of those in the remainder of the beam. The sensor output is found to be insensitive to the defect considered. The FE code is also used to simulate the active control of a nonlinear cantilever composite plate subjected to an impulse load at its free edge. A simple constant-gain position feedback algorithm is shown to suppress the vibrations of the plate.

Although the research on piezoelectric materials and smart structures has been conducted intensively in recent years, we found that more research still needs to be done. As demonstrated by Crawley and Anderson's experiment, although the second order piezoelastic theory gives results much closer to the test values than those obtained with the linear piezoelastic theory, the agreement between the two is not that good for large values of the electric field. Therefore, some higher order piezoelastic theories need to be developed. At the same time, we found that the values of nonlinear material constants are very hard to find for the commercially used piezoelectric materials such as the PZT and the PVDF. In recent years, hysteresis effects in piezoelectric materials have been observed experimentally, which suggest that the piezoelastic theories should be improved. Another important topic in smart structures is the design of the appropriate feed-back control algorithms. For linear system, the control theories have been reported intensively. For systems including nonlinear piezoelectric elements, however, more research needs to be done.

Appendix A

Changes in Frequencies of a Graphite/Epoxy Laminated Plate Caused by Embedded PZT Layers

We use the three-dimensional linear theory of elasticity to delineate the effect of the thickness, stiffness and mass density of piezoelectric (PZT) layers on the first five natural frequencies of a simply supported graphite/epoxy laminated plate with PZT layers embedded in it.

Plate-like smart structures are usually made of PZT patches either embedded in or bonded to the bounding surfaces of a plate. Here we attempt to ascertain changes in the natural frequencies of the underlying plate due to the PZT patches. We consider a simply supported graphite/epoxy laminated plate with PZT layers embedded in it. The plate is assumed to be made of a homogeneous, orthotropic, linear elastic material and the PZT of a homogeneous, transversely isotropic, linear piezoelectric material poled in the thickness direction. Their constitutive relations are

$$\boldsymbol{\tau} = \mathbf{C}\mathbf{s} - \mathbf{e}^T\mathbf{E}, \tag{A.1}$$

$$\mathbf{D} = \mathbf{e}\mathbf{s} + \boldsymbol{\epsilon}\mathbf{E}, \tag{A.2}$$

where $\boldsymbol{\tau}$ is the stress tensor, $\mathbf{s}$ the infinitesimal strain tensor, $\mathbf{E}$ the electric field vector, $\mathbf{D}$ the electric displacement vector, $\mathbf{C} = \mathbf{C}^T$ the material elasticity tensor, $\mathbf{e}$ the piezoelectric constants, and $\boldsymbol{\epsilon}$ the dielectric permittivity. Equation (A.1) with $\mathbf{e} = \mathbf{0}$ gives the stress-strain relation for each graphite/epoxy lamina.

Batra et al.[1-3] have used the three-dimensional linear elasticity theory to study vibrations of a rectangular, simply supported composite plate with PZT layers either embedded in

[0]This note is intended for publication in the *AIAA J.*.

it or bonded to its upper and/or lower surfaces. We follow the same approach and refer the reader to these references for details. We note that the PZT layers are assumed to be perfectly bonded to the substrate and are modeled as thin films. The structure is excited by applying a sinusoidal voltage to a PZT actuator.

Results presented herein are for a $30\sqrt{2}\times 30\times 0.404$ cm $T300/976$ graphite/epoxy laminated plate shown in Fig. A.1. The material properties of the graphite/epoxy layer with coordinate axes coincident with the principal axes of the lamina are

$$\begin{aligned} &C_{11}=152.35 \text{ GPa},\ C_{12}=C_{13}=391.8 \text{ MPa},\ C_{22}=C_{33}=10 \text{ GPa},\\ &C_{23}=306.75 \text{ MPa},\ C_{44}=250.05 \text{ MPa},\ C_{55}=C_{66}=709.95 \text{ MPa},\\ &\rho=1,600 \text{ kg/m}^3. \end{aligned} \tag{A.3}$$

Values assigned to the PZT material parameters (poled in the 3-direction) are

$$\begin{aligned} &e_{31}=e_{32}=-2.1 \text{ C/m}^2,\ e_{33}=9.5 \text{ C/m}^2,\ e_{24}=e_{15}=9.2 \text{ C/m}^2,\\ &C_{11}=148 \text{ GPa},\ C_{12}=76.2 \text{ GPa},\ C_{13}=74.2 \text{ GPa},\ C_{33}=131 \text{ GPa},\\ &C_{66}=35.9 \text{ GPa};\ \rho=7,500 \text{ kg/m}^3. \end{aligned} \tag{A.4}$$

Only non-zero components of $\mathbf{C}$ and $\mathbf{e}$ are listed above. Also $\boldsymbol{\tau}$ and $\mathbf{s}$ in eqns. (A.1) and (A.2) have been regarded as six-dimensional vectors so that $\mathbf{C}$ is a 6×6 symmetric matrix. The plate is made of ten 0.4 mm thick graphite/epoxy lamina with fiber orientations $[0°/90°/0°/90°/0°]_s$ and two PZT layers, each 0.02 mm thick, embedded in it. The PZT layer located between the second and the third substrate from the bottom acts as an actuator, and that between the second and the third substrate layer from the top as a sensor.

The nondimensional natural frequencies, Ω_{mn}, of the plate are related to its dimensional natural frequencies, ω_{mn}, by

$$\Omega_{mn}=\frac{\omega_{mn}}{\dfrac{\pi^2}{\ell^2}\left(\dfrac{D_{11}}{2\rho h}\right)^{1/2}}, \tag{A.5}$$

where $2h$ is the thickness of the plate, ℓ its length, and D_{11} the flexural rigidity. For the graphite epoxy plate, the five lowest nondimensional natural frequenices Ω_{11}, Ω_{21}, Ω_{12}, Ω_{22} and Ω_{31} according to the thin plate theory[4] equal, respectively, 2.002, 4.585, 6.408, 8.007 and 9.454.

Figure A.2 depicts the dependence of the first five nondimensional natural frequencies upon the variation in the thickness of the PZT layers. Each one of the five frequencies decrease monotonically, though not at the same rate, with an increase in the thickness of the PZT layer. The similar result was also observed by Mitchell and Reddy[6] by using a refined hybrid plate theory. In order to magnify the change in the frequencies, we have plotted the

ratio of the natural frequency of the composite plate with the PZT layers divided by the corresponding frequency of the plate only.

Figures A.3 and A.4 depict, respectively, the dependence of the frequency ratio upon the variation in thickness and mass density of the PZT layers. For a given thickness of the PZT layer, the relative change in the fifth lowest frequency is the highest, that in the lowest fourth frequency is between those for the first and third frequencies, and that in the second frequency is between those for the third and fifth lowest frequencies. For results plotted in Fig. A.4, the thickness of the PZT layer was set equal to that of a lamina. We note that in the experimental set-up of Moetakef et al.[5] the thickness of the PZT patch equalled nearly one-half of that of the beam. The relative change in the lowest five frequencies decreases montonically with an increase in the mass density of the PZT layer. The five curves are nearly parallel to each other signifying that the rate of change of frequency with respect to the mass density of the PZT layer is the same for all five frequencies. As for the variation in the thickness of the PZT layer, the curve for the fourth frequency lies between those for the first and the third ones, and that for the third frequency lies between those for the third and fifth ones.

Since we have modeled the substrate layer as orthotropic and the PZT layer as transversely isotropic, it is not clear how to vary the stiffness of the PZT layer relative to that of the graphite/epoxy substrate. In an attempt to decipher the effect of the material stiffness only, we first set the mass density and the thickness of the PZT layer equal to that of the graphite/epoxy lamina, and vary only C_{11} for the PZT layer. We note that the response of the plate with PZT layers is also affected by values of other components of $\mathbf{C}$ for the PZT. As shown in Fig. A.5, all five lowest natural frequencies of the composite structure increase montonically with an increase in the value of C_{11} for the PZT. In the second study of the effect of the PZT stiffness on the natural frequencies of the plate, we set the thickness of the PZT layer equal to one-tenth of the thickness of the substrate which is more likely to occur in a physical situation, mass density of the PZT layer equal to 7500 kg/m^3, $\mathbf{C}^{\rm PZT} = \alpha \mathbf{C}^{\rm substrate}$, and vary α. We realize that it may be difficult to manufacture a PZT with such mechanical properties. Figure A.6 illustrates the effect of such a change in the elastic moduli of the PZT on the five lowest natural frequencies of the plate with embedded PZT layers. A seven fold increase in the stiffness of the PZTs increases the first five natural frequencies by atmost 10%

Acknowledgement: The author is grateful to Professors D. Inman and L. Librescu for suggesting the problem.

References

1. Batra, R. C., Liang, X. Q. and Yang, J. S., "The Vibration of a Simply-Supported Rectangular Elastic Plate due to Piezoelectric Actuators," *Int. J. Solids Struct.*, Vol. 33, 1996, pp. 1597-1618.

2. Batra, R. C., Liang, X. Q., and Yang, J. S., "Shape-Control of Vibrating Simply-Supported Plates", *AIAA J.*, Vol. 34, No. 1, 1996, pp. 116-122.

3. Batra, R. C., and Liang, X. Q., "The Vibration of a Rectangular Laminated Elastic Plate with Embedded Piezoelectric Sensors and Actuators," *Comp. & Struct.*, 1997 (to appear).

4. Jones, R. M., *Mechanics of Composite Materials*, Scripta Book Co., Washington, D.C., 1975.

5. Moetakef, M. A., Joshi, S. P. and Lawrence, K. L., "Elastic Wave Generation by Piezoceramic Patches," *AIAA J.*, Vol. 34, No. 10, 1996, pp. 2110-2117.

6. Mitchell, J. A., Reddy, J. N., "A Refined Hybrid Plate Theory for Composite Laminates with Piezoelectric Laminae", *Int. J. Solids Struct.*, Vol. 32, No. 16, 1995, pp. 2345-2367.

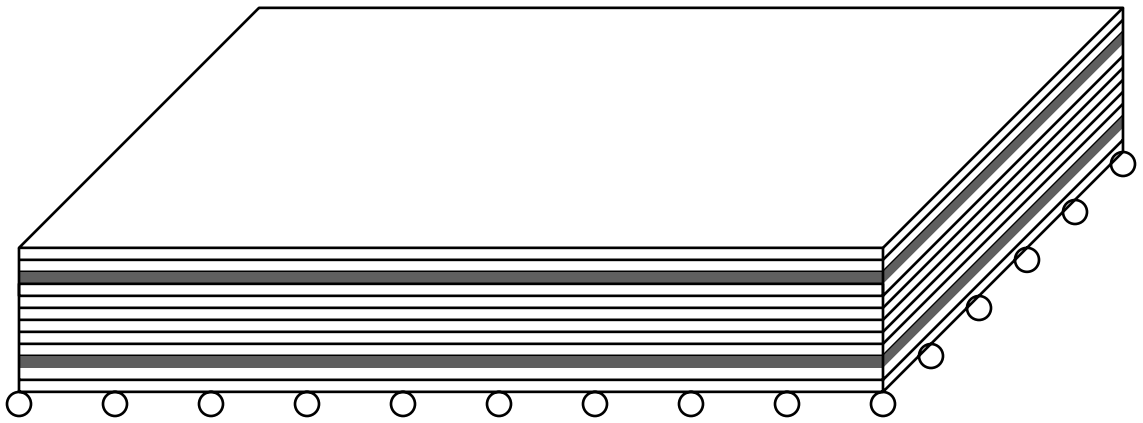

Figure A.1: A sketch of a simply supported composite plate with embedded PZT actuarors and sensors

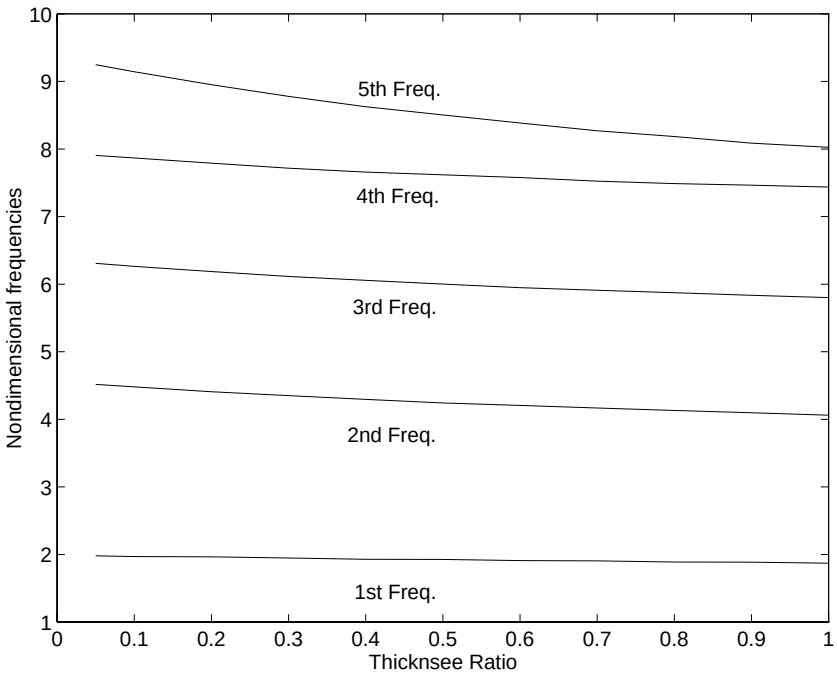

Figure A.2: Nondimensional natural frequencies of the plate with PZT layers vs. thickness of the PZT layer/thickness of the lamina.

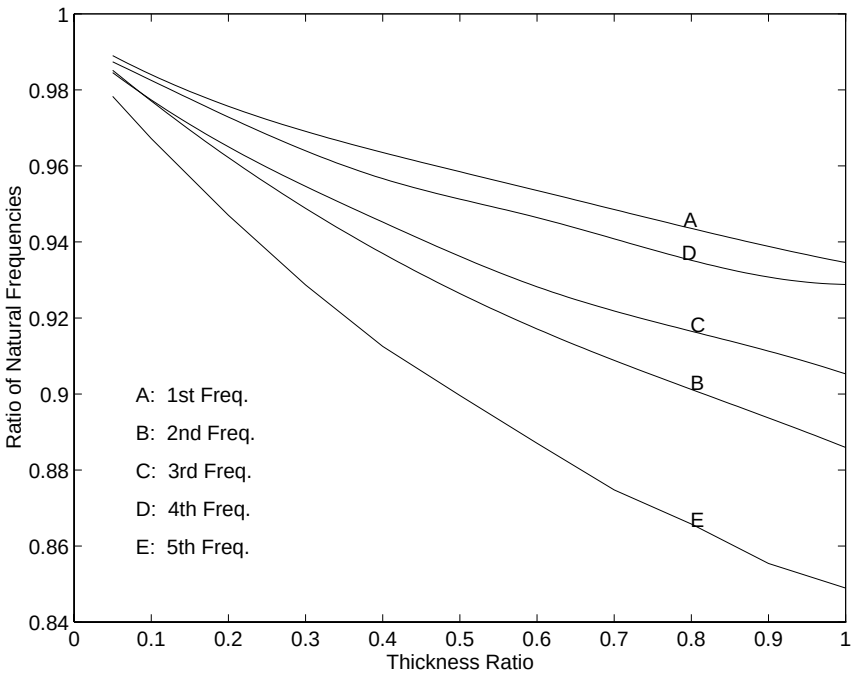

Figure A.3: Frequency of the plate with PZT layers/frequency of the plate without PZT layers vs. thickness of the PZT layer/thickness of the lamina.

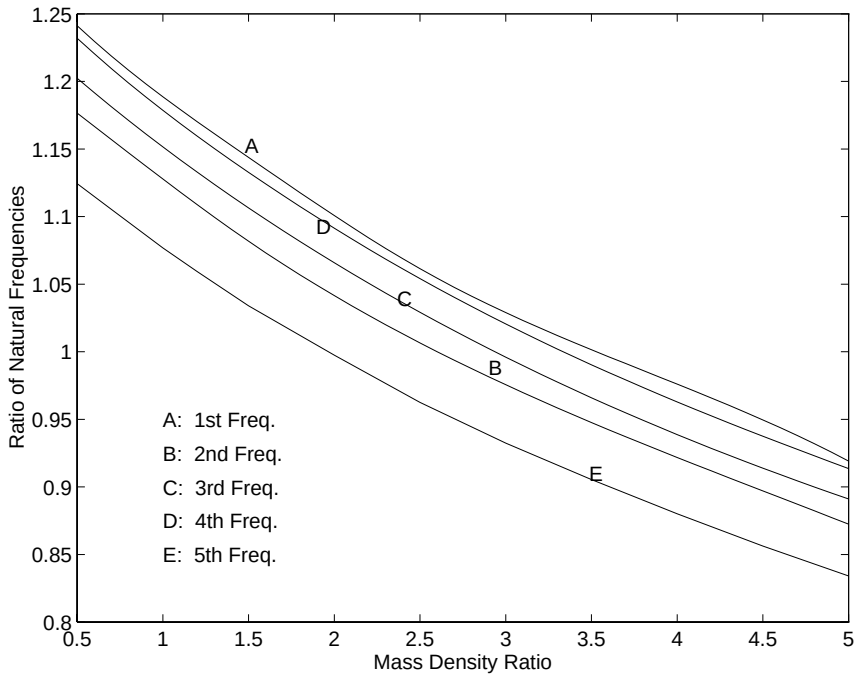

Figure A.4: Frequency of the plate with PZT layers/frequency of the plate without PZT layers vs. mass density of the PZT layer/mass density of the laminate.

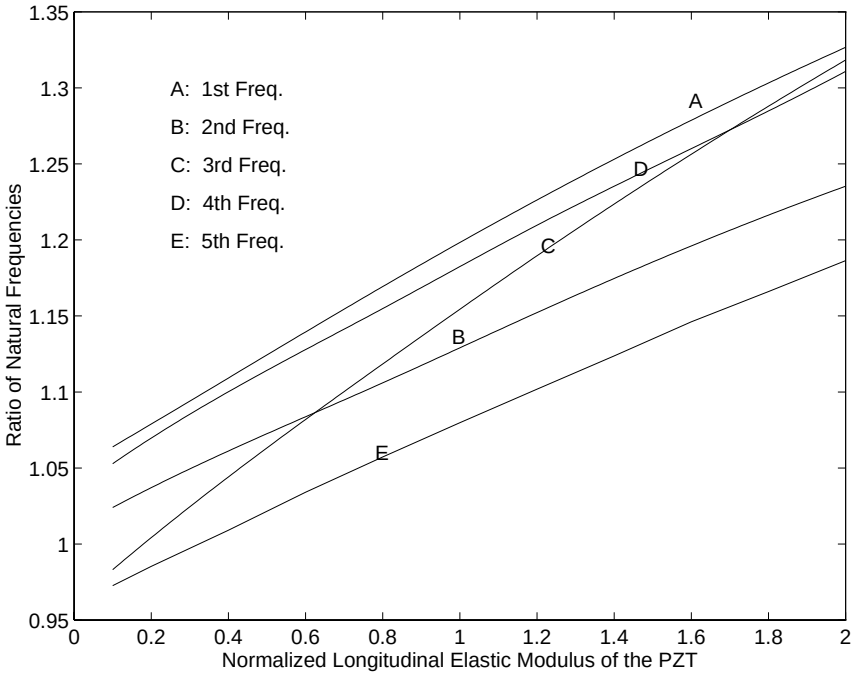

Figure A.5: Frequency of the plate with PZT layers/frequency of the plate without PZT layers vs. C_{11} for the PZT layer/C_{11} for the 0° degree lamina.

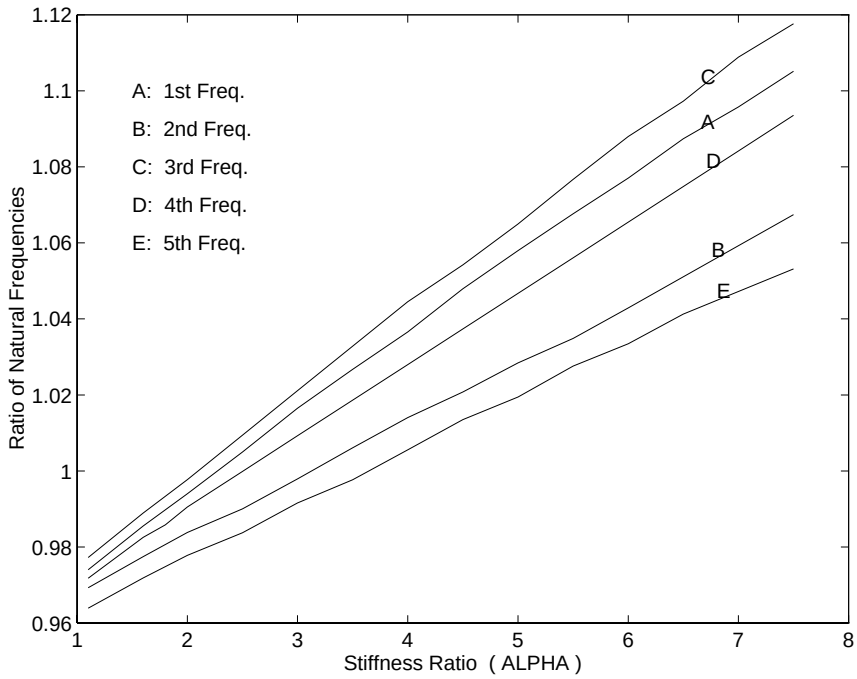

Figure A.6: Frequency of the plate with PZT layers/frequency of the plate without PZT layers vs. α.

Vita

Xiaoqing Liang

The author, Xiaoqing Liang, was born in SaoGuan, P.R. China, on March 15, 1965. He got his Bachelor of Science degree in Engineering Mechanics from the Beijing University, P.R. China, in July of 1987, and his Master of Science in Solid Mechanics from the Institute of Mechanics, Chinese Academy of Sciences, in July of 1990. From July of 1990 to July of 1993, he was employed as a design engineer at the Institute of Mechanics, Chinese Academy of Sciences, and worked in the fields of solid mechanics. In September of 1993, he enrolled in University of Missouri-Rolla to pursue a Doctor of Philosophy degree under the supervision of Professor Romesh C. Batra. He transferred to Virginia Polytechnic Institute and State University in August of 1994 and successfully fulfilled the requirements for a Ph.D. in Engineering Mechanics in February of 1997.